On cosmic censorship for the Einstein-Vlasov system

A numerical study of the spherically symmetric Einstein-Vlasov system for dust-like initial data

Master's thesis in Engineering Mathematics and Computational Science

Edvin Martinson

DEPARTMENT OF MATHEMATICAL SCIENCES
CHALMERS UNIVERSITY OF TECHNOLOGY
Gothenburg, Sweden 2024
www.chalmers.se

Master's thesis 2024

On cosmic censorship for the Einstein-Vlasov system

A numerical study of the spherically symmetric Einstein-Vlasov system for dust-like initial data

Edvin Martinson

CHALMERS
UNIVERSITY OF TECHNOLOGY

Department of Mathematical Sciences
Division of Analysis and Probability Theory
Chalmers University of Technology
Gothenburg, Sweden 2024

On cosmic censorship for the Einstein-Vlasov system
A numerical study of the spherically symmetric Einstein-Vlasov system for dust-like initial data
Edvin Martinson

Supervisor: Håkan Andréasson, Department of Mathematical Sciences
Examiner: Håkan Andréasson, Department of Mathematical Sciences

Master's Thesis 2024
Department of Mathematical Sciences
Division of Analysis and Probability Theory
Chalmers University of Technology
SE-412 96 Gothenburg
Telephone +46 31 772 1000

Cover: Trapped surface in the spherically symmetric Einstein-Vlasov system with inhomogeneous initial data.

Typeset in LaTeX
Gothenburg, Sweden 2024

On cosmic censorship for the Einstein-Vlasov system
A numerical study of the spherically symmetric Einstein-Vlasov system for dust-like initial data
Edvin Martinson
Department of Mathematical Sciences
Chalmers University of Technology

Abstract

Already in the first solution of the Einstein field equations of general relativity, singularities appeared. A great deal of effort has since been put into understanding these objects. If there exist singularities from which matter or light could escape, it would lead to a breakdown of the predictability of the Einstein field equations. The concept of *cosmic censorship*, which asserts that no such singularities exist, is thus fundamental to the theory of general relativity and has been debated in the community ever since it was first conjectured. In this thesis, cosmic censorship is investigated numerically in the spherically symmetric, asymptotically flat Einstein-Vlasov system. The Vlasov matter model is compared to the more primitive *dust* model, which is known to generate *naked singularities* that contradict cosmic censorship. The Einstein-Vlasov system is simulated with a *Particle In Cell* method. The results indicate that initial data that is known to produce naked singularities in dust matter does not give naked singularities in Vlasov matter with large initial velocity dispersion. Moreover, it is shown that the Einstein-Vlasov system can approximate the dust system arbitrarily well up to numerical accuracy. In order to show that cosmic censorship holds even for Vlasov matter that is initially arbitrarily close to dust, better precision in the simulations and a combination of numerical and analytical studies are needed.

Keywords: Einstein-Vlasov, cosmic censorship, naked singularities, Particle In Cell (PIC), general relativity, kinetic theory, black holes.

Acknowledgements

First and foremost, I would like to thank my supervisor Håkan Andréasson for introducing me to this fascinating subject and for his enthusiasm and support during the project. My questions were always answered with great insight and interest, and I have greatly appreciated our discussions on everything from mathematics to skiing. I hope that we can continue this partnership in future work. I would also like to thank Thomas Bäckdahl for efficiently calculating the expression of the Kretschmann scalar, saving me many hours of manual derivations. To my dear friend Ludvig Rodung, I express my gratitude for helping me to understand important concepts of general relativity in the initial stages of the project and for being a sounding board to discuss with. Moreover, I would like to give a special thanks to my friends Isak Wikman, Samuel Winqvist and Pontus Ericstam for valuable feedback on this text. Finally, I am very grateful to my family for always supporting me and encouraging me to ask questions about the world around us.

Edvin Martinson, Gothenburg, June 2024

List of acronyms

Below is the list of acronyms that have been used throughout this thesis listed in alphabetical order:

ADM	Arnowitt–Deser–Misner (mass)
EFE	Einstein Field Equations
ODE	Ordinary Differential Equation
PG	Painlevé-Gullstrand (coordinates)
PIC	Particle In Cell (method)
SCCC	Strong Cosmic Censorship Conjecture
WCCC	Weak Cosmic Censorship Conjecture

Nomenclature

Below is the nomenclature of quantities, indices, parameters, and variables that have been used throughout this thesis.

Tensors & scalars

Abstract index notation and Einstein summation notation is used, see section 2.1.4 and 2.1.3 for details. *Latin* indices $a, b, \ldots$ act as a reminder of the tensor type while *greek* indices $\mu, \nu, \ldots$ are used for tensor elements in a specific basis.

g_{ab} or ds^2	Spacetime metric tensor
T_{ab}	Stress-energy-momentum tensor
R_{ab}	Ricci curvature tensor
R_{abcd}	Riemann curvature tensor
$\Gamma^a{}_{bc}$	Christoffel symbol
K	Kretschmann scalar
R	Scalar curvature

Einstein-Vlasov system

t	Time coordinate
r	Area radius
$\check{r}$	Comoving radius
a	Metric function
β	Metric function
A	Used for notational purpose: $A := \frac{1}{a^2} - \beta^2$
f	Density function
w	Radial momentum
L	Angular momentum
ρ	Energy density
j	Current of particles
p	Radial pressure
p_T	Tangential pressure
M	System mass within radius r
$\mathcal{M}$	ADM mass

t_H	Apparent horizon
r_b	Boundary radius

Initial data parameters and other quantities

ε	Initial velocity dispersion parameter
$\mathring{C} = \frac{\gamma}{3\pi}$	Initial energy density amplitude in homogeneous data
p	Parameter in Eardly-Smarr data (fixed to 3/2 in PG coordinates)
ζ	Parameter in Eardly-Smarr data
ζ_{crit}	Critical value of ζ s.t. $\zeta > \zeta_{\text{crit}}$ gives naked singularities in dust
$\mathring{t}$	Dust singularity time in Eardly-Smarr data
$\mathring{t}_V$	Vlasov singularity time
$\mathring{r}$	Choice of initial radius for calculating null geodesics
$r_{\breve{m}}$	Choice of grid point to represent $\mathring{r}$
K_{limit}	Numerical Kretschmann scalar singularity limit

PIC simulation

Indices

i	Particle index
k	Time step index
m	Spatial element/Grid point index

Parameters

N	Number of particles
N_t	Number of time steps
N_x or N_r	Number of spatial grid elements
N_u	Number of different initial momentum sizes
N_α	Number of different initial momentum angles
r_{min}	Minimum area radius
r_{max}	Maximal area radius
t_{final}	Final time
Δt	Temporal grid size
Δx or Δr	Spatial grid size

Contents

1

Introduction

Ever since Einstein first presented his field equations of general relativity in 1915, people have tried to solve these equations to gain insights about our universe. The *Einstein field equations* (EFE) are

$$R_{ab} - \frac{1}{2} R\, g_{ab} = \frac{8\pi G}{c^4} T_{ab} \ , \tag{1.1}$$

where indices $a, b = 0, 1, 2, 3$ denote the four dimensions of spacetime, R_{ab} is the Ricci curvature tensor, R is the scalar curvature, g_{ab} is the spacetime metric tensor, G is the Newtonian gravitational constant, c the speed of light and T_{ab} is the stress-energy-momentum tensor. In simple terms, (1.1) connects the curvature of spacetime, described by the left hand side, to the matter content in spacetime, described by the right hand side. The unknown is in principle the spacetime metric, g_{ab}, but since this depends on the matter content, the equations need to be solved for the metric and the matter content simultaneously.

The first solution of (1.1) was presented by Schwarzschild, who in 1916 solved the equations for a static, spherically symmetric, vacuum case [1]. Already in this solution, *singularities* appeared. Initially, these singularities were regarded as just a mathematical curiosity of the EFE and something that could never exist in reality. However, in 1939, Oppenheimer and Snyder [2] showed for the first time how matter could collapse to form what is now known as a *black hole*. In their solution, they used a matter model known as *dust* (a pressureless perfect fluid) with homogeneous initial data and could show that a so called *trapped surface* formed around the singularity. Put simply, a trapped surface is a region in spacetime that is so curved, that no particle, or even light, can escape it.

If there exist singularities from which matter or light could escape, it would lead to a breakdown of the predictability of the Einstein field equations. Since the equations "blow up" at singularities, there would be no way of predicting the behaviour of a light ray that escapes from a singularity. Thus, in 1969, Penrose [3] formulated a conjecture known as the *weak cosmic censorship conjecture* (WCCC). It asserts that all physically realistic gravitational collapses are covered by an *event horizon*, and hence can not be observed by a distant observer. The validity of this conjecture has been discussed by researchers ever since.

In 1979, Eardly and Smarr [4] used numerical methods to show that a spherically symmetric dust system forms so called *naked singularities* for a certain set of inhomogeneous initial data. Naked singularities are singularities from which light

can escape to a distant observer, and their existence thus contradict weak cosmic censorship. The results achieved by Eardly and Smarr were shown analytically by Christodolou in 1984 [5]. At first glance, these results appear to disprove the WCCC. However, since they treat a very simplified case, which may not be physically realistic, they are not enough to disprove the conjecture in general. In the framework used by Eardly and Smarr, only one element of T_{ab} is non-trivial in the dust case, which indicates the simplicity of the dust model [6]. Eardly and Smarr themselves write that their results concerning cosmic censorship are likely to change in more advanced matter models [4]. In the last decades, mathematical studies of cosmic censorship have mainly been focused on using more general fluid models or dust cases where the symmetry is perturbed [6].

An alternative phenomenological matter model comes from the Vlasov equation, which originates in kinetic theory, and gives a statistical description of a collection of particles [7]. In kinetic theory, particle systems are described by a density function, $f = f(t, x, p)$, which represents the density of particles for a given time, t; position, x; and momentum, p. Macroscopic properties, like the energy density, are easily obtained by integrating f over momentum space [8]. The time evolution of the system is determined by the relevant force fields which are generated by all the particles collectively. Which force fields are relevant and which type of particle that is described, depends on the field of research. In for example plasma physics, the particles are normally electrons or ions and the dynamics are given by the Maxwell equations. This project is interested in the case of astrophysics, where the particles are stars and the field equations are those of general relativity [7].

Kinetic theory has been studied intensively in other areas of research and is thus relatively well known mathematically. Until the 1990s, it was, however, rarely used as a matter model in mathematical studies of general relatively, despite having some fundamental advantages [8]. In the Einstein-Vlasov system, four components of T_{ab} are non-trivial, which shows that the Vlasov model is more complex than the dust model. Moreover, it is still an open question if naked singularities can form in the Einstein-Vlasov system [6]. This thesis aims to help in answering this question, and more specifically to answer if initial data that results in naked singularities in the spherically symmetric dust case also gives naked singularities in the Vlasov case.

Recent studies by H. Andréasson and G. Rein [9], suggests that the Vlasov system can approximate the dust system arbitrarily well. It is therefore natural to ask what happens in regards to cosmic censorship for a Vlasov system that is initially arbitrarily close to dust. Earlier this year, C. Kehle and R. Unger [10] published a related study, in which they consider *critical collapse* in the Einstein-Maxwell-Vlasov system. They show that, depending on the initial mass of the system, the Vlasov matter either disperses or collapses to a black hole and that no naked singularities are formed as the critical parameter value is crossed. The result is obtained by considering a certain dust solution, which is "desingularised" by Vlasov matter in a similar fashion as done in this work.

1.1 Purpose

The overall purpose of this project is to analyse the Einstein-Vlasov system numerically to see if naked singularities are formed with this matter model. As described above, this is still an open question and the hope is that the results will help in future analytical investigations planned by H. Andréasson et.al. Specifically, there are two main questions that are to be investigated. Namely, if the Vlasov model can approximate dust arbitrarily well and if instances where dust is known to give naked singularities also give naked singularities with the Vlasov matter model.

1.2 Goals

As indicated by the purpose, there are two main questions to be answered and the work is thus divided into two parts. The first part considers homogeneous initial data as in the Oppenheimer-Snyder solution. Here, the numerical results can be directly compared with the analytical results in [2]. The goal is to show that the dust model can be estimated arbitrarily well by the Vlasov model.

In the second part, inhomogeneous initial data in the form proposed by Eardly and Smarr is studied. The first step is to replicate the work with dust matter done in [4] and to translate this into the framework of this thesis. This is done to gain a deeper understanding of the results presented by Eardly and Smarr and to find the specific instances of initial data that give naked singularities with dust in our framework. Once the form of the initial data is known, it needs to be shown that the numerical method is numerically sound with this initial data. The final goal is to analyse the Einstein-Vlasov system with initial data that gives naked singularities for dust.

1.3 Limitations

In this project, only the case of spherical symmetry in an asymptotically flat spacetime is considered. This work is focused on the effect of the matter model, with respect to cosmic censorship. It is therefore of interest to see what happens in cases where naked singularities are known to appear with a dust model, i.e. in the spherically symmetric case. Furthermore, the system of interest is a group of stars that collapse to a black hole. Whatever is far away from this system, like the global shape of the universe, is not of interest. This motivates the asymptotical flatness, which in physical terms means that there are no gravitational effects far away from the system.

The Vlasov model is not compared to any other phenomenological matter model than the dust model. Dust is one of the most popular matter models used by mathematical physicists, but there are also others such as perfect fluid models and scalar fields. More specifically, the comparison is focused around the well known works by Oppenheimer-Snyder [2] and Eardly-Smarr [4], since these are typical examples.

To show that the Vlasov model can approximate dust arbitrarily well, only one error measurement, based on the theoretical trapped surface and boundary radius is used. The error is measured only in the first (in time) point where a trapped surface appears. There are a number of more sophisticated error measures that could be used, e.g. an L^2 error measure of the entire apparent horizon or an L^2 error measure of the metric functions over the entire domain. In regards to cosmic censorship, the crucial point is, however, where the trapped surface crosses the boundary radius. Moreover, H. Andréasson and G. Rein [9] have during the course of this work shown analytically that Vlasov matter can approximate dust arbitrarily well. The numerical studies here are thus of less interest and only constitute a small part of the project. Hence, we suffice with the chosen error measure.

Following [9], we use *Painlevé-Gullstrand* (PG) coordinates. Previous analysis by H. Andreasson and G. Rein has shown that this is preferable over using *comoving* coordinates, which are used in the original paper by Eardly-Smarr, due to problems with local existence in the Vlasov system. It is, however, not possible to in general translate the initial data prescribed in [4] to our framework in PG coordinates. An overview of the system considered in [4] is presented in Appendix C and the initial data depends on two parameters $p > 0$ and $\zeta \geq 0$. Specifically, the translation is not possible for general p. As shown in [9], the expressions become particularly manageable for $p = \frac{3}{2}$ and we thus restrict our analysis to this case. This is in principle not a restriction, since the exact parameter values are not important as long as it can be shown that naked singularities in the dust case disappear with Vlasov matter for the same parameters.

Furthermore, there is an infinite set of parameters that give naked singularities with dust. Namely, naked singularities occur for all $\zeta > \zeta_{\text{crit}}$. We restrict our investigation of cosmic censorship in Vlasov matter to two different zeta values and merely discuss how further investigations could be conducted for a more general result.

Finally, we limit the investigation to Vlasov matter that is relatively far from dust. The effect of using Vlasov matter instead of dust does not come into effect until very close to the singularity. To see this effect numerically, higher precision would be needed, which would require more computer power or simulation time. In section 7.1, we discuss how to show that cosmic censorship holds even for Vlasov matter that is arbitrarily close to dust by a combination of analytical and numerical studies.

1.4 Outline

In the following chapter, the mathematical structure of general relativity and important concepts in astrophysics are introduced. A brief overview of the EFE and kinetic theory is given to present the Einstein-Vlasov system. In chapter 3, a general description of the PIC scheme is outlined before this is specified in the context of this thesis in chapter 5. The main system of this thesis is presented in chapter 4 and the numerical methods used to simulate it are specified in chapter 5. The main results are presented and discussed in chapter 6, and the implications of them are summarised in chapter 7 together with an outlook on further analysis required.

2

Theoretical background

In this chapter, the theoretical framework of the project is presented. First, a background of important mathematical concepts in general relativity, such as tensor calculus, metrics and manifolds, is given. These mathematical concepts are then concretely connected to the structure of spacetime, where general relativity is briefly compared to the picture in pre-relativistic physics and special relativity. For context, some relevant terminology used within the field of astrophysics is then presented. A brief overview of the Einstein field equations and kinetic theory is given before they are put together to form the Einstein-Vlasov system. Note that, unless otherwise stated, *geometrised units* are used in all the physical formulas in this chapter. Specifically, we set Newtons gravitational constant $G = 1$ and the speed of light $c = 1$.

2.1 Tensor calculus and manifolds

The theory of general relativity frequently uses tensors to describe the equations. Here, some of the key concepts of tensor calculus are presented. Moreover, a brief introduction to manifolds and the metric tensor is given. The formalism follows that presented by Wald in [1].

2.1.1 Tensors

Tensors can be seen as a generalisation of vectors and matrices. To precisely describe them, some formalism is needed. Let V be a finite dimensional real vector space. The *dual space*, V^*, can then be defined as the space of all linear maps $f : V \to \mathbb{R}$. In other words, $V^* := \{f \,|\, f : V \to \mathbb{R}, f \text{ linear}\}$. An element $v^* \in V^*$ is called a *dual vector*. Furthermore, if $\{v_1, \ldots, v_n\}$ is a basis of V, then $\{v^{1^*}, \ldots, v^{n^*}\}$ is a basis of V^*, where $v^{i^*} v_j = \delta^i_j$. Here, δ^i_j is the Kronecker delta. This implies that $\dim(V) = \dim(V^*) = n$, and since the basis elements are directly correspondent, there is an isomorphism between V and V^*. However, this isomorphism depends on the basis, so more structure is needed to define it. To add this structure, a metric is introduced, which is described in section 2.1.8. Note that the dual of the dual vector space, $(V^*)^*$, is naturally isomorphic to the original vector space V. Thus, $(V^*)^*$ can be directly identified with V.

With this formalism, we can define the notion of a tensor. A tensor, T, of type (k, l) is a multilinear map

$$T : \underbrace{V^* \times \cdots \times V^*}_{k \text{ times}} \times \underbrace{V \times \cdots \times V}_{l \text{ times}} \to \mathbb{R} \,. \tag{2.1}$$

A dual vector is thus a $(0, 1)$-tensor. If we define vectors as column vectors in some basis, we see that dual vectors can be viewed as a row vectors. Moreover, the linear map defined by them is the scalar product. To illustrate, let $x \in V$ and $y \in V^*$. Then, $y : V \to \mathbb{R}$, and

$$yx = \begin{bmatrix} y_1, \ldots, y_n \end{bmatrix} \begin{bmatrix} x^1 \\ \vdots \\ x^n \end{bmatrix} = y_1 x^1 + \cdots + y_n x^n \in \mathbb{R} \,, \tag{2.2}$$

where, by convention, subscripts denote the components of dual vectors and superscripts components of vectors. Also note that a $(1, 0)$-tensor would be an element of $(V^*)^*$, but since $(V^*)^*$ is identified with V, a $(1, 0)$-tensor is just an ordinary vector.

Due to this identification, tensors of higher type can be thought of in several equivalent ways. By fixing an element $v \in V$ in the $(1, 1)$-tensor T, we get $T(\cdot\,, v) : V^* \to \mathbb{R}$. Thus, $T(\cdot\,, v) \in (V^*)^*$, which, by the identification, implies $T(\cdot\,, v) \in V$. T is thus a linear map from V to V, i.e. $T : V \to V$. To illustrate this, T can be thought of as an $n \times n$ matrix in a given basis. With x and y as above, T can be described either as in (2.1),

$$T(y, x) = yTx = \begin{bmatrix} y_1, \ldots, y_n \end{bmatrix} \begin{bmatrix} T^1{}_1 & \ldots & T^1{}_n \\ \vdots & \ddots & \vdots \\ T^n{}_1 & \ldots & T^n{}_n \end{bmatrix} \begin{bmatrix} x^1 \\ \vdots \\ x^n \end{bmatrix} \in \mathbb{R} \,, \tag{2.3}$$

or as a linear map $T : V \to V$,

$$T(\cdot, x) = Tx = \begin{bmatrix} T^1{}_1 & \ldots & T^1{}_n \\ \vdots & \ddots & \vdots \\ T^n{}_1 & \ldots & T^n{}_n \end{bmatrix} \begin{bmatrix} x^1 \\ \vdots \\ x^n \end{bmatrix} = \begin{bmatrix} T^1{}_1 x^1 + \cdots + T^1{}_n x^n \\ \vdots \\ T^n{}_1 x^1 + \cdots + T^n{}_n x^n \end{bmatrix} \in V \,. \tag{2.4}$$

Vectors and matrices are thus low-level tensors, which can be formalised by the following. Given a basis $\{v_1, \ldots, v_n\}$ of V and a basis $\{v^{1^*}, \ldots, v^{1^*}\}$ of V^*, a (k, l)-tensor can be expressed as an object with n^{k+l} elements.

2.1.2 Tensor transformation law

Naturally, the tensor elements depend on the coordinate system used. If the coordinate system is changed, the tensor elements are changed accordingly, which is described by the *tensor transformation law*. Let $\{x_0, \ldots, x_n\}$ be the initial coordinate system and let $\{\tilde{x}_0, \ldots, \tilde{x}_n\}$ be another coordinate system related to $\{x_0, \ldots, x_n\}$ by some map. If T is a (k, l)-tensor with tensor elements $T^{\mu_1, \ldots, \mu_k}{}_{\nu_1, \ldots, \nu_l}$ in the initial coordinate system, the tensor elements in the new coordinate system can be calculated as

$$\tilde{T}^{\alpha_1, \ldots, \alpha_k}{}_{\beta_1, \ldots, \beta_l} = \sum_{\mu_1, \ldots, \nu_l = 1}^{n} T^{\mu_1, \ldots, \mu_k}{}_{\nu_1, \ldots, \nu_l} \frac{\partial \tilde{x}^{\alpha_1}}{\partial x^{\mu_1}} \cdots \frac{\partial \tilde{x}^{\alpha_k}}{\partial x^{\mu_k}} \frac{\partial x^{\nu_1}}{\partial \tilde{x}^{\beta_1}} \cdots \frac{\partial x^{\nu_l}}{\partial \tilde{x}^{\beta_l}} \,. \tag{2.5}$$

2.1.3 Einstein summation notation

To handle tensor operations more easily, Einstein introduced an index notation in which summation over repeated indices is implied. As an example, consider the summation in (2.2). The sum would in normal matrix notation be written as

$$yx = \sum_{i=1}^{n} y_i x_i \ . \tag{2.6}$$

In Einstein notation, however, the sum over repeated indices is implied and the above is written as

$$yx = y_i x^i \ , \tag{2.7}$$

where the sum is understood to run over $i = 1, \ldots, n$. In this simple example, not much is gained from the simplified notation. Consider now the matrix multiplication in (2.4). Let $b = Tx$, then the elements of b in normal matrix notation would be written as

$$b_i = \sum_{j=1}^{n} T_{ij} x_j \ , \quad i = 1, \ldots, n \ . \tag{2.8}$$

In Einstein notation, this is written as

$$b^i = T^i_{\ j} \, x^j \ , \tag{2.9}$$

where it is understood that the sum runs over the repeated index $j = 1, \ldots, n$ and that it is true for all $i = 1, \ldots, n$.

As the level of the tensor increases, the implied summation notation becomes more and more useful. This notation is used throughout this report, unless otherwise stated.

2.1.4 Abstract index notation

When doing operations on tensors, it can quickly become difficult to keep track of which indices are involved in a specific operation. Furthermore, as described in section 2.1.1, a high level tensor can be viewed in different ways. One way of simplifying the notation is by introducing a basis $\{v_1, \ldots, v_n\}$ of V and $\{v^{1^*}, \ldots, v^{n^*}\}$ of V^*. Then each (k, l)-tensor can be expressed by its basis components $T^{\mu_1,\ldots,\mu_k}{}_{\nu_1,\ldots,\nu_l}$. However, an equation that is true for the tensor elements in a specific basis, may not be true as a general tensor equation. Note that the reverse is always true.

To distinguish between pure tensor operations and operations on tensor elements in a specific basis, the *abstract index notation* presented in [1] is used. A (k, l)-tensor, T, is denoted by $T^{a_1,\ldots,a_k}{}_{b_1,\ldots,b_l}$. The *latin* indices do not denote the elements in a specific basis, but rather act as a reminder of which type of tensor T is. *Greek* indices are instead used to denote the tensor elements in a specific basis. For example $T^{\mu}{}_{\nu}$ denotes the (μ, ν)-th basis component of the tensor $T^a{}_b$.

This notation can be seen as a convenient mixture between the purely mathematical notation, writing tensors as letters without information of the type, and the element-wise notation, which potentially loses information by only considering the tensor elements in a specific basis.

With this notation, we again consider equation (2.2). The left hand side would now change from the purely mathematical notation yx to $y_a x^a$. With Einstein notation, this would imply summation over a. It could thus directly be seen that this is a scalar, even if the basis is not known. The notation $y_\mu x^\mu$ would also be a scalar, although, it would be the summation over the tensor elements in a specific basis. In the same way, the left hand sides of equation (2.3) and (2.4), would be written as $y_a T^a{}_b\, x^b$ and $T^a{}_b\, x^b$ respectively. Note here that in the second expression the index b will be summed over, leaving a super-scripted a, which then directly indicates that the object is a $(1,0)$-tensor (i.e. a vector).

The abstract index notation is, as the Einstein summation notation, used for the remainder of this report, unless otherwise stated.

2.1.5 Tensor operations

Here, some of the most important tensor operations are presented. The *contraction* operation reduces the dimension of the tensor, by summing over a vector index, i, and a dual vector index, j. For a (k,l)-tensor, $T^{a_1,\ldots,a_k}{}_{b_1,\ldots,b_l}$, the contraction operator C with respect to the i-th and j-th indices gives

$$\begin{aligned} C(T^{a_1,\ldots,a_k}{}_{b_1,\ldots,b_l}; i, j) &= T^{a_1,\ldots,a_{i-1},c,\,a_{i+1},\ldots,a_k}{}_{b_1,\ldots,b_{j-1},c,\,b_{j+1},\ldots,b_l} \\ &= U^{a_1,\ldots,a_{i-1},\,a_{i+1},\ldots,a_k}{}_{b_1,\ldots,b_{j-1},\,b_{j+1},\ldots,b_l} \ , \end{aligned} \tag{2.10}$$

where U is a $(k-1,l-1)$-tensor. Note that summation over c is implied. For a $(1,1)$-tensor, which we associate with a $n \times n$ matrix, the contraction $T^a{}_a$ is just the *trace* of the matrix.

Another important tensor operation is the *outer product*. The outer product operator takes a (k,l)-tensor, $T^{a_1,\ldots,a_k}{}_{b_1,\ldots,b_l}$, and a (m,n)-tensor, $U^{c_1,\ldots,c_m}{}_{d_1,\ldots,d_n}$, and constructs a $(k+m, l+n)$-tensor,

$$S^{a_1,\ldots,a_k,c_1,\ldots,c_m}{}_{b_1,\ldots,b_l,d_1,\ldots,d_n} = T^{a_1,\ldots,a_k}{}_{b_1,\ldots,b_l} \otimes U^{c_1,\ldots,c_m}{}_{d_1,\ldots,d_n} \ . \tag{2.11}$$

In a given basis of V and V^*, the elements of $S^{a_1,\ldots,a_k,c_1,\ldots,c_m}{}_{b_1,\ldots,b_k,d_1,\ldots,d_n}$ are given by the product of the elements of $T^{a_1,\ldots,a_k}{}_{b_1,\ldots,b_l}$ and $U^{c_1,\ldots,c_m}{}_{d_1,\ldots,d_n}$. In other words,

$$S^{\alpha_1,\ldots,\alpha_k,\mu_1,\ldots,\mu_m}{}_{\beta_1,\ldots,\beta_l,\nu_1,\ldots,\nu_n} = T^{\alpha_1,\ldots,\alpha_k}{}_{\beta_1,\ldots,\beta_l}\, U^{\mu_1,\ldots,\mu_m}{}_{\nu_1,\ldots,\nu_n} \ . \tag{2.12}$$

Using abstract index notation, the "$\otimes$" in (2.11) can thus be omitted.

To illustrate the outer product, let $\{v_1, v_2\}$ be a basis of V and $\{v^{1^*}, v^{2^*}\}$ a basis of V^*. A (0,1)-tensor, T_a, and a (1,0)-tensor, U^b, can then be represented by their basis components as

$$T_a = \begin{bmatrix} T_1 & T_2 \end{bmatrix} \ , \ U^b = \begin{bmatrix} U^1 \\ U^2 \end{bmatrix} \ , \tag{2.13}$$

and the outer product, $S^a{}_b$, is given by

$$S^a{}_b = T_b\, U^a = \begin{bmatrix} T_1\, U^1 & T_2\, U^1 \\ T_1\, U^2 & T_2\, U^2 \end{bmatrix} \ . \tag{2.14}$$

2.1.6 Manifolds and tangent spaces

In the above discussion, we always assume a general vector space V. However, in general relativity the more general concept of *manifolds* is needed (see section 2.2.1). An n-dimensional manifold, M, is a topological space that locally resembles $\mathbb{R}^n$. Specifically, near each point $p \in M$ there is a neighbourhood that is *homeomorphic* to an open subset of $\mathbb{R}^n$. Recall that two spaces, X, Y, are homeomorphic if there is a bijective map $f : X \to Y$ such that f and f^{-1} are both continuous. This concept allows for the use of local properties of $\mathbb{R}^n$ without making global assumptions on the structure of spacetime.

Note that a manifold is not a vector space. For example, the sphere, $S = \{(x, y, z) \in \mathbb{R}^3 | x^2 + y^2 + z^2 = 1\}$, is not a vector space since there is no natural way of adding two points $p, q \in S$ such that $p + q \in S$. Locally, however, the surface of the sphere will look like $\mathbb{R}^2$. This can be made precise with the notion of a *tangent space*, V_p, at the point $p \in M$. Briefly, the tangent space, V_p, consists of all *tangent vectors* at p. Since it is not the focus of this report, readers are referred to [1, Chapter 2] for details on how this is formally defined. Nevertheless, the tangent space V_p has the properties of a vector space and by assigning a tensor over V_p for each point $p \in M$, a *tensor field* is defined. Moreover, the tangent spaces V_p of all points $p \in M$ can be collected into the so called *tangent bundle*, TM, which is itself a manifold. Specifically, $TM := \{(p, y) \,|\, p \in M, y \in V_p\}$.

2.1.7 Metric tensor

A *metric* is intuitively the infinitesimal squared distance associated with a infinitesimal displacement. This infinitesimal displacement can be described precisely by a tangent vector. The metric at $p \in M$ should thus be a linear map $g : V_p \times V_p \to \mathbb{R}$, which is a $(0, 2)$-tensor. Moreover, the metric needs to be symmetric ($g(v, w) = g(w, v)\ \forall v, w \in V_p$) and non-degenerate ($g(v, w) = 0\ \forall v \in V_p \iff w = 0$). The metric on a manifold is thus a symmetric, non-degenerate, (0,2)-tensor field. In particular, this means that a metric, g, on a manifold, M, is an inner product on V_p for each $p \in M$. Note that the inner product here is not assumed to be positive definite.

Now, let $x_0, \ldots, x_n$ be the coordinate basis. Then the metric tensor g_{ab} can be written in terms of its components, $g_{\mu\nu}$, as

$$g_{ab} = \sum_{\mu,\nu=1}^{n} g_{\mu\nu} dx^\mu dx^\nu \ . \tag{2.15}$$

Note that the metric tensor is sometimes also denoted ds^2.

For a metric g_{ab}, it is always possible to find an orthonormal basis $\{v_1, \ldots, v_n\}$ of V_p for each $p \in M$. Note that since positive definiteness is not assumed, an orthonormal basis fulfills

$$g(v_\mu, v_\nu) = \begin{cases} 0 & , \mu \neq \nu \\ \pm 1 & , \mu = \nu \end{cases} \ . \tag{2.16}$$

The number of + and − signs that occur in (2.16) is the *signature* of the metric. Positive definite metrics $(+ + \cdots +)$ are called *Riemannian*, while metrics of the form $(- + + \cdots +)$ are called *Lorentzian*.

2.1.8 Metric tensor operation

Above, we define the metric tensor g_{ab} as a linear map, $g : V_p \times V_p \to \mathbb{R}$. However, recall from section 2.1.1 that such a tensor may also be viewed as a linear map from V_p to V_p^*, by $v \mapsto g(\cdot\,, v)$ (since $g(\cdot\,, v) : V_p \to \mathbb{R} \implies g(\cdot\,, v) \in V_p^*$). Here V_p^* is the dual tangent space, also known as the *cotangent space*. Due to non-degeneracy of the metric, this map is a bijection, meaning that the inverse map exists. There is thus a one-to-one correspondence between vectors and dual vectors through g_{ab}.

The inverse of g_{ab} is a $(2,0)$-tensor which we denote g^{ab}. As described above, by acting with g_{ab} on a vector v^a, we get a dual vector, which we denote v_a. This then defines the *index lowering* and *index raising* operations given by the metric. To clarify,

$$g_{ab}v^b =: v_a \ , \tag{2.17}$$

$$g^{ab}v_b =: v^a \ . \tag{2.18}$$

The same applies when the metric acts on a general tensor. For example, consider g_{ab} acting on the $(4,3)$-tensor $T^{cdbe}{}_{fgi}$. The result will be the $(3,4)$-tensor $T^{cd\ e}{}_{a\ fgi}$, i.e.

$$g_{ab}T^{cdbe}{}_{fgi} = T^{cd\ e}{}_{a\ fgi} \ . \tag{2.19}$$

2.2 Spacetime structure

The dimensions of space and time can be put together to form a continuum of *events*, known as spacetime. Each event is a point of space, (x, y, z), at an instance of time, t. In pre-relativistic physics, spacetime was divided into three parts. Past events, future events and simultaneous events. The past and future events were divided by the hyperplane of simultaneous events. If the event p lies in the present, it was thought that any observer in the past could go to p and that an observer of p could go to any point in the future. It was, however, impossible for an observer to be at two different simultaneous events. This structure is illustrated in Figure 2.1a.

When special relativity was presented, and it was understood that nothing can travel faster than the speed of light, this picture changed. Only material particles in the *past light cone* could go to the event p, and a material particle at p could only go to events in the *future light cone*. The boundary of the future light cone are events that could be reached by light emitted from p, and similarly the boundary of the past light cone are events from which light can reach p. These events are called *lightlike* or *null* related to p. The concept known as *null infinity* is the abstract region where a lightlike path ends up in infinite time. Events outside of the light cones are said to be *spacelike* related to p and can never affect the future of p. Events within the cones are instead said to be *timelike* related to p. This is illustrated in Figure 2.1b.

Note that there is no notion of absolute simultaneity in special relativity, since time depends on the observer.

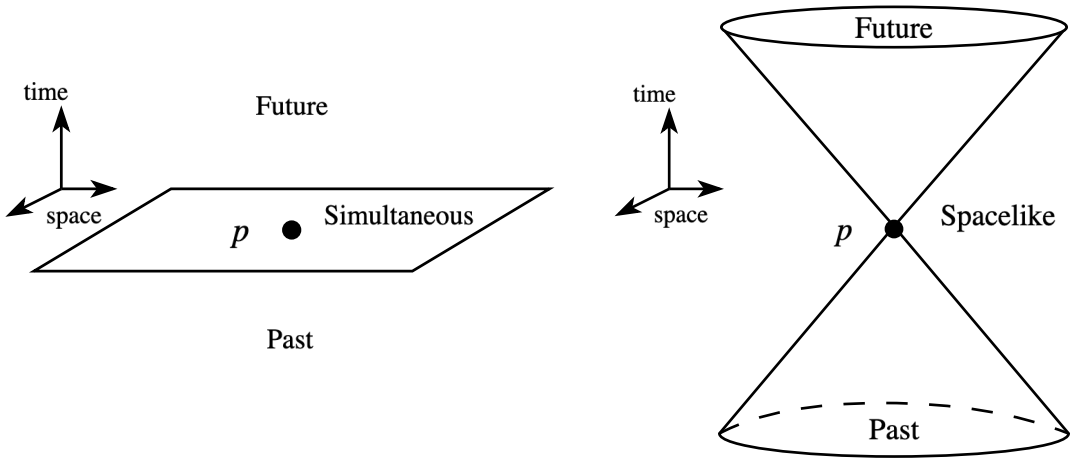

(a) Pre-relativistic picture **(b)** Special relativity

Figure 2.1: Spacetime structure in pre-relativistic physics and special relativity.

In general relativity, the picture becomes more complicated due to the curvature of spacetime. The central idea of general relativity is that gravitational forces are not properties of a gravitational field, but rather properties of the structure of spacetime itself. The curvature of spacetime depends on the matter content, as described by the EFE in (1.1). In the presence of matter, the light cones in Figure 2.1b are therefore altered and point more inward towards the mass. The extent of this alteration depends on the size of the mass, and in a black hole, the curvature is so large that all of the light cone points inwards. This is explained more formally in section 2.3.1. The remainder of this section is devoted to presenting the mathematical structures needed to handle curved spacetimes by concretising concepts from section 2.1.

2.2.1 Spacetime manifold

In pre-relativistic physics and special relativity it is assumed that any event in spacetime can be characterised by four numbers, (t, x, y, z). Hence, spacetime is in one-to-one correspondence to $\mathbb{R}^4$. However, in general relativity, no such global assumptions are made. Instead, spacetime is assumed to be a 4-dimensional manifold, which allows the use of local properties of $\mathbb{R}^4$ without making global assumptions on the structure of spacetime. Moreover, this allows for the spacetime to be curved. Specifically, spacetime is a manifold with a Lorentz metric g_{ab} (see section 2.1.7).

2.2.2 Spacetime metric

In pre-relativistic physics, both the time interval between events, Δt, and the spatial interval between simultaneous events, $|\Delta \mathbf{x}|$, are observer independent. The distance between events in spacetime can thus be defined as in Euclidean space. However,

in special relativity, neither Δt nor $|\Delta \mathbf{x}|$ are observer independent. Instead, the *spacetime interval*,

$$I = -(\Delta t)^2 + \frac{1}{c^2}\left[(\Delta x)^2 + (\Delta y)^2 + (\Delta z)^2\right], \tag{2.20}$$

is the observer independent quantity. Here c is the speed of light. By considering infinitesimal changes, this can be defined as the *metric of spacetime* in special relativity. The path of an inertial observer in this spacetime is a *geodesic* of the spacetime metric, and the curvature associated with the metric is *flat*. Remember that a geodesic is the curve that represents the shortest path between two points in a manifold. Note as well that the spacetime metric is a Lorentzian metric of signature $(-+++)$. The flat spacetime of special relativity is also known as the *Minkowski spacetime*. The concepts of spacelike, timelike or lightlike (null) paths can be specified as if the spacetime interval of the path is > 0, < 0 or $= 0$ respectively.

In general relativity, the observer independent properties of spacetime are also described by the spacetime metric and the paths of inertial observers are given by geodesics of the spacetime metric. However, since gravity is a consequence of the curvature of spacetime, the flat metric of special relativity can not be the spacetime metric of general relativity. Moreover, since the curvature of spacetime depends on the matter content of spacetime (as postulated in the EFE), the spacetime metric is not just a set arena, but instead a dynamical variable that changes with the matter content. Hence, to solve the EFE for the motion of matter, the equations need to be solved for both the metric and the matter distribution simultaneously.

2.2.2.1 Geodesics equation

Given a coordinate basis, $\{x^1, \ldots, x^n\}$, a geodesic of a metric can be mapped onto a curve, $x^\mu(\tau)$, parametrised by some τ. The curve can be determined by the *geodesic equation*

$$\frac{d^2x^\mu}{d\tau^2} + \Gamma^\mu{}_{\sigma\nu}\frac{dx^\sigma}{d\tau}\frac{dx^\nu}{d\tau} = 0\,, \tag{2.21}$$

where $\Gamma^\mu{}_{\sigma\nu}$ is the *Christoffel symbol* specified in (2.35). Given initial values for x^μ and $\frac{dx^\mu}{d\tau}$, (2.21) has a unique solution [1]. As discussed above, a *null* geodesic must also satisfy

$$g_{\mu\nu}\frac{dx^\mu}{d\tau}\frac{dx^\nu}{d\tau} = 0\,. \tag{2.22}$$

2.2.2.2 Schwarzschild solution

To concretise the notion of a spacetime metric, we consider the Schwarzschild solution, presented by Schwarzschild in 1916. Schwarzschild considered a *static*, *spherically symmetric* case. In a static spacetime, all metric components are independent of t and the geometry is unchanged by time-reversal ($t \to -t$). The concept of static spacetimes will not be explained further in this context, and readers are referred to [1, Chapter 6.1] for more details. However, since this thesis is also concerned with spherically symmetric spacetimes, more effort is put into explaining this concept.

The physical interpretation of spherical symmetry is that the spacetime metric is invariant under rotations. The spacetime metric then induces a metric on each orbital sphere. Due to the symmetry, the induced metric must be a multiple of the metric on the unit sphere and can thus be characterised by the area, A_S, of the orbit sphere. For this, we define the *area radius* as

$$r := \left(\frac{A_S}{4\pi}\right)^{\frac{1}{2}} . \tag{2.23}$$

Note that, in Euclidean space, the area radius is just the radius of the sphere, but this is not necessarily true in curved space.

In spherical coordinates, (r, θ, ϕ), the metric on each orbit sphere becomes

$$ds^2 = r^2(d\theta^2 + \sin^2(\theta)d\phi^2) , \tag{2.24}$$

where $r \geq 0$, $\theta \in [0, \pi]$ and $\phi \in [0, 2\pi]$. To choose coordinates for the entire spacetime, we choose an initial sphere with spherical coordinates. These coordinates are then translated along the geodesics orthogonal to the initial sphere to spheres with different r. This method is described more thoroughly in [1, Chapter 6.1], but the resulting spacetime metric for a static, spherically symmetric spacetime in (t, r, θ, ϕ) coordinates is

$$ds^2 = -h_1(r)dt^2 + h_2(r)dr^2 + r^2(d\theta^2 + \sin^2(\theta)d\phi^2) . \tag{2.25}$$

Here r, θ and ϕ are as before, while $t \in \mathbb{R}$. For clarity, this is written in tensor form as

$$g_{ab} = \begin{bmatrix} -h_1(r) & 0 & 0 & 0 \\ 0 & h_2(r) & 0 & 0 \\ 0 & 0 & r^2 & 0 \\ 0 & 0 & 0 & r^2\sin^2(\theta) \end{bmatrix} , \tag{2.26}$$

in accordance with (2.15). Note that the functions h_1 and h_2 do not depend on t, since the metric is static. Morover, these functions are determined by solving the Einstein field equations. By solving for a vacuum case ($T_{ab} = 0$) they become

$$h_1(r) = \left(1 - \frac{2M}{r}\right) , \; h_2(r) = \left(1 - \frac{2M}{r}\right)^{-1} , \tag{2.27}$$

where M is the total mass of the Schwarzschild field. This mass is defined by coinciding with Newtonian gravity for large r. This can be done due to *asymptotical flatness* of the metric, i.e. as $r \to \infty$ the metric will be that of special relativity in spherical coordinates (compare to (2.20) with $c = 1$). This is known as the *Arnowitt–Deser–Misner* (ADM) formalism of defining mass in general relativity.

By examining the functions h_1 and h_2 in equation (2.27), we see that the metric components become *singular* as $r = 2M$ or $r = 0$. The singularity at $r = 2M$ is caused by a breakdown of the coordinates, whereas the $r = 0$ singularity is a true singularity. The difference between a true singularity and a coordinate singularity is discussed further in section 2.2.3.

2.2.2.3 Painlevé-Gullstrand coordinates

An alternative coordinate system for the Schwarzschild solution is the *Painlevé-Gullstrand* (PG) coordinates, which are used in this thesis (see chapter 4). An advantage of using PG coordinates is that the Schwarzschild coordinate singularity at $r = 2M$ is removed. For instructive purposes, we here derive the Schwarzschild metric in PG coordinates. Starting from the Schwarzschild coordinates (t, r, θ, ϕ), let $\tilde{t} = t + \tau(r)$ for some function $\tau(r)$. In other words, consider the coordinate transform

$$\begin{aligned} \tilde{t} &= t + \tau(r)\,, \\ \tilde{r} &= r\,, \\ \tilde{\theta} &= \theta\,, \\ \tilde{\phi} &= \phi\,. \end{aligned} \tag{2.28}$$

The metric in the new coordinate system, $\tilde{g}_{\mu\nu}$, is given by the tensor transformation law in (2.5) as,

$$\tilde{g}_{\mu\nu} = g_{\alpha\beta}\frac{\partial x^\alpha}{\partial \tilde{x}^\mu}\frac{\partial x^\beta}{\partial \tilde{x}^\nu}\,, \tag{2.29}$$

where x is the original coordinates and $\tilde{x}$ the new ones. Note that only the diagonal elements of $g_{\alpha\beta}$ are non-zero (see (2.26)), and that the only non-zero partial derivatives are $\frac{\partial x^0}{\partial \tilde{x}^1} = \frac{\partial t}{\partial \tilde{r}} = -\tau'(r)$ and $\frac{\partial x^\alpha}{\partial \tilde{x}^\alpha}$ for $\alpha = 0, \ldots, 3$. By this, we get

$$\begin{aligned} \tilde{g}_{01} &= g_{00}\frac{\partial x^0}{\partial \tilde{x}^0}\frac{\partial x^0}{\partial \tilde{x}^1} = -h_1(r)\frac{\partial t}{\partial \tilde{t}}\frac{\partial t}{\partial \tilde{r}} = h_1(r)\tau'(r)\,, \\ \tilde{g}_{10} &= g_{00}\frac{\partial x^0}{\partial \tilde{x}^1}\frac{\partial x^0}{\partial \tilde{x}^0} = -h_1(r)\frac{\partial t}{\partial \tilde{r}}\frac{\partial t}{\partial \tilde{t}} = h_1(r)\tau'(r)\,, \\ \tilde{g}_{11} &= g_{00}\frac{\partial x^0}{\partial \tilde{x}^1}\frac{\partial x^0}{\partial \tilde{x}^1} + g_{11}\frac{\partial x^1}{\partial \tilde{x}^1}\frac{\partial x^1}{\partial \tilde{x}^1} \\ &= -h_1(r)\frac{\partial t}{\partial \tilde{r}}\frac{\partial t}{\partial \tilde{r}} + h_2(r)\frac{\partial r}{\partial \tilde{r}}\frac{\partial r}{\partial \tilde{r}} = -h_1(r)\left(\tau'(r)\right)^2 + h_2(r)\,, \\ \tilde{g}_{\mu\nu} &= g_{\alpha\beta},\ \text{if } \mu = \nu = \alpha = \beta = 0, 2, 3\,. \end{aligned}$$

By ignoring the tildes in the new coordinates, the Schwartzschild metric in PG coordinates becomes

$$ds^2 = -h_1(r)dt^{\,2} + 2\tau'(r)h_1(r)dtdr + \left[h_2(r) - h_1(r)\left(\tau'(r)\right)^2\right]dr^2 + r^2(d\theta^2 + \sin^2(\theta)d\phi^2)\,. \tag{2.30}$$

To simplify the expression, choose $\tau(r)$ such that $\tau'(r) = \sqrt{\frac{h_2(r)-a^2}{h_1(r)}}$, for some $a = a(r)$. Then, $a^2 = \left[h_2(r) - h_1(r)\left(\tau'(r)\right)^2\right]$. Furthermore, note that $h_1 \cdot h_2 = 1$ in the Schwarzschild solution (2.27), so

$$\begin{aligned} 2\tau'(r)h_1(r) =& 2\sqrt{\frac{h_2(r) - a^2}{h1_1(r)}}h_1(r) = 2\sqrt{(h_2(r) - a^2)h_1(r)} = 2\sqrt{1 - a^2h_1(r)} = \\ =& 2a^2\sqrt{\frac{1 - a^2h_1(r)}{a^4}} = 2a^2\beta\,, \end{aligned} \tag{2.31}$$

where $\beta := \sqrt{\frac{1-a^2 h_1(r)}{a^4}}$. Thus $h_1(r) = \left(\frac{1}{a^2} - \beta^2 a^2\right)$ and the metric can be written as

$$ds^2 = -\left(\frac{1}{a^2} - a^2\beta^2\right) dt^{\,2} + 2a^2\beta dt dr + a^2 dr^2 + r^2(d\theta^2 + \sin^2(\theta)d\phi^2)\ . \tag{2.32}$$

This derivation is mainly presented to show the form of the Schwarzschild metric in the PG coordinates. The exact form of the metric used in this thesis is presented in chapter 4.

2.2.3 Singularities and the Kretschmann scalar

A *singularity* is a *geodesically incomplete* point in spacetime, i.e. a point from which the geodesics can not be extended smoothly. As seen in section 2.2.2.2 and section 2.2.2.3, classifying when a singularity occurs is not trivial. The metric can become singular solely due to the chosen coordinate system, as the $r = 2M$ singularity in the Schwarzschild case. To remove such cases, a quantity that is invariant of the coordinates should be considered to define a singularity. One such choice is the *Kretschmann scalar*, which is defined by

$$K = R_{abcd}R^{abcd}\,, \tag{2.33}$$

where R_{abcd} is the *Riemann curvature tensor* of the spacetime manifold. At a singularity, the curvature becomes infinite which means that $K \to \infty$. In the Schwarzschild case, $K = 48M^2/r^6$, from which it follows that $r = 2M$ is not a real singularity.

2.3 Horizons and cosmic censorship

As shown in section 2.2.2.2, singularities appeared already in the first solution to the Einstein field equations presented by Schwarzschild in 1916. It was, however, not until 1939 that Oppenheimer and Snyder showed how matter could collapse to form what is now known as a *black hole*. The debate around the nature of singularities and black holes then really started kicking off in the 1960s, with e.g. the Kerr solution of a rotating black hole being presented in 1963. The purpose of this section is to introduce some important concepts needed to understand these discussions.

2.3.1 Trapped surfaces and horizons

A black hole is characterised by the formation of a *trapped surface*, which is a region in spacetime from which no particle, not even light, can escape. It is formed when matter becomes so concentrated, and thus the spacetime so curved, that all the null geodesics from the region converge. The boundary of the union of all trapped surfaces of a black hole is called the *apparent horizon*. It is defined as the boundary between where outward directed light rays actually move outwards and where they instead move inwards. An apparent horizon is thus a property of spacetime that is local in time. Its existence can be shown by showing that light rays originating in

the trapped surface always move inward, whereas light rays originating outside can move outwards. This is what is normally done in numerical relativity [11].

The more commonly known concept of an *event horizon*, is instead a global property of spacetime. An event horizon is defined as the boundary of a region from which light can not reach the future null infinity. In other words, a light ray originating from inside an event horizon can not escape even in infinite time. An event horizon can thus not be be located with local experiments in finite time. In stationary spacetimes an apparent horizon coincides with an event horizon, but this is not true in general. However, in the context of general relativity, the existence of an apparent horizon implies that a future event horizon will form outside of it [11].

2.3.2 Cosmic censorship

The notion that an event horizon forms around spacetime singularities is fundamental to the entire theory of general relativity. A singularity without an event horizon, from which light could escape to the future null infinity, is called a *naked singularity*. If naked singularities exist, it would lead to a breakdown of the predictability of the Einstein field equations. Predictability is a fundamental feature of a physical model, and in pre-relativistic physics, everything, past or present, can be predicted by the laws of physics given sufficient initial data. However, since the EFE "blow up" at a singularity, there would be no way of predicting the behaviour of a light ray or particle that escapes from a singular region.

By several researchers in the field, it had thus implicitly been assumed that an event horizon is always formed around a singularity so that no distant observer could see the singularity [12]. In 1969, Penrose [3] formulated this as a conjecture known as the *weak cosmic censorship conjecture* (WCCC). More specifically, in physical terms, it asserts that all physically realistic gravitational collapses are covered by an event horizon and hence can not be observed by a distant observer [12]. A more precise mathematical definition can be found in [1], but we highlight the requirement of regular, asymptotically flat initial data and a "suitable" matter model. Exactly what constitutes as a suitable matter model is not settled, but some conditions are that it is governed by deterministic equations and that it has locally positive energy density. Note that perfect fluid models, which can generate naked singularities, can obey both these conditions. In order to exclude these, some researchers have tried to impose extra conditions on the matter model in the conjecture [12].

In 1979, Penrose formulated another conjecture concerning the predictability of general relativity. In physical terms, it asserts that in *any* physically realistic spacetime, no singularity (apart from an initial "big bang") is ever visible to *any* observer [1]. In other words, it states that, despite singularities, the theory of general relativity is a generically deterministic theory. This conjecture is known as the *strong cosmic censorship conjecture* (SCCC), and again a more precise mathematical formulation can be found in [1]. Note that this conjecture is stronger than the WCCC in the sense that it applies to any observer in any spacetime, as opposed to a distant observer in an asymptotically flat spacetime.

Despite this, strong cosmic censorship does not in general imply weak cosmic censorship, since it is possible to construct examples that would obey the detailed conditions of the SCCC but not the detailed conditions of the WCCC. Weak cosmic censorship does also not imply strong cosmic censorship. Furthermore, in this thesis, only WCCC is considered. The SCCC is only presented in order to guide the reader who might encounter these concepts in other literature.

2.4 Einstein-Vlasov system

In this section, the Einstein-Vlasov system is introduced. First, the Einstein field equations and concepts concerning them are presented in some more detail. Then, kinetic theory and the Vlasov equation are introduced. Finally, we present how to use the Vlasov equation as a matter model in the EFE to form the Einstein-Vlasov system.

2.4.1 Einstein field equations

With geometrised units, the Einstein field equations are

$$R_{ab} - \frac{1}{2} R\, g_{ab} = 8\pi T_{ab} \ , \tag{2.34}$$

where R_{ab} is the *Ricci curvature tensor*, R is the *scalar curvature*, g_{ab} is the spacetime metric tensor and T_{ab} is the *stress-energy-momentum tensor*. The left hand side is also defined as the *Einstein tensor* G_{ab}. In cosmological solutions, there is a term of Λg_{ab} included in the left hand side to account for the acceleration of expansion of the universe. Λ is called the *cosmological constant* and is negligible at the scale of a galaxy or smaller. It is thus set to zero in this thesis. In general, (2.34) is a system of 10 coupled non-linear partial differential equations, where the metric g_{ab} is the unknown. Moreover, the system needs to be solved for the spacetime metric and the matter distribution simultaneously [1].

As discussed before, the left hand side of (2.34) describes the curvature of the spacetime. Since differential geometry is not the focus of this thesis, the definition of the Ricci curvature tensor from the Riemann curvature tensor is not covered, and readers are referred to [1, Chapter 3]. In simple terms, the Ricci tensor describes how a volume element in flat space changes due to curvature. The different tensor components represent the change along geodesics in different directions [13]. The scalar curvature is just the trace of the Ricci tensor, i.e. $R = R_a{}^a$. The Ricci tensor components can be expressed in terms of the *Christoffel symbol*, which is a tensor field associated to the derivative operator on the manifold and the coordinate system. Given a coordinate system $\{x^0, \dots, x^n\}$, the components of the Christoffel symbol can be expressed as

$$\Gamma^{\rho}{}_{\mu\nu} = \frac{1}{2} g^{\rho\sigma} \left(\frac{\partial g_{\nu\sigma}}{\partial x^{\mu}} + \frac{\partial g_{\mu\sigma}}{\partial x^{\nu}} - \frac{\partial g_{\mu\nu}}{\partial x^{\sigma}} \right) \ . \tag{2.35}$$

The dependence of R_{ab} on the metric is thus highly non-linear and involve derivatives up to second order [1].

In the right hand side of the equation, we find the stress-energy-momentum tensor, T_{ab}. It is a symmetric tensor and its components, $T_{\mu\nu}$, describe how energy[1] and momentum flow through a spacetime volume. The first index describes which component of the four-momentum is being considered, while the second describes in which spacetime direction the flow is. Note that the 0-th component of a four-momentum vector is the energy, while the others are the momentum in each spatial direction. The components of T_{ab} can then be identified as:

- T_{00} is the *energy density*, i.e. the energy per spatial volume unit.
- $T_{0\mu}$ is the *energy flux* in the μ-direction, i.e. energy flowing in a spatial direction.
- $T_{\mu 0}$ is the *momentum density* in the 0-direction, i.e. momentum flowing through time.
- $T_{\mu\mu}$ is the pressure (or force) in the μ direction.
- $T_{\mu\nu}$, $\nu \neq \mu$, is the *shear stress*, i.e. the rate of change of μ-momentum in the ν-direction.

Here the the indices μ, ν represent the spatial directions, i.e. $\mu, \nu = 1, 2, 3$.

The interpretation of these components depends on the chosen reference frame and coordinates, since in general relativity, the notion of time and space depend on the observer. To solve the EFE, the components of T_{ab} thus first have to be expressed in terms of g_{ab}. How this is done depends on which system is being studied, but in the end, a system of equations for the unknown metric g_{ab} is set up. For the Einstein-Vlasov system, this is done explicitly in section 2.4.3.

2.4.2 Kinetic theory and the Vlasov equation

Kinetic theory has been studied extensively as a mathematical subject for several decades. Its purpose is to model the time evolution of a system of particles, and it is, together with fluid models, one of the most used mathematical models for this. As described in the introduction, it is, for example, commonly used in the field of plasma physics. In plasma physics, the particles are electrons or ions whose interactions are governed by the Maxwell equations. In mathematical studies of general relativity, it is, however, more common to use simpler fluid models, even if interest in kinetic theory has increased in the last decades. In astrophysics, the particles can be considered to be stars and their interactions are governed by the Einstein field equations [8]. This section presents some general concepts about kinetic theory and the Vlasov equation.

In kinetic theory, the particles are modeled statistically. The particle system is described by a density function, $f = f(t, x, p)$, which represents the density of particles in *phase space* for a given time, t; position, x; and momentum, p [8]. Note that if there are three spatial dimensions, phase space is a six dimensional space with coordinates $(x^1, x^2, x^3, p^1, p^2, p^2)$. Macroscopic quantities of the system can be

[1]Note that in geometrised units ($c = 1$) energy and mass are the same, since $E = mc^2$.

calculated from f by integrating it with respect to momenta and some kernel $\kappa(p)$ [6]. This differs from fluid models, where the system quantities do not depend on p, only the spacetime-position (t, x) [8]. To clarify, the quantity $Q(t, x)$, related to the kernel $\kappa(p)$, can be calculated as

$$Q(t,x) = \int_{\mathbb{R}^3} \kappa(p) f(t,x,p) dp \ . \tag{2.36}$$

The energy density, $\rho(t, x)$, is given in the case where $\kappa(p) = 1$ [6]. This makes sense intuitively, since $\rho(t, x)$ is the particle density at spacetime position (t, x) for all particles, regardless of their momenta. To get $\rho(t, x)$, f is therefore integrated over all momenta at (t, x).

In 1938, Vlasov proposed a kinetic model with no direct interaction between particles, in order to model plasma more accurately. In particular, no collisions are included in the model, which differs from other models in kinetic theory based on the Boltzmann equation. Instead, each particle is acted on only by fields which are generated by all the particles collectively [7]. In this setting, the density function f is conserved along a flow-curve, $(x(t), p(t))$, in phase space. The *Vlasov equation* (also known as the *collisonless Boltzmann equation*) is then, in general, simply

$$\frac{d}{dt} f(t,x,p) = 0 \ , \tag{2.37}$$

which in a coordinate system $\{x^1, \ldots, x^n, p^1, \ldots, p^n\}$ becomes

$$\frac{\partial f}{\partial t} + \frac{dx^\mu}{dt}\frac{\partial f}{\partial x^\mu} + \frac{dp^\mu}{dt}\frac{\partial f}{\partial p^\mu} = 0 \ . \tag{2.38}$$

Note that the time derivative of the position, $\frac{dx}{dt}$, is the particle velocity and that the time derivative of momentum, $\frac{dp}{dt}$, is the force acting on the particle. This force is governed by the field generated by the collection of particles and can be denoted $F^a(t, x)$. With the velocity as v^a, the Vlasov equation can be written in its more familiar form

$$\frac{\partial f}{\partial t} + v^\mu \frac{\partial f}{\partial x^\mu} + F^\mu \frac{\partial f}{\partial p^\mu} = 0 \ . \tag{2.39}$$

This equation does not say much without putting it into a physical context where the field that generate $F^a(t, x)$ is specified. In the next section, we show how this is done in the case of general relativity.

2.4.3 Einstein-Vlasov equations

To present the Einstein-Vlasov system, we follow the review in [8]. Let M be a four dimensional manifold and g_{ab} a metric with signature $(- + ++)$. Assume all[2] particles have the rest mass m. The possible values of the four-momentum of a particle form a hypersurface in the tangent bundle called the *mass shell*. Denote

[2]It is possible to generalise the equations to particles of different masses, see [8].

the four-momentum p^a, the tangent bundle TM and the mass shell P_m. The mass shell is then defined by

$$P_m := \{(x^a, p^a) \in TM | g_{ab}(x^a)p^a p^b = -m^2c^2,\ p^a \text{ is future directed.}\}\,, \tag{2.40}$$

and can be understood as the set of all future directed timelike vectors with length cm. Note that in normalised units, $m = c = 1$, P_m is the set of all future directed unit vectors and if $m = 0$ it is the set of all future directed null vectors. Now introduce the local coordinates $(x^a, p^{\tilde{a}})$ on P_m, where $a = 0, 1, 2, 3$ and $\tilde{a} = 1, 2, 3$. That is, $x^0 = t$ is the time coordinate, whereas p^0 is expressed with $p^{\tilde{a}}$ and the metric using the relation $g_{ab}p^a p^b = -m^2c^2$.

Since the system considered is a collisionless gas, the particles can be considered free test particles in spacetime. They thus follow the geodesics of spacetime, which will be projections of the curves in P_m defined by

$$\begin{aligned} \frac{dx^a}{d\tau} &= p^a\,, \\ \frac{dp^{\tilde{a}}}{d\tau} &= -\Gamma^{\tilde{a}}{}_{bc}p^b p^c\,, \end{aligned} \tag{2.41}$$

where $\Gamma^{\tilde{a}}{}_{bc}$ is the Christoffel symbol. Since no collisions are included, the density function $f = f(x^a, p^{\tilde{a}})$ on P_m is invariant along the geodesics, which implies

$$\frac{d}{d\tau}f(x^a, p^{\tilde{a}}) = p^a\frac{\partial f}{\partial x^a} - \Gamma^{\tilde{a}}{}_{ab}p^a p^b\frac{\partial f}{\partial p^{\tilde{a}}} = 0\,. \tag{2.42}$$

This is the corresponding Vlasov equation, which can be compared to (2.39). To see this more clearly, let $x^0 = t$ and divide (2.42) by p^0. Then,

$$\frac{\partial f}{\partial t} + \frac{p^{\tilde{a}}}{p^0}\frac{\partial f}{\partial x^{\tilde{a}}} - \frac{1}{p^0}\Gamma^{\tilde{a}}{}_{bc}p^b p^c\frac{\partial f}{\partial p^{\tilde{a}}} = 0\,. \tag{2.43}$$

To couple the Vlasov equation to the Einstein equation, the stress-energy-momentum tensor T_{ab} needs to be expressed in terms of f and g_{ab}. This is done by

$$T_{\mu\nu} = c\sqrt{|g_{ab}|}\int_{\mathbb{R}^3} f p_\mu p_\nu \frac{1}{-p_0}dp^1 dp^2 dp^3\,, \tag{2.44}$$

where $|g_{ab}|$ is the absolute value of the determinant of g_{ab}. Remember that $p_a = g_{ab}p^b$. The equations (2.43) and (2.44) in (2.34) then constitute the Einstein-Vlasov system, with the unknowns being a non-negative function f defined on P_m and a Lorentz metric g_{ab} on the manifold M.

3

Particle In Cell method

In this chapter, the general scheme of the Particle In Cell (PIC) method is presented. The PIC method is mainly used for simulating systems with a large number of particles, $N \sim 10^5 - 10^{10}$, that interact via some force field. It is commonly used in, for example, plasma physics, where the Maxwell-Vlasov system is considered [14]. How the PIC method is applied to the Einstein-Vlasov system, is described in detail in section 5.1.

One of the advantages of the PIC algorithm is that the number of operations per time step is $\mathcal{O}(N\log(N))$, which can be compared to the $\mathcal{O}(N^2)$ calculations per time step needed in the naive approach of calculating the force generated by each pair of particles [15]. Other advantages include reducing the number of assumptions to a minimum and being able to simulate high dimensional cases [14]. It is, however, a relatively noisy method in the sense that a finer grid size does not necessarily translate continuously to more accurate results.

Due to the large number of particles considered, the physical particles are usually collected into *super-particles* which are used as computational particles. These "clouds" of physical particles can be thought of as pieces of phase space and their movement in phase space are determined by the PIC method. The PIC method can thus, in some sense, be thought of as a finite element method, where the elements themselves are moving [16]. In the following, the computational particles are just particles, regardless of whether they are physical particles or super-particles.

3.1 General setup

Starting from the Vlasov equation (2.39), this can be written in its characteristic form for each particle, $i = 1, \dots, N$, as

$$\begin{aligned} \frac{dx_i^a}{dt} &= p_i^a \,, \\ \frac{dp_i^a}{dt} &= F_i^a(t, x_i^a, p_i^a, B^a(Q)) \,, \end{aligned} \tag{3.1}$$

where we normalise $m = 1$ such that $v^a = p^a$. Note that the superscripts here follow abstract index notation and only indicate that we are dealing with vectors. F_i^a is as before the force acting on the particle. Moreover, B^a is some macro field which depends on some macro quantity of the particles, $Q = Q(t, x_i^a, p_i^a)$. For simplicity,

we assume that only one quantity is needed to determine B^a, but the same method is used if more quantities are needed. In this thesis, we assume that Q can be calculated as in (2.36), but in general, any rule for calculating Q from $x_1^a, \ldots, x_N^a, p_1^a, \ldots, p_N^a$ and B^a from Q would constitute a setup for a PIC method [14]. The total density function, $f(t, x, p)$, is considered to be the superposition of the density function of each particle, $f_i(t, x^a, p^a)$, i.e.

$$f(t, x^a, p^a) = \sum_{i=1}^{N} f_i(t, x^a, p^a) \tag{3.2}$$

[16] .

In the PIC algorithm, time is discretised into time steps, $t_k = t_0 + k\Delta t$, where $k = 0, 1, \ldots, N_t$ and Δt is the time interval. Furthermore, the spatial domain, Ω, is discretised into some grid elements $\Omega_1, \ldots, \Omega_{N_x}$. From these elements, a number of grid points $\chi_1^a, \ldots, \chi_{N_x}^a$ are defined (e.g. at the centre of each element). The particles are distributed onto phase space in some initial distribution and are given some *shape function*, which describes how it is spread out in phase space. As discussed previously, the particles can thus be thought of as clouds in phase space rather than point particles [14]. The time evolution of the particles is determined by an iterative scheme, where each of the steps presented in Figure 3.1 is performed in each time step. The PIC method can thus be broken down into four main steps: *particle weighting*, *field solver*, *field weighting* and *particle mover* [16]. The remainder of this section consists of a more detailed presentation of these steps.

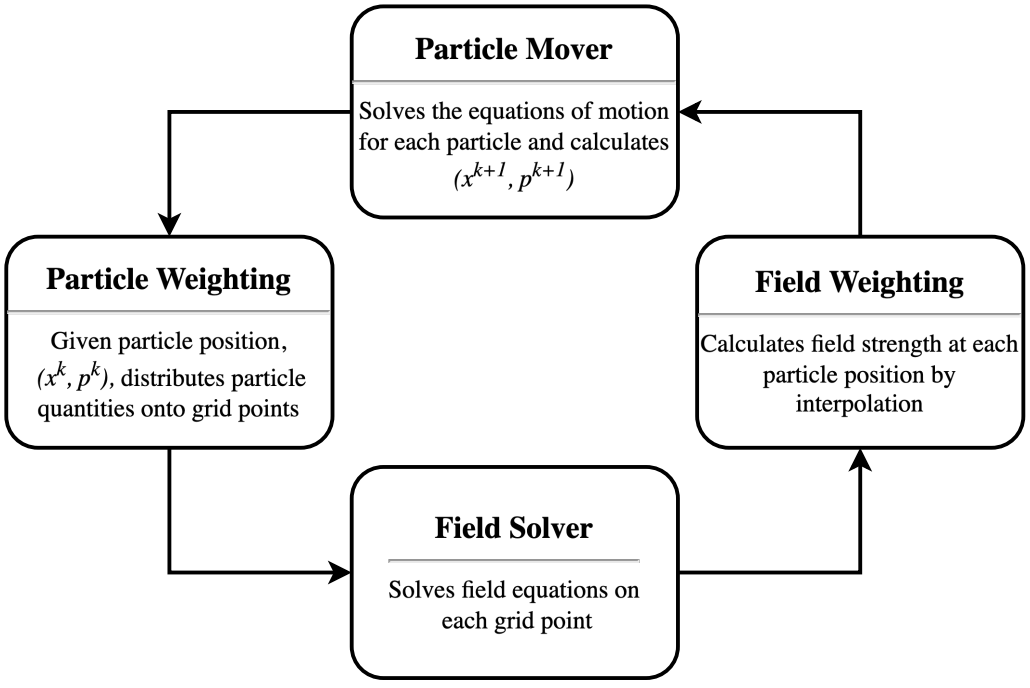

Figure 3.1: Iteration cycle for the k-th time step in the PIC method.

3.1.1 Particle weighting

The purpose of this step is to associate quantities depending on the particle position with the grid points $\chi_1^a, \ldots, \chi_{N_x}^a$. This is done by associating the particle densities with some shape function in phase space, i.e.

$$f_i(t, x^a, p^a) = W_i S_x(x^a - x_i^a(t)) S_p(p^a - p_i^a(t)) \,, \tag{3.3}$$

where x_i^a, p_i^a are the position and momentum of the particle and W_i is the *weight* of the particle. The weight is defined as

$$W_i = f(t, x_i^a, p_i^a) dV_i \,, \tag{3.4}$$

where dV_i is the phase space volume element occupied by the particle. Note that dV_i is invariant in time, meaning that only the initial volume element is needed. In standard PIC, the momentum shape function, S_p, is defined by a Dirac delta as $S_p = \delta(p^a - p_i^a)$, which means that all physical particles in the computational particle have the same velocity [17]. The spatial shape function, S_x, has to fulfill certain requirements and the choice of S_x strongly affects the stability and speed of the PIC simulation [14]. A common choice is to use the *b-spline* functions. The simplest b-spline, $b_0(\xi)$, is the so called *flat-top* function

$$b_0(\xi) = \begin{cases} 1 & , |\xi| < \frac{1}{2} \\ 0 & , \text{else} \end{cases} \,. \tag{3.5}$$

The general b-splines, b_l, can be calculated from

$$b_l(\xi) = \int_{-\infty}^{\infty} b_0(\xi - \xi') b_{l-1}(\xi') d\xi' \,, \tag{3.6}$$

and b_1 is commonly referred to as the *hat* function,

$$b_1(\xi) = \begin{cases} 1 - |\xi| & , |\xi| < 1 \\ 0 & , \text{else} \end{cases} \,. \tag{3.7}$$

Let Δ_p be the scale-length of the *support* (or size) of the particle, then the shape function based on the l-th b-spline can be defined as

$$S_x(x^a - x_i^a) := \frac{1}{\Delta_p} b_l \left(\frac{x^a - x_i^a}{\Delta_p} \right) \tag{3.8}$$

[16]. Now, let Q be a relevant quantity needed to calculate the field B^a. By (2.36), this can be calculated for each particle as

$$Q_i(t, x^a) = \int_{\mathbb{R}^3} \kappa(p^a) f_i(t, x^a, p^a) dp^a = \kappa(p_i^a(t)) W_i S_x(x^a - x_i^a(t)) \,, \tag{3.9}$$

where the function forms in (3.3) have been used. The total distribution of Q is given by summing over all particles as

$$Q(t, x^a) = \sum_{i=1}^{N} \kappa(p_i^a(t)) W_i S_x(x^a - x_i^a(t)) \,. \tag{3.10}$$

The value of Q at the grid point χ_m^a is then taken as the average over the spatial grid element Ω_m. Specifically, if V_m is the volume of Ω_m, we have

$$\begin{aligned} Q(t, \chi_m^a) &= \sum_{i=1}^{N} \kappa(p_i^a(t)) W_i \frac{1}{V_m} \int_{\Omega_m} S_x(x^a - x_i^a(t)) dx \\ &= \frac{1}{V_m} \sum_{i=1}^{N} \kappa(p_i^a(t)) W_i Z_x(\chi_m^a - x_i^a(t)) \,. \end{aligned} \tag{3.11}$$

Here, Z_x is the *interpolation function* [17]. Note that in some literature (e.g. [14]) Z is called the shape function. If S_x is defined as in (3.8) and $\Delta_p = \Delta x^a$, where Δx^a is the size of the grid element, we get Z_x as

$$Z_x(\chi_m^a - x_i^a(t)) = b_{l+1}\left(\frac{\chi_m^a - x_i^a}{\Delta x^a}\right), \tag{3.12}$$

which follows from (3.6) [17].

The particle weighting process can be illustrated in one dimension as in Figure 3.2. The density from the particle centered at position x_1 is described by the shape function in (3.8) with $l = 0$ and $\Delta_p = \Delta x$. The interpolation function, Z_x, is thus the hat function defined in (3.7). Due to the symmetry in this setting, the value of the interpolation function at the grid points, is the same as the fractional distance from x_1 to χ_2 and χ_1 respectively. More clearly, $Z_x(\chi_1 - x_1) = \frac{|\chi_2 - x_1|}{\Delta_p}$ and $Z_x(\chi_2 - x_1) = \frac{|\chi_1 - x_1|}{\Delta_p}$. In particular, this allows for quick calculations of the desired quantities at the grid points by the weighted average of the distances from x_1 to its closest grid points, i.e. by linear interpolation. Due to its simplicity and accuracy, the hat function is the most commonly used interpolation function in PIC implementations and it is commonly known as the *cloud in cell* scheme [14, 15, 16, 17].

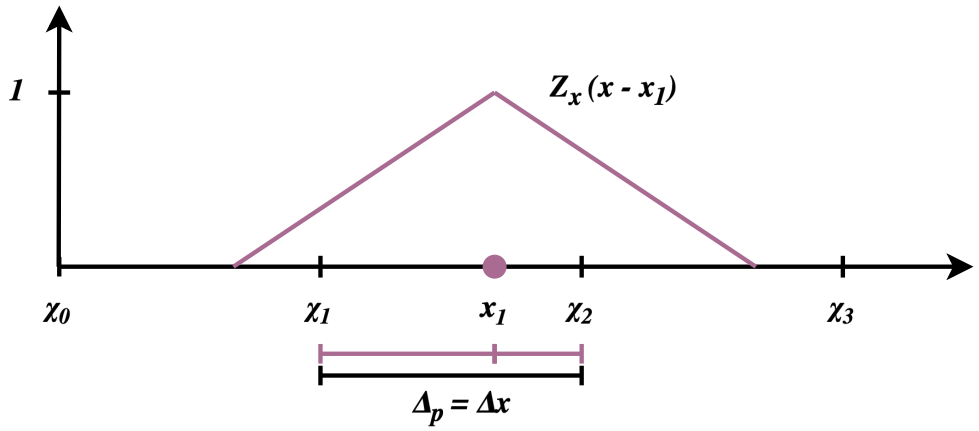

Figure 3.2: Illustration of the particle weighting step in a one dimensional grid. The density of particles centered at x_1 is described by a b-spline interpolation function of order 1. In this setting, with $\Delta_p = \Delta x$, the value of the shape function at the grid points closest to x_1, is directly proportional to the distance between x_1 and the grid points.

3.1.2 Field solver

After distributing the quantities to the grid points $\chi^a_1, \ldots, \chi^a_{N_x}$, the field equations are solved at each grid point [14]. The method for this depends on the field equations of the system considered and will thus not be specified in this general overview. For the system considered in this thesis, details are given in section 5.1.2.2

3.1.3 Field weighting

From the field solver, the field is known at the discrete grid points $\chi^a_1, \ldots, \chi^a_{N_x}$. Since the particles are not necessarily placed exactly on the grid points, the field needs to be extended to any point. In other words, we want to go from discrete $B^a(\chi^a_1), \ldots, B^a(\chi^a_{N_x})$ to continuous $B^a(x^a)$ [14]. This is usually done by assuming that the field is constant in each cell and that the value is that of the cell averaged value obtained at the grid point. The field strength at the particle centered at x^a_i is then calculated by averaging over the shape of the particle in phase space. If S_x is chosen as in (3.8) and $\Delta_p = \Delta x^a$, this is given by

$$B^a(x^a_i) = \sum_{m=1}^{N_x} B^a(\chi^a_m) Z_x(\chi^a_m - x^a) \,, \tag{3.13}$$

where Z_x is the interpolation function in (3.12) [17]. From this, the force, F^a_i, acting on each particle can be calculated. Everything in (3.1) is now known, and the new positions can be calculated [14].

3.1.4 Particle mover

The purpose of the particle mover is to update the position and momenta of every particle. This is done by discretising and solving (3.1). In the simplest case, this can be done by simply using the values at the previous time step as

$$\begin{aligned} x^a_i(t_{k+1}) &= x^a_i(t_k) + p^a_i(t_{k+1/2})\Delta t \,, \\ p^a_i(t_{k+1}) &= p^a_i(t_k) + F_i(t_k, x^a_{i,k}, p^a_{i,k}, B^a(Q_k))\Delta t \,. \end{aligned} \tag{3.14}$$

In more advanced implementations, it is common to use more sophisticated techniques to achieve higher accuracy. One such alternative is a *leap-frog* method, which achieves second order accuracy by calculating the momenta at half time steps. However, the particle mover is the most time consuming part of the PIC method, since it needs to be applied to every particle and the number of particles is usually large. It must therefore be fast and is generally where most optimisation efforts are put [14].

With the new coordinates for each particle, $x^a_i(t_{k+1})$, the particle quantities can be distributed onto the grid points by particle weighting. Hence, the cycle can be repeated for each time step until the final time t_{N_t} is reached.

4

Main system in Painlevé-Gullstrand coordinates

In this thesis, the system considered is that presented in [9]. The aim of this chapter is to give an overview of how these equations are derived from the general Einstein-Vlasov system. Moreover, we present the corresponding Einstein-dust system and specifically the homogeneous Oppenheimer-Snyder and inhomogeneous Eardly-Smarr cases which are studied in this thesis.

The system is considered in PG coordinates, (t, r, θ, ϕ), where $t \in \mathbb{R}$, $r \geq 0$, $\theta \in [0, \pi]$ and $\phi \in [0, 2\pi]$. We are interested in a non-static spacetime and consider a spacetime metric of the form

$$ds^2 = -\left(1 - a^2\beta^2\right) dt^2 + 2a^2\beta dt dr + a^2 dr^2 + r^2(d\theta^2 + \sin^2(\theta)d\phi^2) \,, \tag{4.1}$$

where $a = a(t, r)$ and $\beta = \beta(t, r)$. To get asymptotic flatness and regularity at the center we impose the boundary conditions

$$\beta(t, 0) = \beta(t, \infty) = 0 \,, \; a(t, 0) = a(t, \infty) = 1 \,. \tag{4.2}$$

Note that as $a = 1$ and $\beta = 0$ the flat Minkowski spacetime is recovered. For clarity, the unknowns are a and β, so to solve the system, these need to be determined. Note that if $a = 1$ and $\beta = \sqrt{\frac{2M}{r}}$, the Schwarzchild solution in (2.32) is recovered.

4.1 Einstein-Vlasov system

In [9], the density function, f, is chosen to be defined on the cotangent bundle, TM^*, instead of the tangent bundle as in section 2.4.3. Similarly to the tangent bundle, TM^* is the bundle of all dual tangent spaces at each $p \in M$. With the particle mass, m, and the speed of light, c, normalised to 1, the mass shell is defined as

$$P_m^* := \{(x^a, p_b) \in TM^* | g^{ab}(x^a)p_a p_b = -1, \; p^a \text{ is future directed.}\} \,. \tag{4.3}$$

Like in section 2.4.3, local coordinates are chosen as $(x^a, p_{\tilde{b}})$ with p^0 expressed by the metric. The geodesic equations become

$$\begin{aligned} \frac{dx^a}{d\tau} &= p^a = g^{ab}p_b \,, \\ \frac{dp_{\tilde{a}}}{d\tau} &= -\frac{1}{2}\frac{\partial g^{bc}}{\partial x^{\tilde{a}}} p_b p_c \,, \end{aligned} \tag{4.4}$$

which correspond to the characteristic equations of the Vlasov equation when f is supported on P_m^*.

We choose a reference frame such that p_1 is the radial momentum coordinate. If w is the radial momentum, we have $p_1 = aw$. The angular momentum, $L := (p_2)^2 + \frac{1}{\sin^2(\theta)}(p_3)^2$ is conserved along the geodesics by spherical symmetry. Furthermore, from the definition of P_m^* we have $g^{\mu\nu}p_\mu p_\nu = -1$. The only non-zero elements of the inverse metric, g^{ab}, are the diagonal elements $g^{\mu\mu}$ and the off-diagonal g^{10}, g^{01}. Thus,

$$\begin{aligned}
-1 &= g^{00}p_0p_0 + g^{01}p_0p_1 + g^{10}p_1p_0 + g^{11}p_1p_1 + g^{22}p_2p_2 + g^{33}p_3p_3 \\
-1 &= -(p_0)^2 + 2\beta p_0p_1 - \left(\frac{1}{a^2} - \beta^2\right)(p_1)^2 + \frac{1}{r^2}(p_2)^2 + \frac{1}{r^2\sin^2(\theta)}(p_3)^2 \\
-1 &= -(p_0)^2 + 2\beta p_0p_1 - \beta^2(p_1)^2 + \left(\frac{1}{a^2}\right)(p_1)^2 + \frac{1}{r^2}(p_2)^2 + \frac{1}{r^2\sin^2(\theta)}(p_3)^2 \\
-1 &= -\left(-p_0 + \beta p_1\right)^2 + w^2 + \frac{L}{r^2} \\
-1 &= -\left(g^{0\mu}p_\mu\right)^2 + w^2 + \frac{L}{r^2} \\
\implies p^0 &= \sqrt{1 + w^2 + \frac{L}{r^2}}\,.
\end{aligned} \tag{4.5}$$

Note the first term inside the square of p^0 represents the particle mass, $m = 1$.

With f defined on TM^*, the equivalent of (2.44) is

$$T_{\mu\nu} = \sqrt{|g^{ab}|}\int_{\mathbb{R}^3} f p_\mu p_\nu \frac{1}{p^0} dp_1 dp_2 dp_3\,. \tag{4.6}$$

From this, the non-trivial elements of T_{ab} can be calculated as

$$\begin{aligned}
T_{00} &= \rho - 2a\beta j + a^2\beta^2 p\,, \\
T_{01} &= -aj + a^2\beta p\,, \\
T_{11} &= a^2 p\,, \\
T_{22} &= r^2 p_T\,,
\end{aligned} \tag{4.7}$$

where we define ρ, j, p and p_T as

$$\begin{aligned}
\rho(t,r) &:= \frac{\pi}{r^2}\int_{-\infty}^{\infty}\int_0^\infty p^0 f(t,r,w,L)\,dL\,dw\,, \\
j(t,r) &:= \frac{\pi}{r^2}\int_{-\infty}^{\infty}\int_0^\infty w f(t,r,w,L)\,dL\,dw\,, \\
p(t,r) &:= \frac{\pi}{r^2}\int_{-\infty}^{\infty}\int_0^\infty \frac{w^2}{p^0} f(t,r,w,L)\,dL\,dw\,, \\
p_T(t,r) &:= \frac{\pi}{2r^4}\int_{-\infty}^{\infty}\int_0^\infty \frac{L}{p^0} f(t,r,w,L)\,dL\,dw\,.
\end{aligned} \tag{4.8}$$

In words: ρ is the energy density, j is the current of particles, p is the radial pressure and p_T is the tangential pressure. For instructive purposes, the derivation of the

expression for T_{00} in (4.7) is presented here. The others elements in (4.7) can be derived in similar fashion. To calculate T_{00}, we first need to find an expression for p_0. By the metric identities,

$$\begin{aligned} &\begin{cases} p_0 = g_{0\mu}p^\mu = g_{00}p^0 + g_{01}p^1 = -(1-a^2\beta^2)p^0 + a^2\beta p^1 \\ p^1 = g^{1\mu}p_\mu = g^{10}p_0 + g^{11}p_1 = \beta p_0 + \left(\frac{1}{a^2} - \beta^2\right) p_1 \end{cases} \\ \implies p_0 &= \frac{1}{1-a^2\beta^2}\left[-(1-a^2\beta^2)p^0 + (1-\alpha^2\beta^2)\beta p_1\right] = -p^0 + \beta p_1 \,. \end{aligned} \tag{4.9}$$

With this in (4.6), we get

$$\begin{aligned} T_{00} &= \frac{1}{r^2 a\sin(\theta)} \int_{\mathbb{R}^3} f(t,x,p) p_0 p_0 \frac{1}{p^0} dp_1 dp_2 dp_3 \\ &= \frac{1}{r^2 a\sin(\theta)} \int_{\mathbb{R}^3} f(t,x,p) \left(-p^0 + \beta p_1\right)^2 \frac{1}{p^0} dp_1 dp_2 dp_3 \\ &= \frac{1}{r^2 a\sin(\theta)} \int_{\mathbb{R}^3} f(t,x,p) \left(p^0 - 2\beta p_1 + \beta^2 (p_1)^2 \frac{1}{p^0}\right) dp_1 dp_2 dp_3 \\ &\vdots \\ &= \frac{\pi}{r^2} \int_{-\infty}^{\infty}\int_0^{\infty} f(t,r,w,L) \left(p^0 - 2a\beta w + a^2\beta^2 w^2 \frac{1}{p^0}\right) dL dw \\ &= \rho - 2a\beta j + a^2\beta^2 p \,, \end{aligned} \tag{4.10}$$

where the last step follows from the chosen definitions in (4.8). The steps resulting from the coordinate transform $(p_1, p_2, p_3) \mapsto (w, L, p_3)$ are presented in Appendix B.1.

4.1.1 Main system of equations

In the chosen coordinates, the Vlasov equation is given by

$$\frac{\partial f}{\partial t} + \left(\frac{w}{ap^0} - \beta\right)\frac{\partial f}{\partial r} + \left[\left(\frac{\beta}{a}\frac{\partial a}{\partial r} + \frac{\partial \beta}{\partial r} - \frac{1}{a}\frac{\partial a}{\partial t}\right) w + \frac{L}{ap^0 r^3}\right]\frac{\partial f}{\partial w} = 0 \,, \tag{4.11}$$

which gives the characteristic equations

$$\frac{dr}{dt} = \frac{w}{ap^0} - \beta \,, \tag{4.12}$$

$$\frac{dw}{dt} = \left(\frac{\beta}{a}\frac{\partial a}{\partial r} + \frac{\partial \beta}{\partial r} - \frac{1}{a}\frac{\partial a}{\partial t}\right) w + \frac{L}{ap^0 r^3} \,, \tag{4.13}$$

$$\frac{dL}{dt} = 0 \,. \tag{4.14}$$

Finally, in [9], they choose a suitable combination of the EFE and define the field equations of Einstein-Vlasov system as

$$\frac{\partial}{\partial t}\left(r(1-A)\right) = 8\pi r^2\left(\beta(\rho+p) - \left(a\beta^2 + \frac{1}{a}\right)j\right), \tag{4.15}$$

$$\frac{\partial}{\partial r}\left(r(1-A)\right) = 8\pi r^2(\rho - a\beta j), \tag{4.16}$$

$$\frac{\partial\beta}{\partial t} - \beta\frac{\partial\beta}{\partial r} = \frac{1}{2r}(1-A) + 4\pi r p, \tag{4.17}$$

$$\frac{\partial a}{\partial t} - \beta\frac{\partial a}{\partial r} = -4\pi r a^2 j, \tag{4.18}$$

where $A := \frac{1}{a^2} - \beta^2$. There is also a fifth equation including p_T, but since this is not relevant for the main system, it is only presented in (B.22). Note that with (4.18), the expression in (4.13) can be written as

$$\frac{dw}{dt} = 4\pi r a j w + \frac{\partial\beta}{\partial r}w + \frac{L}{ap^0 r^3}. \tag{4.19}$$

The system of (4.12), (4.19) and (4.15-4.18) coupled to the initial conditions,

$$\begin{aligned} a(0,r) &= 1, \\ \beta(0,r) &= \mathring{\beta}(r), \\ f(0,r,w,L) &= \mathring{f}(r,w,L), \end{aligned} \tag{4.20}$$

constitute the main system of equations considered in this thesis. Here, $\mathring{f}$ and $\mathring{\beta}$ are arbitrary initial functions which, in this thesis, are chosen in a specific way in order to approximate the dust model. See section 5.1.1 for details.

4.1.2 System mass and trapped surface condition

From (4.16), it follows that

$$A(t,r) = 1 - \frac{8\pi}{r}\int_0^r (\rho - a\beta j)_{(t,s)} s^2 ds\,. \tag{4.21}$$

By comparing to the Schwarzschild metric, we have $A = 1 - \frac{2M}{r}$. The mass of the system within radius r is thus given by

$$M(t,r) = 4\pi\int_0^r (\rho - a\beta j)_{(t,s)} s^2 ds\,. \tag{4.22}$$

The ADM mass, which is described briefly in section 2.2.2.2, represents the total mass of the system. From (4.22), we define it as

$$\mathcal{M}(t) := M(t,\infty) = 4\pi\int_0^\infty (\rho - a\beta j)_{(t,r)} r^2 dr\,. \tag{4.23}$$

If the spacetime is asymptotically flat and there is regularity at the centre, i.e. (4.2) is fulfilled, $\mathcal{M}$ is a conserved quantity. A derivation of this is presented in Appendix B.2. Finally, the condition for a trapped surface is given by

$$M(t,r) \geq \frac{r}{2}\,. \tag{4.24}$$

In words, this condition says that if enough mass M is confined into a small enough volume of radius r, the spacetime will get so curved that no particles or light can escape from within the volume.

4.1.3 Radial null geodesics

The null geodesics of the metric in (4.1) must fulfill (2.21) and (2.22). We are interested in outward pointing radial null geodesics, meaning that $\tau = r$ in (2.21) and (2.22). From (2.22), we get

$$\begin{aligned} 0 &= (-1+a^2\beta^2)\left(\frac{dt}{dr}\right)^2 + 2a^2\beta\frac{dt}{dr}\frac{dr}{dr} + a^2\left(\frac{dr}{dr}\right)^2 + r^2\cancel{\left(\frac{d\theta}{dr}\right)^2} + r^2\sin^2(\theta)\cancel{\left(\frac{d\phi}{dr}\right)^2} \\ 0 &= \left(\frac{dt}{dr}\right)^2 + \frac{2a^2\beta}{(-1+a^2\beta^2)}\frac{dt}{dr} + \frac{a^2}{(-1+a^2\beta^2)} \\ &\implies \frac{dt}{dr} = \frac{a}{1-a\beta}\,, \end{aligned} \tag{4.25}$$

where spherical symmetry is used in the first step. This can also be verified with the geodesic equation in (4.12). For a radial null geodesic, the angular momentum and mass are zero, which means $p^0 = \sqrt{0+w^2+0} = w$. Hence, (4.12) also gives

$$\frac{dr}{dt} = \frac{1}{a} - \beta \implies \frac{dt}{dr} = \frac{1}{\frac{1}{a}-\beta} = \frac{a}{1-a\beta}\,. \tag{4.26}$$

4.2 Einstein-Dust system

In this section, we introduce some important concepts and equations of the Einstein-Dust system. In the dust system, ρ is the only non-trivial matter quantity, which greatly simplifies the equations. The dust system can be recovered exactly from the Vlasov system above by letting $f(t,r,w,L) = \frac{1}{\pi}\delta(w^2+\frac{L}{r^2})\rho(t,r)$, where δ is the Dirac delta function. The density function is then not dependent on the momentum and all particles have the same velocity as in dust. From (4.8), we just get

$$\begin{aligned} \rho(t,r) &= \frac{1}{r^2}\int_{-\infty}^{\infty}\int_0^{\infty}\sqrt{1+w^2+\frac{L}{r^2}}\,\delta(w^2+\frac{L}{r^2})\rho(t,r)\,dL\,dw \\ &= \rho(t,r)\int_{-\infty}^{\infty}\int_0^{\infty}\sqrt{1+w^2+\frac{L}{r^2}}\,\delta(w^2+\frac{L}{r^2})\,d\frac{L}{r^2}\,dw \\ &= \rho(t,r)\,. \end{aligned} \tag{4.27}$$

From (4.8), it similarly follows that $j = p = p_T = 0$, which is exactly the case in the dust model. To initialise the Vlasov system arbitrarily close to dust, we thus set $\mathring{f} = \frac{1}{\pi}\delta(w^2 + \frac{L}{r^2})\mathring{\rho}(r)$, where $\mathring{\rho} = \rho(0, r)$.

In the remainder of this section, we present the dust solutions with homogeneous Oppenheimer-Snyder and inhomogeneous Eardly-Smarr initial data. The equations are presented in the framework of this thesis, which follows [9], since we will need them for our comparison to the Vlasov system. Specifically, we need to define the initial data $\mathring{\rho}$. A brief overview of the original Eardly-Smarr solution in comoving coordinates is given in Appendix C.

4.2.1 Oppenheimer-Snyder data

Oppenheimer and Snyder considered the collapse of a homogeneous dust cloud. This corresponds to the homogeneous initial energy density

$$\mathring{\rho}(r) = \begin{cases} \frac{\gamma}{3\pi} & , 0 \leq r \leq 1 \\ 0 & , \text{else} \end{cases} , \tag{4.28}$$

where γ is a parameter. To have regular initial data, γ needs to be chosen small enough to avoid an initial trapped surface. The condition for a trapped surface is that in (4.24), and the apparent horizon of the trapped surface which forms in the Oppenheimer-Snyder case is given by

$$t_H(r) = \frac{1}{\sqrt{2\gamma}} - \frac{2}{3}r \quad \text{for } r < r_b(t)\,. \tag{4.29}$$

Here, r_b is the *boundary radius* of the dust system which is given by

$$r_b(t) = (1 - \sqrt{2\gamma}t)^{\frac{2}{3}} \tag{4.30}$$

[9]. When $r_b(t) = 0$, i.e. at $t = \frac{1}{\sqrt{2\gamma}}$, all the dust particles have converged to the centre and we have "blow up". Note from (4.29), that the trapped surface is formed before the blow up time, so the singularity will always be shielded from any distant observer. For clarity, the trapped surface is given by the region $\{(t, r) \,|\, t > t_H(r), r < r_b(t_H(r))\}$, and thus the first (in time) point of the trapped surface is the intersection between $t_H(r)$ and $r_b(t)$. In other words, the trapped surface is formed when the particles have converged close enough to the centre.

4.2.2 Eardly-Smarr data

For Eardly-Smarr data, we start from the comoving framework presented in [4] and translate this into PG coordinates. For context, an overview of the original comoving framework is presented in Appendix C. To be consistent with the rest of the report, we let r be the area radius and denote the comoving radius by $\check{r}$. From the comoving metric in (C.1), it then follows that $r = Y(t, \check{r})$. Following [9], the metric transform

of (C.1) into (4.1) gives

$$a = X(t,\check{r})\left(\frac{\partial Y(t,\check{r})}{\partial \check{r}}\right)^{-1} \tag{4.31}$$

$$\beta = -\frac{\partial Y(t,\check{r})}{\partial t}\,. \tag{4.32}$$

From the Einstein-dust equations in (C.2), we have $X(t,\check{r}) = \frac{\partial Y(t,\check{r})}{\partial \check{r}}$, which means that $a = 1$ for dust. Furthermore, by (C.3), we have

$$Y(t,\check{r}) = \left(\frac{9}{2}\right)^{\frac{1}{3}} \mathring{M}(\check{r})^{\frac{1}{3}} \left(t_0(\check{r}) - t\right)^{\frac{2}{3}}\,, \tag{4.33}$$

where $\mathring{M}$ and t_0 are functions prescribing the initial data. Thus, β can be calculated from (4.32) and (4.33) as

$$\begin{aligned}\beta &= -\left(\frac{9}{2}\right)^{\frac{1}{3}} \mathring{M}(\check{r})^{\frac{1}{3}} \frac{2}{3} \left(t_0(\check{r}) - t\right)^{-\frac{1}{3}} (-1) \\ &= \frac{\frac{2}{3}\left(\frac{9}{2}\right)^{\frac{1}{3}+\frac{1}{6}} \mathring{M}(\check{r})^{\frac{1}{3}+\frac{1}{6}}}{\left(\frac{9}{2}\right)^{\frac{1}{6}} \mathring{M}(\check{r})^{\frac{1}{6}} \left(t_0(\check{r}) - t\right)^{\frac{1}{3}}} = \frac{\frac{2}{3}\left(\frac{9}{2}\right)^{\frac{1}{2}} \mathring{M}(\check{r})^{\frac{1}{2}}}{Y(t,\check{r})^{\frac{1}{2}}} = \sqrt{\frac{2\mathring{M}(\check{r})}{r}}\,,\end{aligned} \tag{4.34}$$

where the last step uses that $r = Y(t,\check{r})$. Note that $\check{r}$ will be a function of r and t, which needs to be determined.

In [9], they propose initial data on the form

$$\mathring{M}(\check{r}) = \begin{cases} \check{r}^3 & ,\, 0 \le \check{r} \le 1 \\ 1 & ,\, \check{r} > 1 \end{cases}\,, \quad t_0(\check{r}) = \begin{cases} \mathring{t} + \zeta \check{r}^p & ,\, 0 \le \check{r} \le 1 \\ \mathring{t} + \check{r}^2 - 1 + \zeta & ,\, \check{r} > 1 \end{cases}\,, \tag{4.35}$$

where $\zeta \ge 0$ and $p > 0$ are parameters and $\mathring{t} \ge 0$ is a constant. This is the same as proposed in [4], see (C.5), except for the constant time translation $\mathring{t}$. The physical singularity occurs when $t = t_0(\check{r})$, since the area radius $r = Y(t,\check{r})$ becomes zero for any constant matter shell $M(\check{r})$ with fixed $\check{r}$. In [4], $\mathring{t} = 0$, so the singularity is introduced in the centre at $t = 0$. This is unnatural for numerical simulations and by translating the time coordinate by $\mathring{t} > 0$, the simulations can instead start at $t = 0$ with regular initial data.

With (4.35) in (4.33) and $r = Y(t,\check{r})$, we get

$$r = Y(t,\check{r}) = c_0 \begin{cases} \check{r}(\mathring{t} + \zeta \check{r}^p - t)^{\frac{2}{3}} & ,0 \le \check{r} \le 1 \\ (\mathring{t} + \check{r}^2 - 1 + \zeta - t)^{\frac{2}{3}} & ,\check{r} > 1 \end{cases}\,, \tag{4.36}$$

where $c_0 := (9/2)^{\frac{1}{3}}$. From this, $\check{r}(t,r)$ can be determined. There is, however, no

explicit expression of $\check{r}(t,r)$ for general p. For simplicity, choose $p = 3/2$, so that

$$\begin{aligned} r &= c_0 \check{r} \left(\mathring{t} + \zeta \check{r}^{\frac{3}{2}} - t\right)^{\frac{2}{3}} \\ \left(\frac{r}{c_0}\right)^{\frac{3}{2}} &= \check{r}^{\frac{3}{2}} \left(\mathring{t} + \zeta \check{r}^{\frac{3}{2}} - t\right) \\ 0 &= \left(\check{r}^{\frac{3}{2}}\right)^2 + \frac{\mathring{t} - t}{\zeta} \check{r}^{\frac{3}{2}} - \frac{1}{\zeta}\left(\frac{r}{c_0}\right)^{\frac{3}{2}} \\ \check{r}^{\frac{3}{2}}(t,r) &= -\frac{\mathring{t} - t}{2\zeta} + \sqrt{\frac{(\mathring{t} - t)^2}{4\zeta^2} + \frac{1}{\zeta}\left(\frac{r}{c_0}\right)^{\frac{3}{2}}} \,. \end{aligned} \tag{4.37}$$

Note that from (4.36), $t = t_0(\check{r})$ implies that $r = 0$, meaning that the singularity will occur at $r = 0$ in PG coordinates. The boundary radius is where $\check{r} = 1$, i.e. at

$$r_b(t) = Y(t,1) = c_0(\zeta + \mathring{t} - t)^{\frac{2}{3}} \,. \tag{4.38}$$

Since $\check{r}$ is strictly increasing in r, $0 \leq \check{r} \leq 1 \iff 0 \leq r \leq r_b(t)$. Combining (4.35) and (4.37) in (4.34), we thus get

$$\beta(t,r) = \begin{cases} \sqrt{\frac{2}{r}} \check{r}^{\frac{3}{2}} = \sqrt{\frac{2}{r}} \left(-\frac{\mathring{t}-t}{2\zeta} + \sqrt{\frac{(\mathring{t}-t)^2}{4\zeta^2} + \frac{1}{\zeta}\left(\frac{r}{c_0}\right)^{\frac{3}{2}}} \right) & , 0 \leq r \leq r_b(t) \\ \sqrt{\frac{2}{r}} & , r > r_b(t) \end{cases} . \tag{4.39}$$

As for Oppenheimer-Snyder data, we wish to find an expression for the initial energy density $\mathring{\rho} = \rho(0,r)$. Noting that $j = 0$, in dust, the energy density can be calculated from (4.22) as

$$\rho(t,r) = \frac{1}{4\pi r^2} \frac{\partial M}{\partial r} \,. \tag{4.40}$$

By (4.37) in (4.35)

$$M(t,r) = \begin{cases} \check{r}^3(0,r) = \left(-\frac{\mathring{t}-t}{2\zeta} + \sqrt{\frac{(\mathring{t}-t)^2}{4\zeta^2} + \frac{1}{\zeta}\left(\frac{r}{c_0}\right)^{\frac{3}{2}}} \right)^2 & , 0 \leq r \leq r_b(t) \\ 1 & , r > r_b(t) \end{cases} , \tag{4.41}$$

which in (4.40) gives

$$\rho(t,r) = \begin{cases} \dfrac{3\left(-\frac{\mathring{t}-t}{2\zeta} + \sqrt{\frac{(\mathring{t}-t)^2}{4\zeta^2} + \frac{1}{\zeta}\left(\frac{r}{c_0}\right)^{\frac{3}{2}}} \right)}{8\pi c_0^{\frac{3}{2}} \zeta r^{\frac{3}{2}} \sqrt{\frac{(\mathring{t}-t)^2}{4\zeta^2} + \frac{1}{\zeta}\left(\frac{r}{c_0}\right)^{\frac{3}{2}}}} & , 0 \leq r \leq r_b(t) \\ 0 & , r > r_b(t) \end{cases} . \tag{4.42}$$

Finally, as for Oppenheimer-Snyder, it is in the dust case possible to find an analytical expression for the apparent horizon. It is given in [9] as

$$t_H(r) = \mathring{t} + \zeta\sqrt{\frac{r}{2}} - \frac{2}{3}r \quad \text{for } r < r_b(t) \,. \tag{4.43}$$

5

Numerical methods

In this chapter, the numerical methods used in this thesis are described. First, the PIC implementation used to simulate the Einstein-Vlasov system presented in 4.1 is described in detail. This is followed by a description of the parameter search and dust convergence simulations performed with homogeneous initial data. Finally, we describe the numerical convergence and cosmic censorship simulations performed using inhomogeneous initial data.

5.1 Particle In Cell implementation

In this section, the main numerical method used in this project is described. The description follows the general setup in chapter 3, but presents the different steps in the particular case considered. As in the general setup, the particles here represent the computational particles, which for our purposes can be thought of as stars. In order to simulate large numbers of particles efficiently, the PIC routine is implemented[1] in C with parallel processes through *pthreads*. The effect of this on the runtime is described briefly in section 5.1.3.

Due to spherical symmetry, only one spatial dimension needs to be considered. Namely, the area radius, r. Furthermore, we consider two coordinates, u and α, to span the momentum dimensions of phase space. Here, u is the norm of the momentum and α is the angle to the radial coordinate. In other words, $\alpha \in [0, \pi]$, describes how much of the momentum is pointing inwards or outwards from the centre. If $\alpha = \pi/2$, the momentum is purely tangential and if $\alpha = 0$ it is outwards radial. In these coordinates, w and L from section 4.1 can be expressed as

$$\begin{aligned} w &= u\cos(\alpha)\,, \\ L &= u^2 r^2 \sin^2(\alpha)\,, \end{aligned} \tag{5.1}$$

which in particular means that $u^2 = w^2 + \frac{L}{r^2}$.

5.1.1 Parameters and initialisation

In order to understand the PIC implementation and the results generated from it, we begin with a brief overview of the important simulation parameters. Firstly,

[1]Note that the implementation was provided by H. Andréasson. Only relatively minor modifications and bug fixes have been made by the author.

the spatial discretisation parameters are the interval $[r_{\min}, r_{\max}]$ and the number of grid points N_r. From these, the radial step length Δr, is given by $\Delta r = \frac{r_{\max} - r_{\min}}{N_r}$ and the grid points are $r_m = r_{min} + m\Delta r$ for $m = 0, \ldots, N_r$. Similarly, for the momentum space, N_u and N_α denote the number of grid points in these coordinates and $\Delta u = \frac{u_{\max}}{N_u}$, $\Delta\alpha = \frac{\pi}{N_\alpha}$. Importantly, $u_{\max}$ is controlled by the parameter ε as $u_{\max} = \sqrt{\varepsilon}$. This means that as $\varepsilon \to 0$, all the particles will have an initial relative momentum of 0, which is exactly the case in dust matter. The parameter ε thus describes the initial dispersion of the particle momenta. Finally, the time dimension is discretised by a final time, t_{final}, and the number of time steps, N_t. This gives $\Delta t = \frac{t_{\text{final}}}{N_t}$.

At $t = 0$, the initial distribution of particles is given by introducing one particle midway between each grid point in phase space. Specifically, one particle is introduced at every

$$\begin{aligned} \mathring{r}_i &= r_{\min} + (m - 0.5)\Delta r\,, \\ \mathring{u}_i &= (m_u - 0.5)\Delta u\,, \\ \mathring{\alpha}_i &= (m_\alpha - 0.5)\Delta\alpha\,, \end{aligned} \tag{5.2}$$

where $m = 1, \ldots, N_r$, $m_u = 1, \ldots, N_u$ and $m_\alpha = 1, \ldots, N_\alpha$. The total number of particles in the simulation is thus $N = N_r \cdot N_u \cdot N_\alpha$ and at each spatial grid point, r_m, there are $N_u \cdot N_\alpha$ particles with different momenta. The initial volume element occupied by the i-th particle is

$$d\mathring{V}_i = (4\pi\mathring{r}_i^2\Delta r)(2\mathring{u}_i^2 \sin(\mathring{\alpha}_i)\Delta u\Delta\alpha)\,. \tag{5.3}$$

Note that the first factor is the area of a sphere times a height Δr and that the second factor comes from the Jacobian of the coordinate transform in (5.1). The missing r^2 from the Jacobian is taken care of in (5.11).

The initial density distribution is given at each grid point by

$$\mathring{f}(r, u) = \mathring{\rho}(r) H\left(\frac{u^2}{\varepsilon}\right) \frac{1}{\pi\varepsilon\sqrt{\varepsilon}}\,, \tag{5.4}$$

where H is a sufficiently smooth non-negative function and $\mathring{\rho}$ is the initial energy density. Following [9], we define H as

$$H(\eta) = \begin{cases} \frac{105}{32}\,(1 - \eta)^2 & ,\eta < 1 \\ 0 & ,\text{else} \end{cases}\,. \tag{5.5}$$

Note that $H\left(\frac{u^2}{\varepsilon}\right)\frac{1}{\varepsilon\sqrt{\varepsilon}} \to \delta(u^2)$ as $\varepsilon \to 0$. As discussed in section 4.2, this would thus exactly recover the dust system initially if $\mathring{\rho}$ is chosen as the initial energy density in dust. Furthermore, since

$$2\int_0^1 \sqrt{\eta} H(\eta) d\eta = 1 \tag{5.6}$$

we have from (4.8) that

$$\begin{aligned}\rho(0,r) &= \frac{1}{\varepsilon\sqrt{\varepsilon}r^2}\int_{-\infty}^{\infty}\int_0^{\infty}\sqrt{1+w^2+\frac{L}{r^2}}H\left(\frac{w^2+\frac{L}{r^2}}{\varepsilon}\right)\mathring{\rho}(r)dLdw \\ &= \mathring{\rho}(r)\frac{1}{\varepsilon\sqrt{\varepsilon}r^2}\int_0^{\infty}\int_0^{\pi}\sqrt{1+u^2}H\left(\frac{u^2}{\varepsilon}\right)2u^2r^2\sin(\alpha)dud\alpha \\ &= \mathring{\rho}(r)\frac{4}{\varepsilon\sqrt{\varepsilon}}\int_0^{\infty}u^2\sqrt{1+u^2}H\left(\frac{u^2}{\varepsilon}\right)du \\ &= \mathring{\rho}(r)2\int_0^1\sqrt{\eta}\sqrt{1+\varepsilon\eta}H(\eta)d\eta \longrightarrow \mathring{\rho}(r) \text{ as } \varepsilon\to 0\,, \end{aligned} \tag{5.7}$$

in accordance with (4.27). Note that first the coordinate transform in (5.1) and then $\eta = u^2/\varepsilon$ is used. To initialise the Vlasov system with dust-like initial data we thus set $\mathring{\rho}$ as in the corresponding dust case. The exact choices of $\mathring{\rho}$ for homogeneous and inhomogeneous initial data are specified in section 5.2 and 5.3 respectively.

The other initial conditions in (4.20) are set as

$$a(0,r) = 1\,, \tag{5.8}$$

$$\beta(0,r) = \sqrt{\frac{2M(0,r)}{r}}\,, \tag{5.9}$$

which corresponds to the dust system. Here, $M(0,r)$ is defined by (4.22) with $j(0,r)=0$ and is calculated numerically as in (5.12).

5.1.2 Time loop

As described in section 3.1, the time dimension is discretised into time steps, t_k, where $k = 1,\ldots,N_t$. In each time step, the procedure in Figure 3.1 is performed. The implementation of these steps are presented in detail in here.

5.1.2.1 Particle weighting

Given the (initial) distribution of the particles, the properties ρ, j, p and p_T need to be calculated at each spatial grid point. From the previous time step (or initialisation), each particle has a position, r_i; momentum, w_i, L_i; and function value $f(t_k, r_i, w_i, L_i)$. The desired quantities can be calculated for each particle by (3.9). To calculate the quantities at each grid point as in (3.11), we use the interpolation function

$$Z_r(r-r_m) = b_1\left(\frac{r-r_m}{\Delta r}\right)\,, \tag{5.10}$$

for the field and particle weighting. This is the hat function, which is defined in (3.7) and illustrated in Figure 3.2. The momentum shape functions are chosen as in standard PIC to $S_p(p^a - p_i^a) = \delta(p^a - p_i^a)$. Furthermore, with the spatial grid volume element $V_m = (4\pi r_m^2\Delta r)$, we calculate ρ, j, p and p_T at the grid points as

in (3.11). In particular,

$$\begin{aligned}
\rho(t_k, r_m) &= \frac{\pi}{4\pi r_m^2 \Delta r} \sum_{i=1}^{N} p_i^0 f(t_k, r_i, w_i, L_i) d\mathring{V}_i Z_r(r_m - r_i(t_k)) \,, \\
j(t_k, r_m) &= \frac{\pi}{4\pi r_m^2 \Delta r} \sum_{i=1}^{N} w_i f(t_k, r_i, w_i, L_i) d\mathring{V}_i Z_r(r_m - r_i(t_k)) \,, \\
p(t_k, r_m) &= \frac{\pi}{4\pi r_m^2 \Delta r} \sum_{i=1}^{N} \frac{w_i^2}{p_i^0} f(t_k, r_i, w_i, L_i) d\mathring{V}_i Z_r(r_m - r_i(t_k)) \,, \\
p_T(t_k, r_m) &= \frac{\pi}{4\pi r_m^2 \Delta r} \sum_{i=1}^{N} \frac{L_i}{2 r_i^2 p_i^0} f(t_k, r_i, w_i, L_i) d\mathring{V}_i Z_r(r_m - r_i(t_k)) \,,
\end{aligned} \tag{5.11}$$

where $p_i^0 = \sqrt{1 + w_i^2 + L_i / r_i^2}$. Note that these correspond to (4.8) with the coordinate transform in (5.1). The Jacobian of the coordinate transform cancels a factor $\frac{1}{r^2}$ in (4.8), which could be troublesome for small r. Furthermore, $\frac{L_i}{r_i^2} = u^2 \sin^2(\alpha)$, so also here the radius is cancelled from the denominator. Note that, due to the chosen Z_r, the equations in (5.11) are implemented by linear interpolation as discussed in section 3.1.1. This is made explicit in the field weighting in section 5.1.2.3.

The mass is calculated at each grid point by discretising (4.22) as

$$M(t_k, r_m) = \sum_{n=1}^{m} 4\pi r_n^2 \Delta r \left[\rho(t_k, r_n) - a(t_k, r_n) \beta(t_k, r_n) j(t_k, r_n) \right] \,, \tag{5.12}$$

5.1.2.2 Field solver

The objective of the field solver is to solve the equations in (4.15-4.18) at the grid points. This, in particular, means updating the function values of a, $\frac{\partial a}{\partial r}$, $\frac{\partial a}{\partial t}$, β and $\frac{\partial \beta}{\partial r}$. First, $\frac{\partial a}{\partial t}$ and $\frac{\partial \beta}{\partial t}$ are updated by (4.18) and (4.17) using the function values from the previous time step. Specifically,

$$\frac{\partial a}{\partial t}(t_k, r_m) = \left[\beta \frac{\partial a}{\partial r} - 4\pi r a^2 j \right]_{(t_{k-1}, r_m)} \,, \tag{5.13}$$

$$\frac{\partial \beta}{\partial t}(t_k, r_m) = \left[\beta \frac{\partial \beta}{\partial r} + \frac{M}{r^2} + 4\pi r p \right]_{(t_{k-1}, r_m)} \,. \tag{5.14}$$

The function values of a and β in the current time step are then given by

$$a(t_k, r_m) = a(t_{k-1}, r_m) + \frac{\partial a}{\partial t}(t_k, r_m) \Delta t \,, \tag{5.15}$$

$$\beta(t_k, r_m) = \beta(t_{k-1}, r_m) + \frac{\partial \beta}{\partial t}(t_k, r_m) \Delta t \,. \tag{5.16}$$

The boundary conditions in (4.2) are enforced as $a(t_k, 0) = 1$ and $\beta(t_k, 0) = 0$. Finally, the spatial derivatives are taken as

$$\frac{\partial a}{\partial r}(t_k, r_m) = \frac{a(t_k, r_{m+1}) - a(t_k, r_m)}{\Delta r} \,, \tag{5.17}$$

$$\frac{\partial \beta}{\partial r}(t_k, r_m) = \frac{\beta(t_k, r_{m+1}) - \beta(t_k, r_m)}{\Delta r} \,, \tag{5.18}$$

for $m = 1, \ldots, N_r - 1$. For $m = N_r$, we simply use the values at r_{N_r-1}. Since the spacetime is asymptotically flat, the difference should be small for large r.

5.1.2.3 Field weighting

Once the metric functions are known at the grid points, they need to be calculated at the particle positions for the particle mover. This is done by (3.13) with the same interpolation function as for the particle weighting, i.e. (5.10). In particular,

$$B(t_k, r_i) = \sum_{m=1}^{N_r} B(t_k, r_m) Z_r(r_m - r_i) \,, \tag{5.19}$$

where B is a placeholder for a, $\frac{\partial a}{\partial r}$, $\frac{\partial a}{\partial t}$, β and $\frac{\partial \beta}{\partial r}$. Note that, as discussed in section 3.1.1, the choice of Z_r in (5.10) enables (5.19) to be implemented by linear interpolation between the closest grid points. Specifically, if $r_i \in [r_m, r_{m+1}]$, we calculate $B(t_k, r_i)$ as

$$B(t_k, r_i) = \frac{r_{m+1} - r_i}{\Delta r} B(t_k, r_m) + \frac{r_i - r_m}{\Delta r} B(t_k, r_{m+1}) \,. \tag{5.20}$$

5.1.2.4 Particle mover

The final step in the time loop is to use the characteristic system of the Vlasov equation to move the particles. In order to avoid problems close to $r = 0$, we define local Cartesian coordinates (x^1, x^2, p_1, p_2) such that x_1 is the radial direction of the particle and x_2 is the direction of the particle's angular momentum. Concretely, for each particle

$$\begin{aligned} x^1(t_k) &:= r_i \,, \;\; p_1(t_k) := w_i \\ x^2(t_k) &:= 0 \,, \;\; p_2(t_k) := \sqrt{L_i}/r_i \end{aligned} \tag{5.21}$$

The Vlasov equation in these coordinates can be written as

$$\frac{\partial f}{\partial t} + \left(\frac{p_\mu}{a p^0} - \beta \frac{x^\mu}{r} \right) \frac{\partial f}{\partial x^\mu} + \left[\left(4\pi r a j + \frac{\partial \beta}{\partial r} - \frac{\beta}{r} \right) \frac{x^\nu p_\nu}{r} \frac{x^\mu}{r} + \frac{\beta}{r} p_\mu \right] \frac{\partial f}{\partial p_\mu} = 0 \,, \tag{5.22}$$

where $\mu, \nu = 1, 2$. From this, the characteristic system is

$$\begin{aligned} \frac{dx^1}{dt} &= \frac{p_1}{a p^0} - \beta \frac{x^1}{r} = \frac{p_1}{a p^0} - \beta \,, \\ \frac{dx^2}{dt} &= \frac{p_2}{a p^0} - \beta \frac{x^2}{r} = \frac{p_2}{a p^0} \,, \\ \frac{dp_1}{dt} &= \left(4\pi r a j + \frac{\partial \beta}{\partial r} - \frac{\beta}{r} \right) \frac{x^\nu p_\nu}{r} \frac{x^1}{r} + \frac{\beta}{r} p_1 = \left(4\pi r a j + \frac{\partial \beta}{\partial r} \right) p_1 \,, \\ \frac{dp_2}{dt} &= \left(4\pi r a j + \frac{\partial \beta}{\partial r} - \frac{\beta}{r} \right) \frac{x^\nu p_\nu}{r} \frac{x^2}{r} + \frac{\beta}{r} p_2 = \frac{\beta}{r} p_2 \,. \end{aligned} \tag{5.23}$$

In the discretised version, the new positions are calculated from the values at the previous time step as

$$\begin{aligned} x^1(t_{k+1}) &= x^1(t_k) + \Delta t \left(\frac{p_1}{ap^0} - \beta \right)_{(t_k, r_i)}, \\ x^2(t_{k+1}) &= x^2(t_k) + \Delta t \left(\frac{p_2}{ap^0} \right)_{(t_k, r_i)}, \\ p_1(t_{k+1}) &= p_1(t_k) + \Delta t \left(4\pi r a j p_1 + \frac{\partial \beta}{\partial r} p_1 \right)_{(t_k, r_i)}, \\ p_2(t_{k+1}) &= p_2(t_k) + \Delta t \left(\frac{\beta}{r} p_2 \right)_{(t_k, r_i)}. \end{aligned} \tag{5.24}$$

Finally, the new particle radius and radial momenta is given by

$$r_i(t_{k+1}) = \sqrt{(x^1)^2 + (x^2)^2}\Big|_{(t_{k+1})}, \tag{5.25}$$

$$w_i(t_{k+1}) = \frac{x^1 p_1 + x^2 p_2}{r_i}\Big|_{(t_{k+1})}. \tag{5.26}$$

Note that L is conserved according to (4.14).

In the particle mover, we also update the particle density function. According to the Vlasov equation, f is conserved along the geodesics. However, since we choose a reference frame of non-canonical momentum coordinates ($p_1 = aw$), the characteristic equations are not volume preserving. In order to calculate the phase space integrals in (4.8) in the next time step, we need to know how phase space integrals of f change over time in these coordinates. By [18, Lemma 2.1], we have

$$\frac{d}{dt} \int_\Omega f(t,z) dz = - \int_\Omega f(t,z) \left(\frac{\partial a}{\partial t} + \frac{\partial a}{\partial r} \frac{dr}{dt} \right) \frac{1}{a} dz, \tag{5.27}$$

where Ω is some region of phase space. With the expression in (4.12) for $\frac{dr}{dt}$, we thus update f in each time step by

$$f(t_{k+1}, r_i, w_i, L_i) = f(t_k, r_i, w_i, L_i) \left[1 - \Delta t \left(\frac{\partial a}{\partial t} + \frac{\partial a}{\partial r} \left(\frac{w_i}{ap^0} - \beta \right) \right) \frac{1}{a} \right]_{(t_k, r_i)}. \tag{5.28}$$

Once the position, momentum and density function for each particle has been updated, the time loop is finished. The new particle distribution is used in the next time step and the cycle is repeated until t_{final} is reached.

5.1.3 Runtime analysis

It is useful to do a quick runtime analysis in order understand how the grid parameters affect the runtime of the simulations. In each time step, the particle weighting, field weighting and particle mover involve every particle, whereas the field solver

only involves every spatial grid point. To handle large numbers of particles, the steps involving every particle are done in N_{threads} parallel computational threads. The runtime thus roughly scales like,

$$\text{Runtime} \propto N_t \left(\frac{N}{N_{\text{threads}}} + N_r \right) = N_t N_r \left(\frac{N_u N_\alpha}{N_{\text{threads}}} + 1 \right) \approx \frac{N_t N_r N_u N_\alpha}{N_{\text{threads}}} \,, \tag{5.29}$$

where the last step follows from $N_u N_\alpha >> 1$. For fixed N_{threads}, the runtime is thus $\propto N_t N_r N_u N_\alpha$. Note that we fix $N_{\text{threads}} = 12$, since this is the available threads in the used hardware.

5.2 Homogeneous initial data

The main objective of the simulations with homogeneous initial data is to show that the Vlasov system can approximate dust arbitrarily well as the initial momentum dispersion $\varepsilon \to 0$. This is done by comparing numerical results from Vlasov simulations to the analytical dust results presented in 4.2.1. We set $\mathring{\rho}$ in (5.4) to

$$\mathring{\rho}(r) = \begin{cases} \mathring{C} & , r < r_{\max} \\ 0 & , \text{else} \end{cases} \,, \tag{5.30}$$

where $\mathring{C}$ is a parameter. By comparison to (4.28), the corresponding dust parameter in section 4.2.1 is then $\gamma = 3\pi\mathring{C}$.

We define two error measures based on the first (in time) point a trapped surface appears. For Vlasov matter, this point is given by the first grid point (t_k, r_m) such that $M(t_k, r_m) > r_m/2$ in accordance to (4.24). Denote this point $(\hat{t}, \hat{r})$. In dust, the first point of the trapped surface is given by the intersection between $t_H(r)$ and $r_b(t)$ in (4.29) and (4.30). Since, t_H depends on r and r_b depends on t, we use the numerical point in the dust functions to define the error. Specifically, we define

$$\begin{aligned} \text{Error } r &:= |\, r_b(\hat{t}\,) - \hat{r}\,| \,, \\ \text{Error } t &:= |\, t_H(\hat{r}) - \hat{t}\,| \,. \end{aligned} \tag{5.31}$$

5.2.1 Parameter search

In order to show that the errors decrease to zero as $\varepsilon \to 0$, we first conduct a parameter search to see how the grid parameters N_r, N_u, N_α and N_t affect the errors for a fixed ε. Since the runtime is proportional to the number of particles, see (5.29), we should make sure that the effort is put where it is most effective. As a centre for the parameter search we use

$$\begin{gathered} N_r = 500,\ N_u = N_\alpha = 60,\ N_t = 20000, \\ r_{\min} = 0.01, r_{\max} = 1,\ t_{\text{final}} = 1.2,\ \mathring{C} = 0.1,\ \varepsilon = 10^{-5} \,, \end{gathered} \tag{5.32}$$

and vary one of the grid parameters at a time. This parameter search is not a complete picture of the multidimensional parameter space, but aims to suggest some heuristics of which parameters to choose in the simulations. Some of the results are presented in Appendix A.1, but we summarise the main takeaways here.

The momentum parameters, N_u and N_α, appear to not affect the result much and it is sufficient to choose $N_u > 30$ and $N_\alpha > 110$ to achieve maximum accuracy. This can be understood since $u_{\max} = \sqrt{\varepsilon} << 1$, so the dispersion in u will anyway be small for small ε. For α, the maximum value is always π so the interval $[0, \pi]$ just needs to be sufficiently discretised in order to initialise particles with enough directional dispersion.

From the set up of the PIC method, it is clear that the most important grid property for minimising numerical errors is the spatial grid size, Δr, which is governed by N_r. It is thus crucial to have a sufficiently large value of N_r. From the parameter search, we find $N_r \geq 1500$ to be sufficient for the current setting.

It may be expected that increasing the number of time steps, N_t, will always give increased accuracy. However, in the parameter search we find that the optimal value of N_t depends on N_r. A too fine time discretisation in a rough spatial discretisation leads to larger errors. There seems to be a positive correlation between the two grids, in the sense that by increasing N_r, an increase N_t in is needed for the best accuracy. If $N_r = 1500$, a good choice of N_t seems to be $N_t \in [10000, 20000]$. If $N_r = 2000$, instead $N_t \in [20000, 40000]$ is a good choice.

5.2.2 Dust convergence

Guided by the parameter search, we choose

$$\begin{aligned} &N_r = 2000,\ N_u = 40,\ N_\alpha = 120,\ N_t = 40000, \\ &r_{\min} = 0.01,\ r_{\max} = 1,\ t_{\text{final}} = 1.2,\ \mathring{C} = 0.1, \end{aligned} \tag{5.33}$$

to show that the Vlasov system can approximate dust arbitrarily well, i.e. that the errors in (5.31) approach zero as $\varepsilon \to 0$. The simulations are performed for a set of logarithmically decreasing ε-values until convergence is reached. Note that if Error $r < \Delta r$ and Error $t < \Delta t$, the best possible numerical values are found and the Vlasov system can approximate dust arbitrarily well up to the available numerical accuracy.

In addition to (5.33), some different parameters are used to show the effect on the error if the grid is not sufficiently fine and if $\mathring{C}$ is altered. Specifically, we consider the same parameters as in (5.33) but with $N_r = 500$ and two different values of N_t. Furthermore, we investigate the case of $\mathring{C} = 0.05$ for a range of different grid parameters to show that the increased error is due to increased numerical errors.

5.3 Inhomogeneous initial data

In this section, we describe how the results with inhomogenous Eardly-Smarr data are produced. We follow the framework presented in section 4.2.2, where the parameter choice $p = 3/2$ is made for simplicity. Note that this value of p is not included in the original paper by Eardly and Smarr (see [4, Table 1]). The first step is thus to find the critical value ζ_{crit} for which $\zeta > \zeta_{\text{crit}}$ gives naked singularities with dust

matter, so that this can be tested with Vlasov matter. To make sure that there is consistency between the PG coordinate system used in this thesis and the comoving coordinates originally used in [4], this is done in both coordinate systems. Moreover, the original results in [4] are reproduced in Appendix C. Once ζ_{crit} is known, we move on to Vlasov matter, for which we first analyse the numerical convergence and then specify the simulation setup for the cosmic censorship results.

5.3.1 Dust matter

The goal of this section is to calculate the outward pointing radial null geodesics of the dust system. In PG coordinates these are given by (4.25) and for dust matter, both a and β are known explicitly. Namely, $a = 1$ and β is given by (4.39). The null geodesics are thus readily obtained by integrating (4.25) with the `ode45` function in MATLAB. The integration is started at $\mathring{r} = 10^{-6}$. Note that the ODE in (4.25) becomes singular at $2M = r$, which can be seen from considering (4.34) in (4.25) with $a = 1$. Hence, a termination criteria is implemented so that the integration is stopped when the curve approaches the apparent horizon defined in (4.43).

To see if the singularity is naked, a null geodesic starting at the singularity, $(\mathring{t}, \mathring{r})$, is plotted together with the apparent horizon. If the null geodesic avoids the apparent horizon in the internal region $0 \leq r \leq r_b(t)$, it will escape to null infinity and the singularity is naked. The apparent horizon, t_H, in (4.43) and the boundary radius, r_b, in (4.38) intersect at $r = 2$, which means that if the null geodesic does not intersect $t_H(r)$ for $r \leq 2$, the singularity is naked.

The critical value ζ_{crit}, for which $\zeta > \zeta_{\text{crit}}$ gives globally naked singularities, is determined by a trial and error numerical search. From [4, Table 1], it is given that if $p = 1$, $\zeta_{\text{crit}} \approx 6.3084$ and if $p = 2$, $\zeta_{\text{crit}} \approx 9.0307$. For $p = 3/2$, we thus expect $\zeta_{\text{crit}} \in [6.3; 9.1]$ and start the search in the centre $\zeta \approx 7.7$. If the singularity is naked, ζ is decreased and if it is not, ζ is increased. By repeating this couple of times, the resulting $\zeta_{\text{crit}} \approx 7.4945$ is found.

To show consistency, the same parameter values are used in comoving coordinates, where instead the comoving geodesic equation (C.6) is integrated. Here, $X(t, \check{r})$ is given by $X(t, \check{r}) = \frac{\partial Y(t,\check{r})}{\partial \check{r}}$ as in (C.2) and $Y(t, \check{r})$ is given by (4.36) as described in section 4.2.2. We see that the same ζ_{crit} holds in comoving coordinates.

For simplicity, we set $\mathring{t} = 0$, and only note that the same results were obtained for other $\mathring{t}$. The results are presented in Appendix A.2.

5.3.2 Vlasov matter

For the results with Vlasov matter, the initial density in (5.4), is set as $\mathring{\rho}(r) = \rho(0, r)$ where ρ is as in (4.42). To make sure that the ADM mass $\mathcal{M} = 1$, as in the dust case, $r_{\max}$ is chosen as $r_{\max} = r_b(0) = c_0(\zeta + \mathring{t})^{\frac{2}{3}}$ in all simulations. In the following, we first discuss some details concerning the ADM mass with Eardly-Smarr data and how to show that the PIC method is numerically sound. We then describe the simulation setup for the results regarding cosmic censorship.

5.3.2.1 ADM mass with Eardy-Smarr data

As discussed in section 4.1.2, the ADM mass $\mathcal{M}$ is a conserved quantity given the conditions in (4.2). However, in Appendix B.2, we show that the Eardly-Smarr data violates the condition of regularity at the centre after the singularity (for $t > \mathring{t}$). To ensure that $\mathcal{M}$ is still conserved with Eardly-Smarr data, we therefore integrate inwards instead of outwards when calculating the mass in the simulations with inhomogenous data. Specifically, we define the mass as

$$\tilde{M}(t,r) = \mathring{\mathcal{M}} - 4\pi \int_r^\infty (\rho - a\beta j)_{(t,s)} s^2 ds \ , \tag{5.34}$$

so that $\tilde{M}(t,\infty) = \mathring{\mathcal{M}} := \mathcal{M}(0)$ for all t. Before the singularity, i.e. for $t < \mathring{t}$, regularity at the centre holds and (5.34) is equivalent to (4.22). The discretised version in (5.12) is modified accordingly to

$$\tilde{M}(t_k, r_m) = \mathring{\mathcal{M}} - \sum_{n=m}^{N_r} 4\pi r_n^2 \Delta r \left[\rho(t_k, r_n) - a(t_k, r_n)\beta(t_k, r_n) j(t_k, r_n)\right] . \tag{5.35}$$

Note that $\mathring{\mathcal{M}}$ is calculated from (5.12) in the initialisation step in order to get consistency between the methods.

5.3.2.2 Numerical convergence

To show that the PIC implementation is numerically sound, we investigate if the ADM error decreases as the grid becomes finer. We define the ADM error as

$$\text{Error}_{\mathcal{M}} = \frac{|\mathring{\mathcal{M}} - M(t_{\text{final}}, \infty)|}{\mathring{\mathcal{M}}} , \tag{5.36}$$

i.e. the relative difference in $\mathcal{M}$ before and after the simulation. Note that this will trivially be 0 if M is calculated from (5.35). We therefore set $t_{\text{final}} < \mathring{t}$, so that $\mathcal{M}$ is always conserved, and calculate M from (5.12) when investigating the ADM error.

Since we use (5.35) to calculate M in the main simulations, we also show that (5.35) is equivalent to (5.12) for $t < \mathring{t}$. For this, we define an error measure based on the L^2 norm over all the grid points normalised by the number of grid points. Specifically, we define the error as

$$\text{Error}_M = \frac{\|\tilde{M} - M\|_2}{N_t N_r} = \frac{1}{N_t N_r} \left(\sum_{k=1}^{N_t} \sum_{m=1}^{N_r} (M(t_k, r_m) - \tilde{M}(t_k, r_m))^2 \right)^{\frac{1}{2}} . \tag{5.37}$$

With the learnings from the parameter search in Appendix A.1 in mind, we choose the parameters

$$\begin{aligned} &N_u = 40,\ N_\alpha = 120,\ p = \frac{3}{2},\ \zeta = 7.6, \\ &t_{\text{final}} = 5.0,\ \mathring{t} = 6.0,\ r_{\min} = 0.01,\ r_{\max} = r_b(0) = c_0(\zeta + \mathring{t})^{\frac{2}{3}} \approx 9.4065, \end{aligned} \tag{5.38}$$

as our baseline and alter the number of temporal and spatial steps N_t and N_r. Remember that the spatial and temporal grids are dependent, so we increase N_r and N_t together in accordance to Appendix A.1. The simulations are performed for different values of ε to see if this has an effect on the numerical errors.

5.3.2.3 Cosmic censorship

To show that cosmic censorship holds for Vlasov matter, we investigate if null geodesics that originate from the singularity are caught by the apparent horizon or not. As discussed above, dust matter gives naked singularities for all $\zeta > \zeta_{\text{crit}}$. We, however, restrict our investigation to two zeta values: $\zeta = 7.6$, which is just above ζ_{crit}, and the larger $\zeta = 15 \approx 2 \cdot \zeta_{\text{crit}}$, to get an idea what happens for a large ζ-value. The results are compared to the same parameter values in dust.

To calculate the null geodesics with Vlasov matter, we first run the PIC simulation in C. The program outputs a and β at each grid point (t_k, χ_m), $k = 0, \dots, N_t$, $m = 0, \dots, N_r$. This data is used with the linear interpolation function `interp2` to solve the null geodesic equation (4.25) with `ode45` in MATLAB. The trapped surface is calculated from the output of M at each grid point as in (4.24).

As discussed in section 2.2.3, deciding when the singularity occurs is not trivial. It is, however, crucial for the cosmic censorship results, since the starting point of the null geodesic is essential to if the geodesic is caught by the trapped surface or not. The origin point of the null geodesics is set to $(t, r) = (\mathring{t}_V, \mathring{r})$, where $\mathring{t}_V$ is the time where the singularity first occurs with Vlasov matter and $\mathring{r}$ is a small initial radius.

Importantly, the singularity time in Vlasov is not the same as in dust, i.e. $\mathring{t}_V \neq \mathring{t}$. To decide $\mathring{t}_V$, we use the Kretschmann scalar, which is calculated from (2.33) for the chosen metric in (4.1). With the EFE in (4.15-4.18), the additional field equation (B.22) and $(1 - A) = \frac{2M}{r}$, it can be simplified to

$$K = \frac{48M^2}{r^6} + 128\pi(p - p_T - \rho)\frac{M}{r^3} - 64\pi(4j^2 - 2(p^2 + \rho^2) - (2p_T - p - \rho)^2)\,. \tag{5.39}$$

Note that the first term is the same as in the Schwarzschild solution. The derivation of K is treated in more detail in Appendix B.3.

As described in section 2.2.3, a singularity can be classified by $K \to \infty$. Numerically, we therefore need a limit K_{lim} such that $K > K_{\text{limit}}$ signifies a singularity. For this, we use the dust case, where K is known analytically. Specifically, we define the limit as

$$K_{\text{limit}} := K_{\text{dust}}(\mathring{t}, \mathring{r})\,, \tag{5.40}$$

where the analytical expressions in (4.41) and (4.42) are used for M and ρ in (5.39). Note that all the other quantities are zero in the dust case, i.e. $j = p = p_T = 0$. The singularity time $\mathring{t}_V$ is then defined as the first t that fulfills

$$K(t, \mathring{r}) > K_{\text{limit}}\,. \tag{5.41}$$

Since the singularity appears at $(\mathring{t}_V, 0)$, we need $\mathring{r}$ to be small. However, due to the numerical implementation, it is not reliable to use the values at the first grid points $r_0, r_1, r_2, \dots$. To mitigate the effect of numerical errors close to $r = 0$, we therefore ignore the first grid points and choose $\mathring{r} = r_8$, i.e. the 8th grid point.

This can essentially be understood as choosing $r_{\min} = r_8$ instead of $r_{\min} = r_0$. The first grid points are included for stability in the simulations, but disregarded in the post-processing. This choice is motivated further in Appendix A.3, but it can be noted that for the dust case, K changes dramatically for small r as t crosses $\mathring{t}$. If, N_r is chosen sufficiently large so that r_8 is small, it should therefore be a stable method to determine $\mathring{t}_V$.

As seen in the parameter search in Appendix A.1, an increase in N_r requires an increase in N_t. From the above, we need to choose N_r large (i.e. Δr small), so N_t also needs to be chosen large so that Δt is sufficiently small. If the grid parameters are unmatched, the program crashes due to numerical instability. Trial and error is used to decide which parameters are possible. Moreover, as can be seen in Table 5.1, $r_{\max}$ and t_{final} need to be relatively large, meaning that very large N_r and N_t are needed to achieve sufficiently small Δr and Δt. The limiting factor of N_t and N_r is the runtime of the simulations, which is approximately proportional to $N_t \cdot N_r \cdot N_u \cdot N_\alpha$ as discussed in section 5.1.3.

To counterbalance the increased runtime, we decrease N_u and N_α from previous simulations. As indicated by the parameter search in Appendix A.1, these do not affect the accuracy much, but have a sizeable effect on the runtime when $N_t \cdot N_r$ is large. For context, the change of N_u from 40 to 30 and N_α from 120 to 90 decreases the runtime with $\approx 44\%$. With the estimated runtimes in Table 5.1 reaching several hours, this makes a significant difference.

The final time, t_{final}, is decided from when the particles have converged to the centre in the dust case (i.e. $r_b(t) = 0$, which occurs at $t = \zeta + \mathring{t}$, see (4.38)). Note that if ε is increased, the dispersion of the particles increases which increases the time for the particles to converge. To capture this, some margin is included in t_{final}. The $r_{\max}$ parameter is, as discussed before, chosen as $r_{\max} = r_b(0) = c_0(\zeta + \mathring{t})^{\frac{2}{3}}$. This means that both $r_{\max}$ and t_{final} need to be increased if ζ or $\mathring{t}$ are increased. To keep Δt and Δr constant, N_r and N_t thus need to be increased. To simulate the system with large ζ-values thus becomes difficult from a runtime point of view.

With this in mind, we choose parameters for all simulations such that

$$p = \frac{3}{2},\ \mathring{t} = 1, r_{\min} = 0.0001,\ \Delta r = 0.00125 \Rightarrow r_8 = \mathring{r} = 0.01,\ \Delta t = 5 \cdot 10^{-5}\,. \quad (5.42)$$

This in particular, leads to the grid parameters presented in Table 5.1 for the two different ζ-values. For context, we also include the estimated runtime which is calculated from previous simulations and the proportionality in (5.29).

Table 5.1: Grid parameters for the cosmic censorship simulations and estimated runtime of the PIC simulation.

ζ	$r_{\max}$	t_{final}	N_r	N_t	N_u	N_α	Est. runtime
7.6	6.9301	10	5544	$2 \cdot 10^5$	30	90	6.3 h
15.0	10.4830	20	8386	$4 \cdot 10^5$	20	60	8.5 h

Note that N_t always denote the time steps in the PIC simulation. To keep the data size manageable for post processing, only every 40th time step is printed.

6

Results & Discussion

The main results of the thesis work are presented and discussed in this section. First, we present results indicating that the Vlasov system can approximate the dust system arbitrarily well up to numerical accuracy. The PIC implementation is then shown to be numerically well-behaved. Finally, it is shown that some instances of naked singularities in the Eardly-Smarr solution disappear by using Vlasov matter with large initial velocity dispersion, and that the numerical precision is not enough to show this for Vlasov matter that is initially arbitrarily close to dust.

6.1 Dust convergence with homogeneous data

To show that the Vlasov system can approximate the dust system arbitrarily well, we first consider simulations with the parameters in (5.33). The results from these simulations are presented in Figure 6.1 and Table 6.1. The general trend is clearly that the errors defined in (5.31) decrease as ε decreases, which suggests that the Vlasov system approaches the dust system. Furthermore, with $\varepsilon \leq 10^{-6}$, the difference is smaller than the numerical accuracy used since Error $r < \Delta r$ and Error $t < \Delta t$. Thus, for these parameters, the Vlasov system can approximate the dust system arbitrarily well up to numerical accuracy.

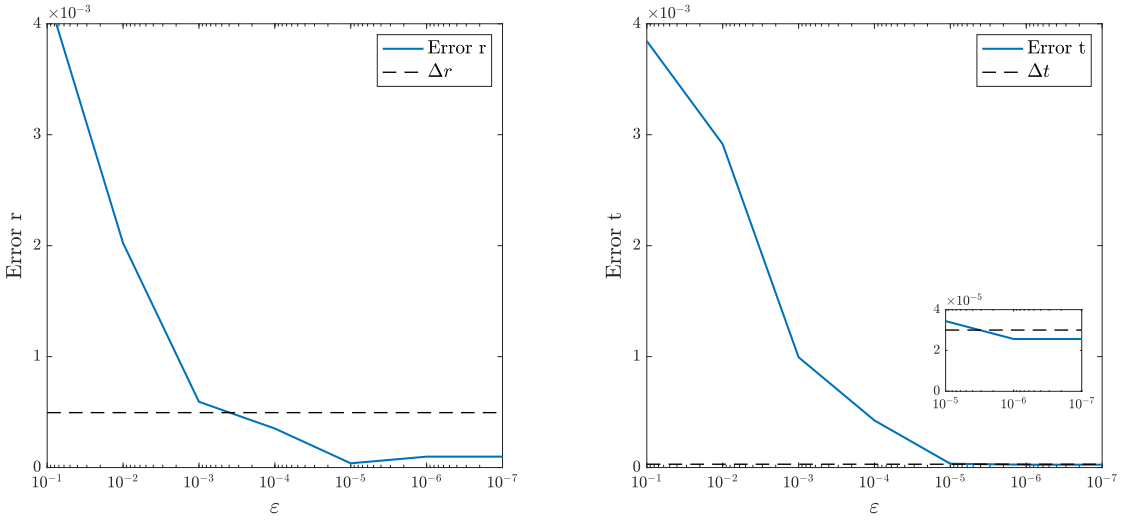

Figure 6.1: Error in r and t as a function of the parameter ε. Generated from parameter values in (5.33).

Table 6.1: Numerical and analytical values from simulations with parameters in (5.33). Asterix (*) denotes error values that are smaller than $\Delta r = 0.000495$ and $\Delta t = 0.000030$ respectively.

ε	$\hat{r}$	$r_b(\hat{t}\,)$	Error r	$\hat{t}$	$t_H(\hat{r})$	Error t
10^{-1}	0.839025	0.834756	0.004269	0.172860	0.169016	0.003844
10^{-2}	0.835065	0.833042	0.002023	0.174570	0.171656	0.002914
10^{-3}	0.836550	0.835957	0.000593	0.171660	0.170666	0.000994
10^{-4}	0.837540	0.837188	0.000352*	0.170430	0.170006	0.000424
10^{-5}	0.837540	0.837578	0.000038*	0.170040	0.170006	0.000034
10^{-6}	0.837540	0.837638	0.000098*	0.169980	0.170006	0.000026*
10^{-7}	0.837540	0.837638	0.000098*	0.169980	0.170006	0.000026*

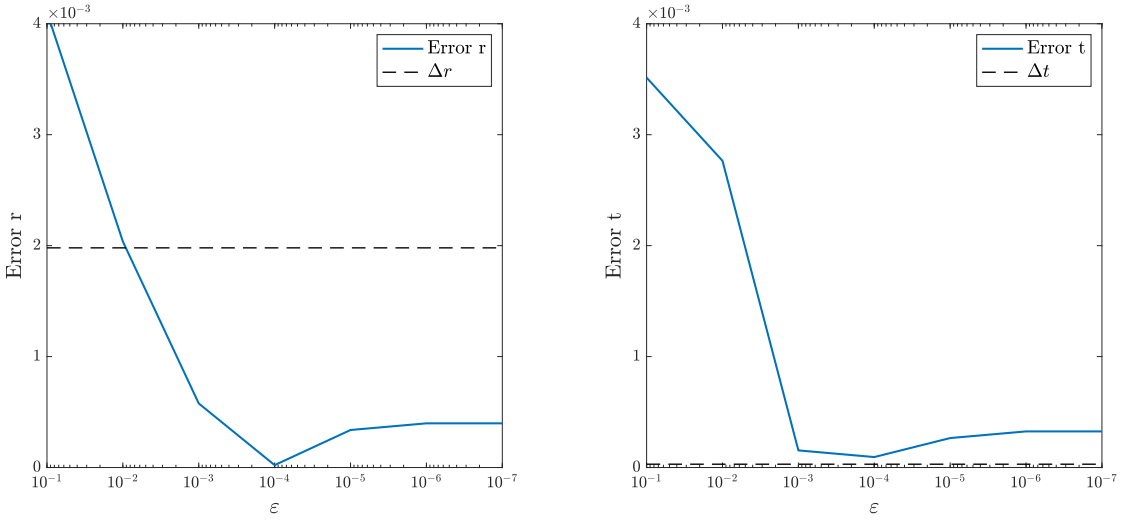

(a) $N_t = 40000$

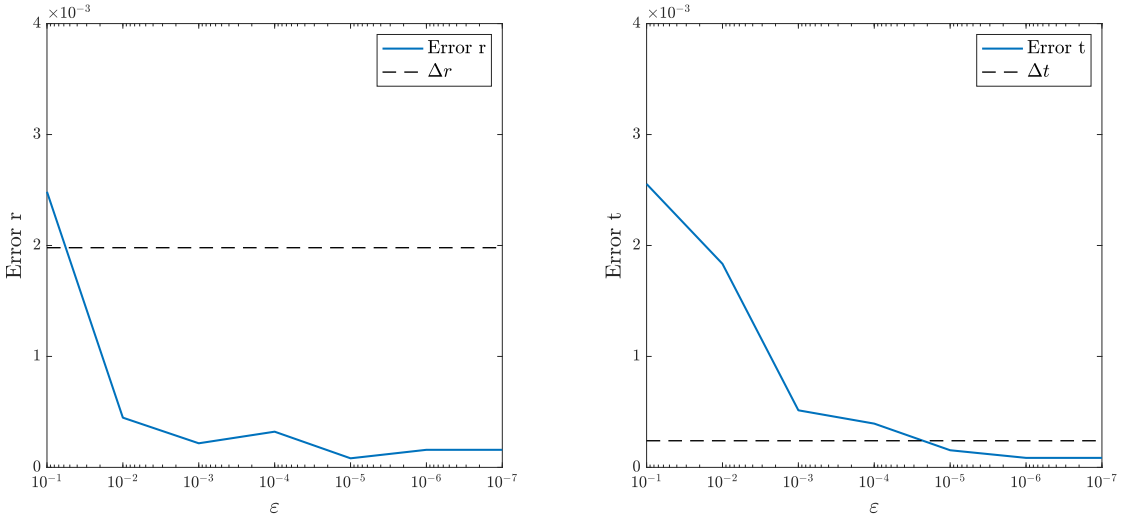

(b) $N_t = 5000$

Figure 6.2: Error in r and t as a function of the parameter ε. Generated from parameter values in (5.33) with $N_r = 500$ and different values of N_t.

A natural question is then if this is achievable for general parameters. In Figure 6.2, the same parameters as in (5.33) are used but with the spatial grid reduced to $N_r = 500$ and with two different number of time steps N_t. In Figure 6.2a the error initially decreases with decreasing ε, but for $\varepsilon \leq 10^{-4}$ it starts to increase. This may seem to contradict the notion that the error should be arbitrarily small for small ε. However, it is merely an effect of a non-synchronized grid. As can be seen in the parameter search in Appendix A.1, the error increases if N_t is too large compared to N_r. In Figure 6.2b, the number of time steps is adjusted for the rougher spatial grid and the error again reaches values smaller than the numerical accuracy. This example highlights the fact that the numerical method is somewhat noisy and that it is important to tune the parameters well for high accuracy.

Both of the previous examples use the initial density $\mathring{C} = 0.1$, which is advantageous in that the trapped surface appears relatively early in the simulation (at $t \approx 0.17$, see Table 6.1). To investigate if the above holds for general initial densities, we also consider $\mathring{C} = 0.05$. With this initial density, the trapped surface appears later in the simulation (at $t \approx 0.75$), which results in overall larger errors. This can be seen in Figure 6.3, where the simulation parameters in (5.33) and $\mathring{C} = 0.05$ are used. Note that the scale of the error axis is ten times larger than in Figure 6.1. The overall trend is the same as before, with decreasing difference as ε decreases, but the errors never reach values below Δr or Δt. Note as well that a smaller ε is needed before convergence is reached, although the difference in error between $\varepsilon = 10^{-7}$ and $\varepsilon = 10^{-9}$ is minimal.

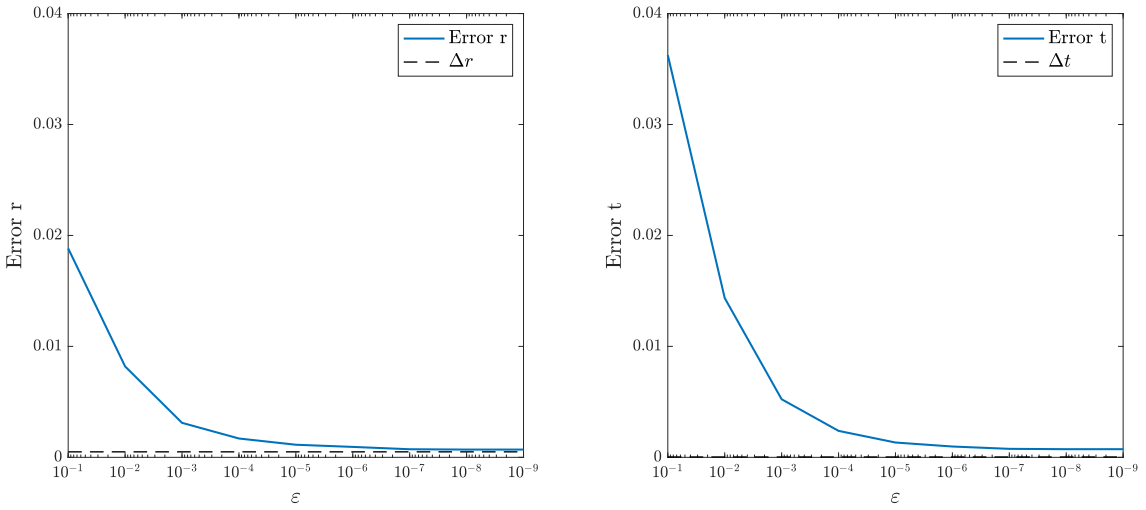

Figure 6.3: Error in r and t as a function of the parameter ε. Generated from parameter values in (5.33) and $\mathring{C} = 0.05$.

To show that the increased error is an effect of increased numerical errors, and not a contradiction of the notion that Vlasov can approximate dust arbitrarily well, we consider the same simulation with different grid sizes (i.e. different accuracies). The different grid parameters are presented in Table 6.2 together with the smallest errors

achieved. The dependence of ε is shown in Figure 6.4, where both the y-axis scale in Figure 6.1 and that in Figure 6.3 are used for comparison.

As can be seen from Figure 6.4a, the errors are more or less the same for the different parameter values as $\varepsilon > 10^{-3}$. The overall trend is also the same as in Figure 6.1 and Figure 6.2b, indicating that the grid discretisation parameters are well synchronized. From Figure 6.4b it is clear that for smaller ε, the error decreases with finer grid. Moreover, from the error values in Table 6.2, it appears as if the error in r is generally of the same magnitude as Δr whereas the error in t is approximately $10\Delta t$. This indicates that this is the best achievable numerical accuracy for $\mathring{C} = 0.05$, which then shows that Vlasov data can approximate dust arbitrarily well up to numerical accuracy also in this case.

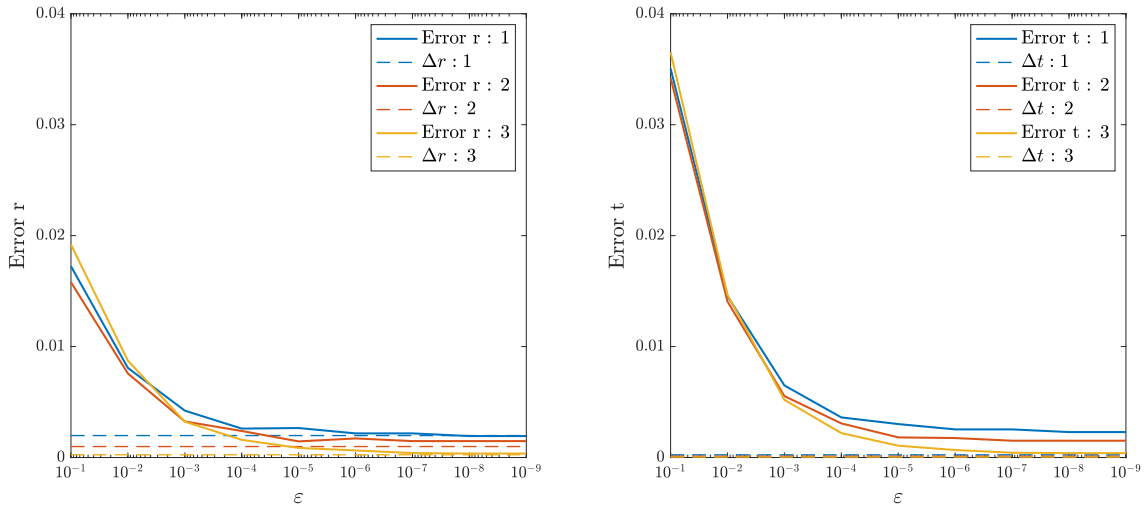

(a) y-axis to scale with Figure 6.3

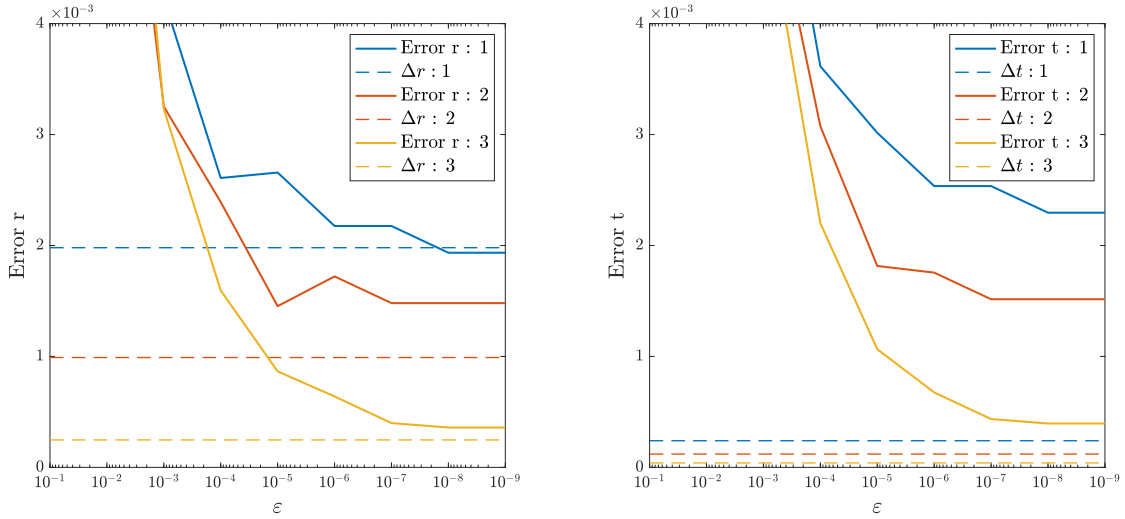

(b) y-axis to scale with Figure 6.1

Figure 6.4: Error in r and t as a function of the parameter ε. The number after : denotes which parameter set in Table 6.2 is used to produce the data.

Table 6.2: Specification of the different grid parameters used in the simulations with $\mathring{C} = 0.05$ together with the smallest achieved errors. The parameters not specified here are those in (5.33).

Parameter set	N_r	Δr	Error r	N_t	Δt	Error t
1	500	0.001980	0.001935	5000	0.000240	0.002295
2	1000	0.000990	0.001481	10000	0.000120	0.001515
3	4000	0.000247	0.000359	30000	0.000040	0.000395
4	8000	0.000124	0.000159	50000	0.000024	0.000195

6.2 Inhomogeneous data

In this section, results obtained with inhomogeneous Eardly-Smarr data are presented. We first show that the numerical method converges well for this data by showing that the numerical errors decrease as expected with increasing number of grid points. We then present and discuss the main results regarding cosmic censorship in Vlasov matter with dust-like initial data.

6.2.1 Numerical convergence

As described in section 5.3.2.1, we verify the numerical convergence by examining the ADM error, $\text{Error}_{\mathcal{M}}$, for different grid sizes. The number of grid points and the resulting errors are presented in Table 6.3. In general, the error is quite small regardless of the grid size. Moreover, it decreases as expected with increased number of grid points. The convergence is further illustrated in Figure 6.5.

Table 6.3: Results of the conservation of mass tests. Parameters not specified here are given in (5.38). The ADM error, $\text{Error}_{\mathcal{M}}$, and Error_M are defined in (5.36) and (5.37). 0* means the error is less than the numerical precision 1e-6.

ε	N_r	N_t	$\mathring{\mathcal{M}}$	$\mathcal{M}(t_{\text{final}})$	$\text{Error}_{\mathcal{M}}$	Error_M
0.1	100	1000	1.016494	1.016876	3.7580e-4	5.9836e-7
0.1	500	5000	1.016502	1.016525	2.2627e-5	7.1922e-9
0.1	1000	10000	1.016502	1.016517	1.4756e-5	2.2098e-9
0.1	2000	20000	1.016502	1.016513	1.0821e-5	7.7222e-10
0.01	100	1000	1.001676	1.002307	6.2994e-4	7.9660e-7
0.01	500	5000	1.001684	1.001696	1.1980e-5	2.8578e-9
0.01	1000	10000	1.001685	1.001688	2.9950e-6	5.3221e-10
0.01	2000	20000	1.001685	1.001687	1.9966e-6	1.5720e-10
0.0001	100	1000	1.000028	0.999998	2.9999e-5	4.1803e-7
0.0001	500	5000	1.000036	1.000043	6.4001e-5	1.6866e-9
0.0001	1000	10000	1.000037	1.000038	9.9996e-7	1.8893e-10
0.0001	2000	20000	1.000037	1.000037	0*	3.3801e-11
1e-6	100	1000	1.000012	0.999981	3.1000e-5	4.2031e-7
1e-6	500	5000	1.000020	1.000025	4.9999e-6	1.3672e-9
1e-6	1000	10000	1.000020	1.000021	9.9998e-7	1.4591e-10
1e-6	2000	20000	1.000020	1.000020	0*	2.7921e-11

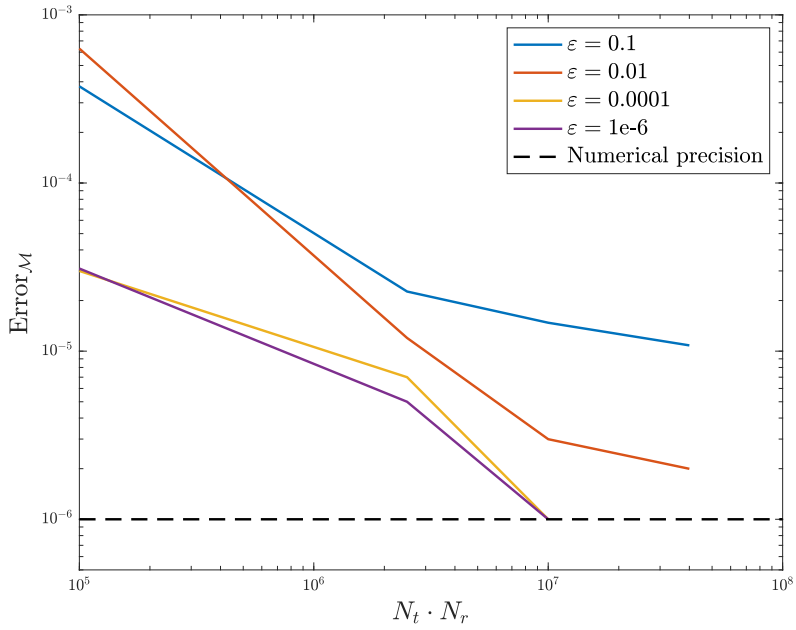

Figure 6.5: The ADM error, $\text{Error}_{\mathcal{M}}$, for different ε as a function of the number of grid points. The parameters used are specified in (5.38) and Table 6.3. Note that the axes are slaced logarihmically.

From Table 6.3 and Figure 6.5, we see that there is a clear trend of decreasing error with decreasing ε. For the smallest ε, the error becomes smaller than the numerical precision when the grid is sufficiently fine. This can be explained by understanding the role of ε. As shown in section 6.1, the Vlasov system approximates the dust system arbitrarily well for small ε. This, in particular, means that all the quantities that are trivial in the dust case will be close to zero throughout the simulation, which leads to decreased numerical errors.

In Table 6.3, we also present the error measure of the difference between calculating the mass as in (5.12) or as in (5.35). It is clear that the difference is negligible for all the tested grid sizes, which verifies the use of (5.35) to overcome the difficulties of non-regularity at the centre which occurs for $t > \mathring{t}$ with the Eardly-Smarr data. Moreover, the error decreases with finer grid size, which indicates the decrease of numerical errors. If there were no numerical errors, (5.12) and (5.35) would be exactly equivalent, which can easily be seen from the equations.

6.2.2 Cosmic censorship

In this section, the central results of this thesis are presented and discussed. We analyse two different values of ζ that give naked singularities in dust and show that these do not give naked singularities in with Vlasov matter, at least for large ε. In Appendix A.2, it is shown that the critical value in dust is $\zeta_{\text{crit}} \approx 7.4595$. If $\zeta < \zeta_{\text{crit}}$ a null geodesic originating at the singularity is caught by the apparent horizon and cosmic censorship holds. If $\zeta > \zeta_{\text{crit}}$, the null geodesic instead escapes to null infinity and cosmic censorship is violated. This is illustrated in Figure A.5.

First, the case of $\zeta = 7.6 > \zeta_{\text{crit}}$ is considered. The results for dust and two instances of Vlasov matter are presented in Figure 6.6. Here, the null geodesic originating at the singularity is plotted together with the apparent horizon and the boundary radius. For the dust case in Figure 6.6a, the null geodesic does not intersect the apparent horizon before it crosses r_b. It instead escapes to null infinity and hence the singularity is naked. For the Vlasov matter in Figure 6.6b and Figure 6.6c, the null geodesic is instead caught by the apparent horizon. By previous results [19], this implies that an event horizon is formed around the singularity. The singularities with Vlasov matter are thus black holes in accordance with the WCCC. Moreover, the null geodesic is caught earlier for $\varepsilon = 0.1$ than for $\epsilon = 0.01$, which implies the singularity becomes "less naked" for Vlasov matter further away from dust.

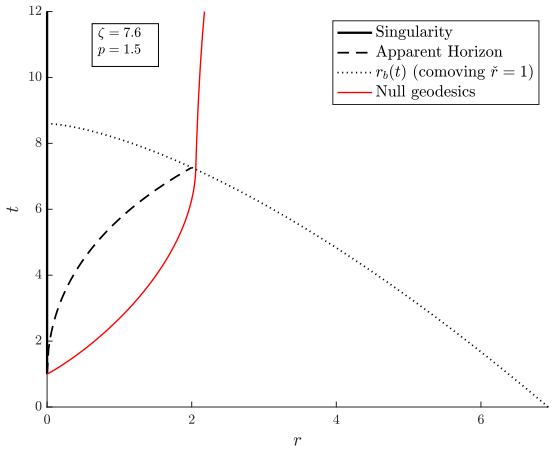

(a) Dust

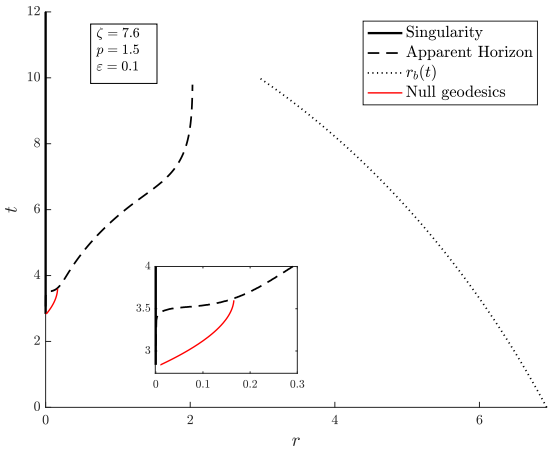

(b) $\varepsilon = 0.1$

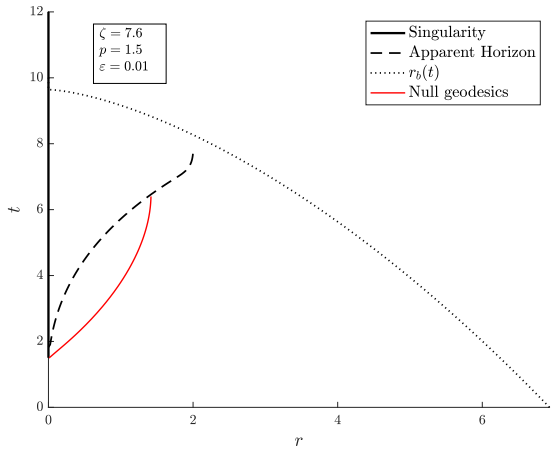

(c) $\varepsilon = 0.01$

Figure 6.6: Null geodesics originating at the singularity in the case of $\zeta = 7.6$ for dust and two instances of Vlasov matter.

To illustrate the difference between Vlasov and dust more clearly, we in Figure 6.7 include the singularity, apparent horizon and boundary radius from dust. These are plotted in gray together with the corresponding quantities from Vlasov in black. Furthermore, we include two null geodesics calculated from the Vlasov data. One originating at the Vlasov singularity $(\mathring{t}_V, \mathring{r})$ as in Figure 6.6 and one originating at the dust singularity $(\mathring{t}, \mathring{r})$. The null geodesics starting from the dust singularity do not cross the apparent horizon for any ε. The key difference between dust and Vlasov in regard to cosmic censorship thus appear to be that the singularity appears later with Vlasov matter. In Figure 6.7, this is illustrated by the vertical lines at $r = 0$, which represent the singularity in dust (gray) and Vlasov (black). More specifically, the key difference is that the apparent horizon spreads out more horizontally for small r with Vlasov matter, which is best seen by the miniboxes in Figure 6.6b and Figure 6.7b.

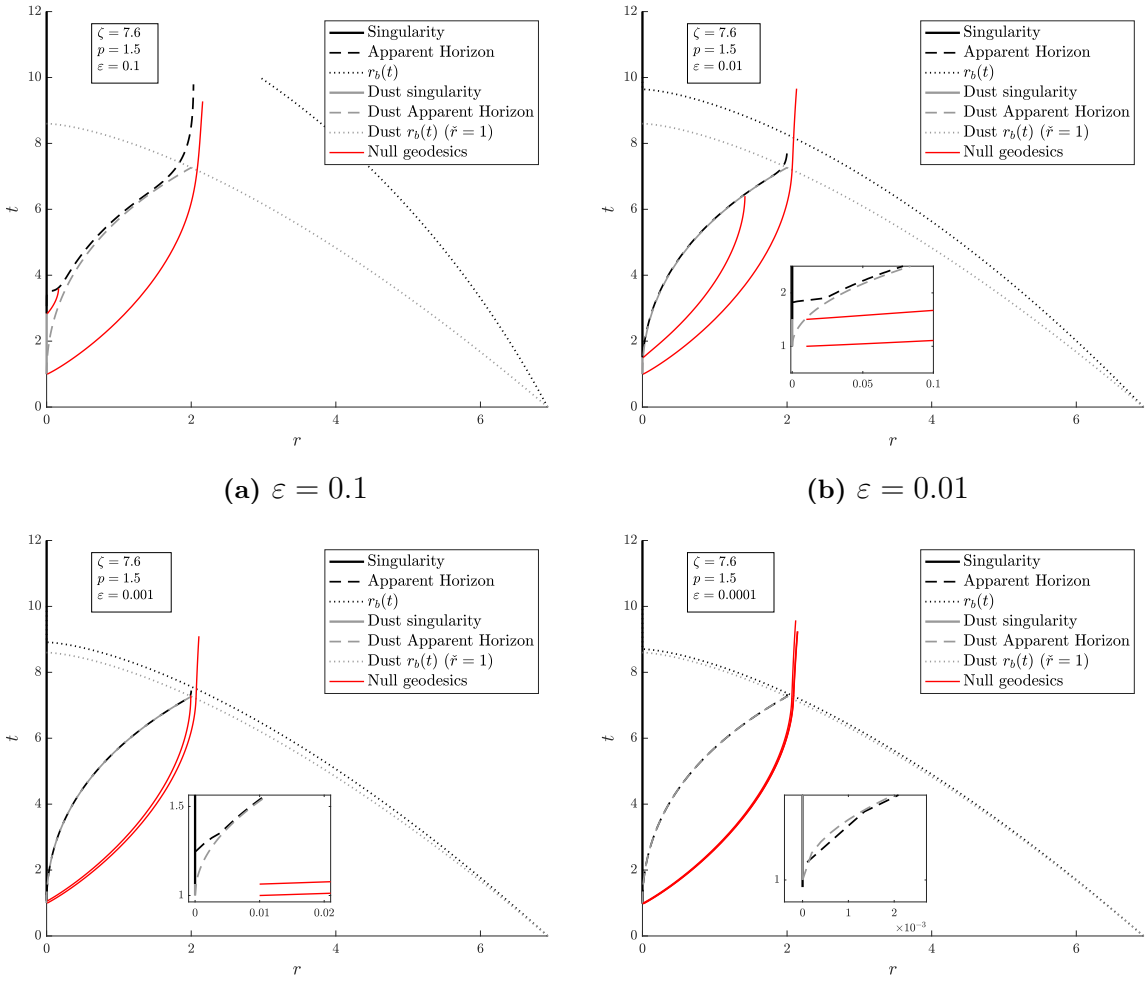

(a) $\varepsilon = 0.1$

(b) $\varepsilon = 0.01$

(c) $\varepsilon = 0.001$

(d) $\varepsilon = 0.0001$

Figure 6.7: Null geodesics originating at the singularity in the case of $\zeta = 7.6$ for different instances of Vlasov matter. Gray lines indicate the corresponding quantities in the dust solution.

It is no surprise that the difference between Vlasov and dust comes into effect close to the singularity in the centre, since this is where the radial and angular momentum, w and L (and thus j, p and p_T), become large. Remember that these quantities are zero in dust. The hypothesis is that even if the matter is arbitrarily close to dust initially, using the Vlasov model instead of dust will make a difference close to the singularity where the momenta increase drastically. From Figure 6.7b, we see that already for $\varepsilon = 0.01$ the precision used in the simulations is barely enough to capture this difference. For the smaller ε, the difference between Vlasov and Dust appear to be for $r < \mathring{r} = 0.01$. It is thus not really captured by the simulations, which only include $r \geq \mathring{r}$ as discussed in section 5.3.2.3.

For $\varepsilon = 0.001$, the Vlasov singularity is nevertheless non-naked due to the slight increase in $\mathring{t}_V$ compared to $\mathring{t}$, although the margin is minimal. For $\varepsilon = 0.0001$, the Vlasov singularity is naked just as in dust. The results for small ε presented here are, however, not really representative since the key effects of Vlasov matter are not captured with the precision used. Figure 6.7c and 6.7d are merely included for completeness and to explain the need of better precision for small ε.

A closer analysis of the difference between $\mathring{t}$ and $\mathring{t}_V$ can be found in Appendix A.3. Specifically in Figure A.8. For the tested $\varepsilon \geq 0.001$, the Vlasov singularity appears after the dust singularity, i.e. $\mathring{t}_V > \mathring{t}$. For $\varepsilon = 0.0001$, it instead appears before the dust singularity, i.e. $\mathring{t}_V < \mathring{t}$. Moreover, the difference between $\mathring{t}_V$ and $\mathring{t}$ decreases with ε, which is in alignment with the results in section 6.1 showing that Vlasov can approximate dust arbitrarily well. Previous analytical arguments in comoving coordinates by H. Andréasson et.al. consider $\epsilon << 1$ and $r << 1$ in an attempt to show that cosmic censorship holds for Vlasov matter. Their results indicate that $\mathring{t}_V < \mathring{t}$, which thus appear to be in alignment with this result. However, in order to verify this argument, very small r need to be considered. This would require better accuracy close to $r = 0$ than what has been achieved in this thesis and is discussed further in section 7.1.

The effect of ε can also be seen in the difference of the boundary radius, r_b, in Vlasov compared to dust. In Figure 6.7, it is clear that the larger the ε, the more r_b will differ from its counterpart in dust. This is due to the dispersion induced by the ε parameter. In dust, all the particles initially have zero relative momenta, which can be understood from the delta function in (4.27). From (5.5), we understand that the approximated delta function used in the Vlasov matter, $H\left(\frac{u^2}{\varepsilon}\right)\frac{1}{\varepsilon\sqrt{\varepsilon}}$, allows some spread in the initial relative momenta. The larger the ε, the larger this initial spread is and thus the larger the dispersion of the particles. This effect is exactly what is seen in the boundary radii in Figure 6.7.

In physical terms, the value of ε governs the largest initial relative momenta of the particles. From (5.5), the maximum initial relative momenta a particle will have is when $u^2/\varepsilon = 1 \implies u = \sqrt{\varepsilon} \implies w_{\max} = \sqrt{\varepsilon}$ by (5.1). In non-geometrised units, this means that the particles with the largest initial momenta will have an initial velocity of $\sqrt{\varepsilon} \cdot c$, where c is the speed of light. The velocity dispersion of galaxies is typically in the order of 100 km/s [20] which is approximately $0.0003c$. For a realistic system, we would thus need $\varepsilon \approx 10^{-7}$. In a realistic system, however,

also factors such as stars of different masses and non-uniform velocity distributions should be considered. This is a topic for a research paper in physics and not within the scope of this thesis. Hence, it will not be discussed further here.

To investigate what happens as ζ increases, we consider the larger $\zeta = 15 \approx 2\,\zeta_{\text{crit}}$. The null geodesics for dust and two instances of Vlasov matter are presented in Figure 6.8. By comparing Figure 6.8a to Figure 6.6a, we see that the dust system becomes "more naked" for the larger ζ value. For $\zeta = 7.6$, the null geodesic narrowly misses the apparent horizon whereas it for $\zeta = 15$ is far from it. For Vlasov matter with $\varepsilon = 0.1$, the result is similar to the previous case. The apparent horizon initially spreads out more horizontally and thereby intersects the null geodesic. The singularity time ($\mathring{t}_V \approx 6$) is significantly later than before ($\mathring{t}_V \approx 3$) compared to dust ($\mathring{t} = 1$). This can be seen by comparing the horizontal black lines at $r = 0$ in Figure 6.8b and Figure 6.6b.

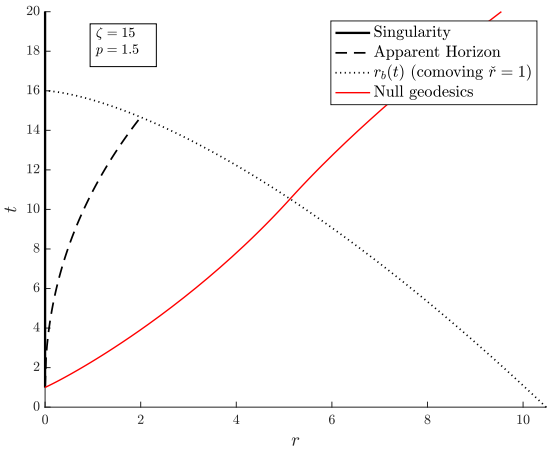

(a) Dust

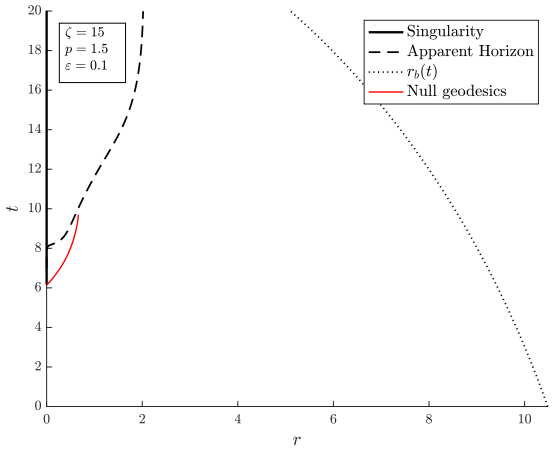

(b) $\varepsilon = 0.1$

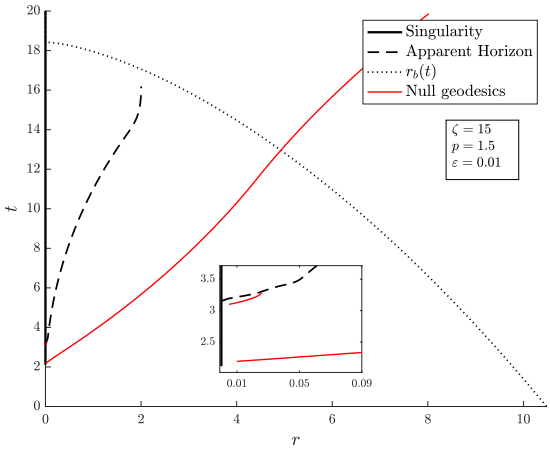

(c) $\varepsilon = 0.01$

Figure 6.8: Null geodesics originating at the singularity in the case of $\zeta = 15$ for dust and two instances of Vlasov matter.

Also for $\varepsilon = 0.01$, the singularity time ($\mathring{t}_V \approx 2.2$) is later than in the $\zeta = 7.6$ case ($\mathring{t}_V \approx 1.5$) and the apparent horizon initially spreads out more horizontally than in dust. However, the singularity time is not close enough to the point where the apparent horizon intersects $r = 0$ and thus the null geodesic diverges to null infinity as in the dust case. In the minibox in Figure 6.8c, we include a null geodesic originating closer to $t_H(r = 0)$ and see that this is indeed caught by the apparent horizon due to the initial horizontal spread of t_H.

We believe that there are two factors as to why the singularity becomes naked for $\varepsilon = 0.01$ in this case. Firstly, similarly to the above case with $\varepsilon \leq 0.001$, due to the numerical precision and not being able to come close enough to $r = 0$. As indicated by the dust solution, it becomes more difficult to get censorship for larger ζ-values and thus the behaviour close to $r = 0$ becomes more important. Secondly, due to the method used to determine $\mathring{t}_V$. Already in the first case, this method is somewhat noisy in that there is not always a clear sudden blow-up of K for Vlasov like there is in dust (see Appendix A.3 for details). In addition, since the difference between dust and Vlasov is most prominent close to the singularity at the centre, it is not obvious that the dust case can be used to define K_{limit}.

Morever, for larger ζ, the blow-up of K becomes more localised at $r = 0$. For example, $K_{\text{limit}} = K_{\text{dust}}(t = \mathring{t}, \mathring{r} = 0.01) = 8488$ if $\zeta = 15$ and $K_{\text{limit}} = K_{\text{dust}}(t = \mathring{t}, \mathring{r} = 0.01) = 33065$ if $\zeta = 7.6$. If $\mathring{r}$ is decreased by a factor 10, these limits increase by a factor 10^3, which would be a more distinguishable K_{limit}. The importance of $\mathring{r}$ to be small in the calculation of $\mathring{t}_V$ thus increases as ζ increases. In section 7.1, we discuss how future studies could potentially improve on the method used for determining $\mathring{t}_V$.

Finally, we include the dust apparent horizon and boundary radius in gray in Figure 6.9. The takeaways are more or less the same as in the case of $\zeta = 7.6$ in Figure 6.7. Specifically, the singularity is formed later for large ε. The apparent horizon also forms later and spreads out more horizontally than in dust for small r.

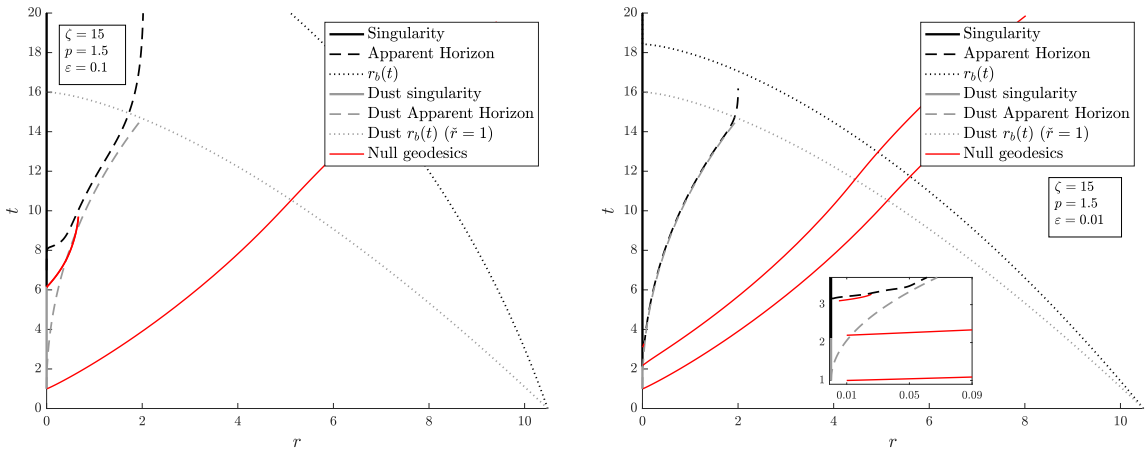

(a) $\varepsilon = 0.1$ **(b)** $\varepsilon = 0.01$

Figure 6.9: Null geodesics originating at the singularity in the case of $\zeta = 15$ in Vlasov matter. Gray lines indicate the corresponding quantities in the dust solution.

7

Conclusions

The concept of cosmic censorship is fundamental to the theory of general relativity and has been debated in the community ever since it was first conjectured. The popularly used dust model is known to generate naked singularities but it is still an open question if they can occur with Vlasov matter. The primary goal of this thesis was to investigate if initial data that is known to give naked singularities in dust also give naked singularities in the Einstein-Vlasov system.

We have shown that the Einstein-Vlasov system can approximate the dust system arbitrarily well up to numerical accuracy. Morever, the cosmic censorship results indicate that naked singularities do not form in the Einstein-Vlasov system, at least for Vlasov matter with a large initial velocity dispersion. This is due to the increased momenta close to the singularity. In order to show this in general and for Vlasov matter that is initially arbitrarily close to dust, better precision close to the centre is needed.

7.1 Further developments

In this section, we discuss how to improve on the results obtained in this thesis.

Due to the limitations discussed in section 5.3.2.3 and 6.2.2, we have not been able achieve a more general cosmic censorship result for the Einstein-Vlasov system. For a conclusive result, it needs to be investigated if naked singularities can form in any Vlasov matter, even one that is initially arbitrarily close to dust. An analysis of the Einstein-Vlasov system with a small initial velocity dispersion is thus needed. As discussed in section 6.2.2, this seems to require analysing the behaviour for very small r which would require significantly better precision than has been achieved here. Since this is a recurring theme, possible efforts to improve the precision for small r are discussed later in this section.

A first step towards a more general result would be to verify a previous analytical argument by H. Andréasson and G. Rein. The argument is based on trapping the inhomogeneous solution between two homogeneous solutions for small r in order to estimate when the inhomogeneous trapped surface and singularity are formed. The argument is carried out in comoving coordinates, so to directly use the method in this thesis, it would first have to be repeated in PG coordinates. Alternatively, the work done in this thesis could be redone in comoving coordinates. This would in

itself be of interest, since the comoving coordinate system is more popularly used in the community. It should be kept in mind that previous analysis by H. Andréasson and G. Rein has shown that local existence does not hold in these coordinates, but it is possible that this is not a problem for numerical studies.

To achieve a more general result, also larger ζ-values need to be investigated. Since the dust case becomes "more naked" for larger ζ, it is interesting to see how the Vlasov matter behaves as ζ increases. The results for $\zeta = 15$ indicate that the singularity will occur later for larger values of ζ and that the apparent horizon will still spread out horizontally for small r, thus intersecting the null geodesic. However, this needs to be verified more generally. As discussed in 5.3.2.3, an increased ζ would require a larger $r_{\max}$ and thus a larger N_r to keep Δr sufficiently small. In short, this would require a larger computational effort.

A parameter that has been left unchanged for the cosmic censorship results is $\mathring{t}$. Since the dispersion of the particles increases with time, increasing $\mathring{t}$ for a fixed ε should be similar to increasing ε for a fixed $\mathring{t}$. This is, however, not something that has been tested extensively in this thesis and it could be of interest to see how a change in $\mathring{t}$ affects the results. An increase in $\mathring{t}$ does, however, necessitate an increase in t_{final} and thus an increase in N_t to keep Δt constant.

A key improvement needed to conduct the suggested studies is to improve on the method used to determine $\mathring{t}_V$. The method in this thesis is based on the Kretschmann scalar and the K_{limit} calculated from dust. As discussed in section 6.2.2 and Appendix A.3, this method is quite noisy. Part of this comes from the unstable numerical behaviour at the centre. For example, β and $\frac{\partial \beta}{\partial r}$ are both set to 0 at r_0 in the PIC simulation for numerical stability. As can be seen from the dust case, β is not 0 for $t > \mathring{t}$. This inconsistency arises from trying to simulate for times after the singularity. Moreover, this affects the first couple of grid points since $\frac{\partial \beta}{\partial t}$, which updates β, depends on both β and $\frac{\partial \beta}{\partial r}$. Already in this work, alternative implementations were tried but without success. To obtain a better precision for small r an improvement of this implementation could be crucial.

An alternative approach of determining $\mathring{t}_V$ could come from analytical arguments. In dust, it is known that the apparent horizon intersects $r = 0$ at $\mathring{t}$, i.e. $t_H(r = 0) = \mathring{t}$. A similar result for Vlasov matter would simplify the numerical analysis and give more confidence in the results. See Figure 6.8c for an example of where this would completely change the cosmic censorship result. An indication to why this might be true also for Vlasov is that the metric does not appear to be singular before $t_H(r = 0)$, but this would need to be verified.

Finally, we discuss possible ways to improve the numerical precision for small r. As can be seen by (5.29), the runtime depends heavily on the grid parameters N_t and N_r. To improve the precision, both of these need to be increased which increases the runtime drastically. One way of mitigating the increased runtime is by increasing the computational power. By running the simulations on a computer cluster the number of parallel processes, N_{threads}, could be increased drastically. If necessary, also the field solver could be done in parallel. Using a computer cluster would both help in the analysis and decrease the feedback time for test simulations.

Although the brute force approach of just increasing the computer power might work, there are alternatives. Note that a combination of the two would probably be the best approach. One alternative could be to use a non-uniform spatial grid, with more grid points close to the centre and fewer further out. This is used in other discretisation schemes where the computational effort is focused on the areas of most interest.

Another idea could be to not initialise as many particles per spatial grid point, in order to keep the total number of particles low even when N_r increases. In the current implementation, this can be done by decreasing N_u and N_α, as done in Table 5.1. There is, however, a limit on how much N_u and N_α can be decreased since these need to be large enough to ensure a sufficiently smooth dispersion of the initial momenta. An alternative implementation could be to not initialise particles at every spatial grid point. Another alternative to get a sufficiently smooth dispersion in the initial momenta without introducing as many particles per grid point, could be to initialise fewer particles at each grid point, and sample their initial momenta from the momentum distribution. By then increasing the number of grid points, the total momenta dispersion among all particles will be the same but Δr will be smaller.

Bibliography

[1] Wald RM. General Relativity. Chicago: The University of Chicago Press; 1984.

[2] Oppenheimer JR, Snyder H. On Continued Gravitational Contraction. Physical Review. 1939 9;56(5):455-9.

[3] Penrose R. Gravitational collapse: The role of general relativity. Rivista del Nuovo Cimento. 1969;1:252-76.

[4] Eardley DM, Smarr L. Time functions in numerical relativity: Marginally bound dust collapse. Physical Review D. 1979 4;19(8):2239-59.

[5] Christodoulou D. Violation of cosmic censorship in the gravitational collapse of a dust cloud. Communications in Mathematical Physics. 1984 6;93(2):171-95.

[6] Andréasson H. Two topics for the Einstein-Vlasov system: Gravitational collapse and properties of static and stationary solutions. General Relativity Minicourse, Harvard CMSA; 2022. Available from: `https://youtu.be/WhwBxDxgj6s?si=p9kQK5v5hLunNnau`.

[7] Rendall AD. An introduction to the Einstein-Vlasov system. Max Planck Institute for Gravitational Physics; 1996. Available from: `arXiv:gr-qc/9604001`.

[8] Andréasson H. The Einstein-Vlasov System/Kinetic Theory. Living Reviews in Relativity. 2011 12;14(1):4.

[9] Andréasson H, Rein G. The Einstein-Vlasov system in Painlevé-Gullstrand coordinates. In preparation;.

[10] Kehle C, Unger R. Extremal black hole formation as a critical phenomenon. ETH Zürich & Princeton University; 2024. Available from: `arXiv:2402.10190`.

[11] Altas E, Tekin B. Basics of Apparent horizons in black hole physics. Journal of Physics: Conference Series. 2022 2;2191(1):012002.

[12] Wald RM. "Weak" Cosmic Censorship. PSA: Proceedings of the Biennial Meeting of the Philosophy of Science Association. 1992;1992:181-90. Available from: `http://www.jstor.org/stable/192834`.

[13] Hirvonen V. The Ricci Tensor: A Complete Guide With Examples;. Available from: `https://profoundphysics.com/the-ricci-tensor/`.

[14] Tskhakaya D. The Particle-in-Cell Method. In: Fehske H, Schneider R, Weiße A, editors. Computational Many-Particle Physics. Berlin, Heidelberg: Springer Berlin Heidelberg; 2008. p. 161-89. Available from: https://doi.org/10.1007/978-3-540-74686-7_6.

[15] Pritchett PL. Particle-in-Cell Simulation of Plasmas— A Tutorial. In: Büchner J, Scholer M, Dum CT, editors. Space Plasma Simulation. Berlin, Heidelberg: Springer Berlin Heidelberg; 2003. p. 1-24. Available from: https://doi.org/10.1007/3-540-36530-3_1.

[16] Lapenta G. Kinetic Plasma Simulation: Particle In Cell Method. In: Proceedings of the XII Carolus Magnus Summer School on Plasma and Fusion Energy Physics. KU Leuven; 2015. .

[17] Hu Y. Particle In Cell (PIC) simulation. Hefei: Institute of Physical Sciences, Chinese Academy of Sciences; 2019.

[18] Rein G, Rodewis T. Convergence of a Particle-in-cell Scheme for the Spherically Symmetric Vlasov-Einstein System. Indiana University Mathematics Journal. 2003;52(4):821-61. Available from: http://www.jstor.org/stable/24903484.

[19] Dafermos M. Spherically symmetric spacetimes with a trapped surface. Classical and Quantum Gravity. 2005 6;22(11):2221-32.

[20] Hu J. The black hole mass–stellar velocity dispersion correlation: bulges versus pseudo-bulges. Monthly Notices of the Royal Astronomical Society. 2008 6;386(4):2242-52.

[21] Rein G. The Vlasov-Einstein system with surface symmetry. Habilitation: Mathematisches Institut der Ludwig-Maximilians-Universität München; 1995.

A

Additional figures

In this appendix, we present some additional figures that are not relevant to the main results, but may be relevant for the discussion or methodology.

A.1 Grid parameter search

Here, some figures produced during the parameter search discussed in section 5.2 are presented. In all figures, the error in r is given to the left and the error in t to the right. The errors are defined as in (5.31) and the parameters not specified are as in (5.32). The values of Δt and Δr are included in order to see how the error relates to the maximum achievable precision.

In Figure A.1, we see that the error is not affected much by changing N_u as long as N_u is sufficiently large. The same is true for N_α, but with a larger threshold value, as can be seen in Figure A.2.

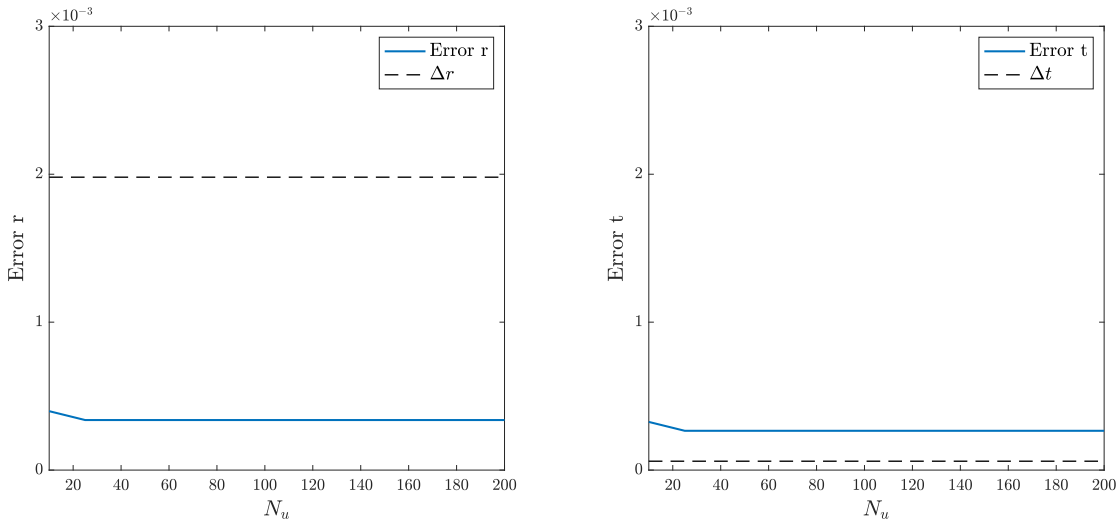

Figure A.1: Error in r and t as a function of the number of grid steps in u.

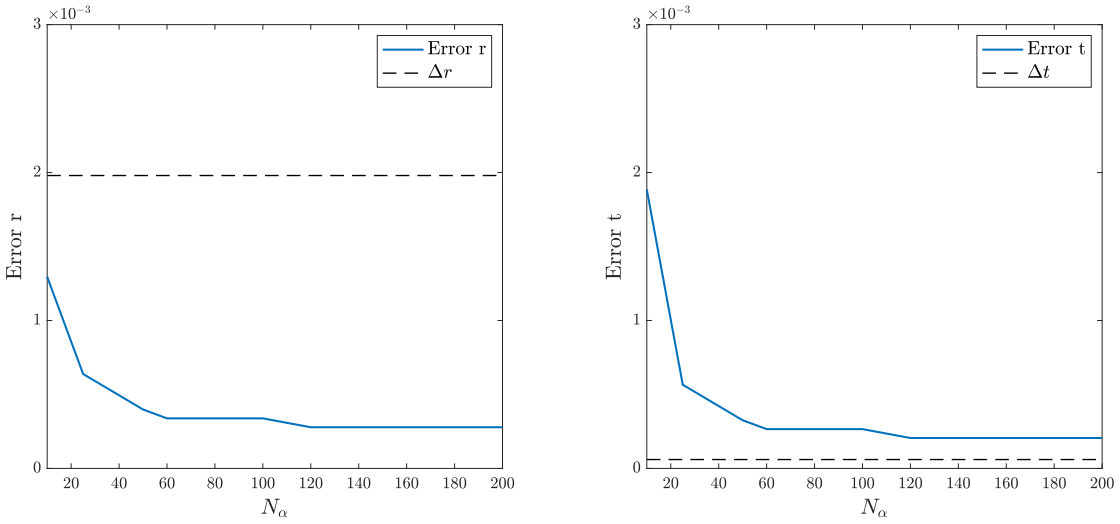

Figure A.2: Error in r and t as a function of the number of grid steps in α.

The spatial grid size governed by N_r, has a greater effect on the error, which can be seen in Figure A.3. This is expected, since N_r is the main parameter for reducing numerical errors. Moreover, the numerical value of r is used in the error measure of t, meaning that sufficient accuracy in r is needed for a good Error t. With sufficiently large N_r, the best possible accuracy for the given time discretisation is achieved, i.e. Error $t < \Delta t$.

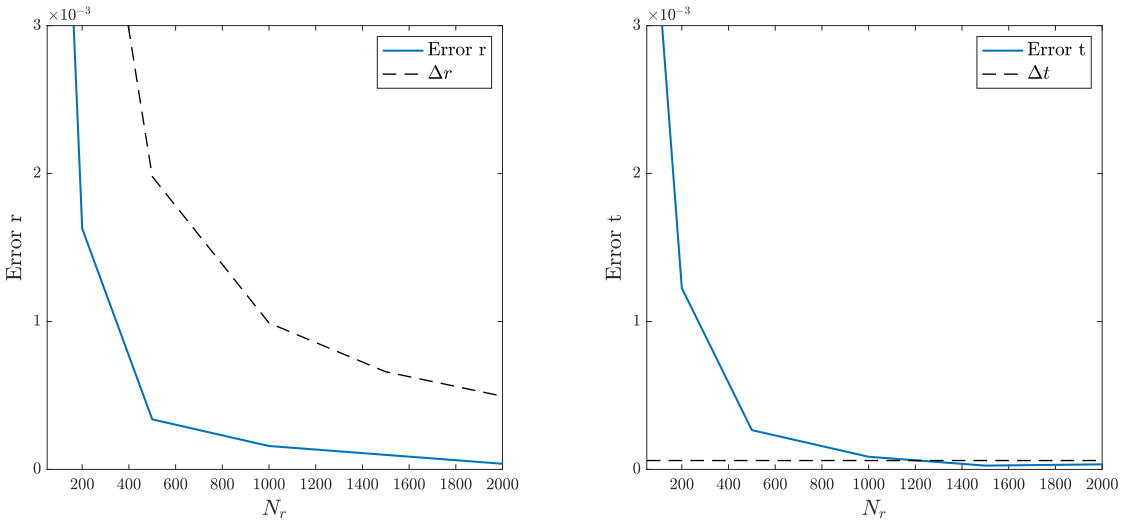

Figure A.3: Error in r and t as a function of the number of grid steps in r.

The number of time steps, N_t, also affects the numerical accuracy. However, increasing N_t does not necessarily lead to better accuracy unless the number of spatial grid steps, N_r, is sufficiently large. This is seen in Figure A.4, where the errors increas if N_t is chosen too large for a given N_r. Nevertheless, as N_r increases, N_t needs to be increased sufficiently to achieve the best accuracy.

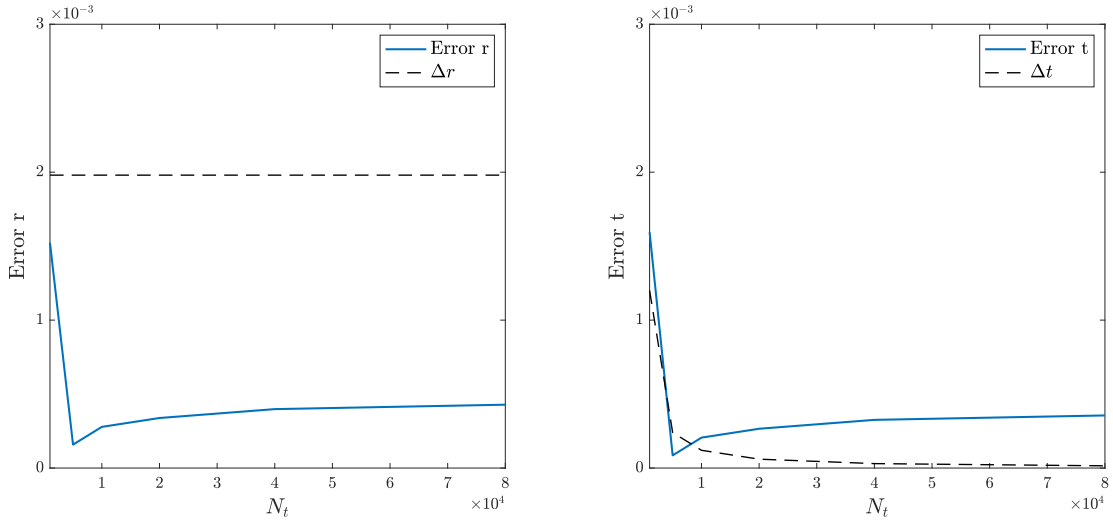

(a) $N_r = 500$

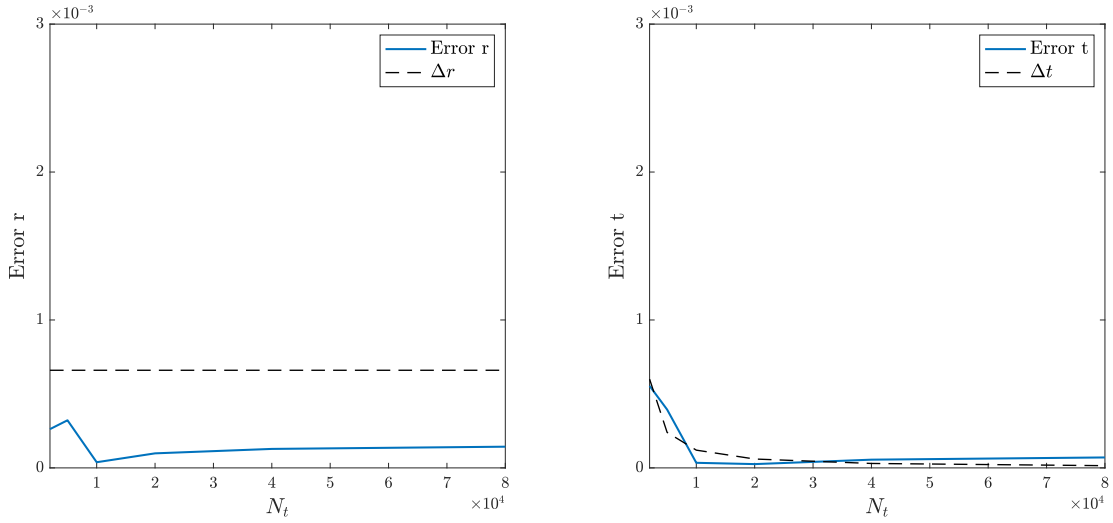

(b) $N_r = 1500$

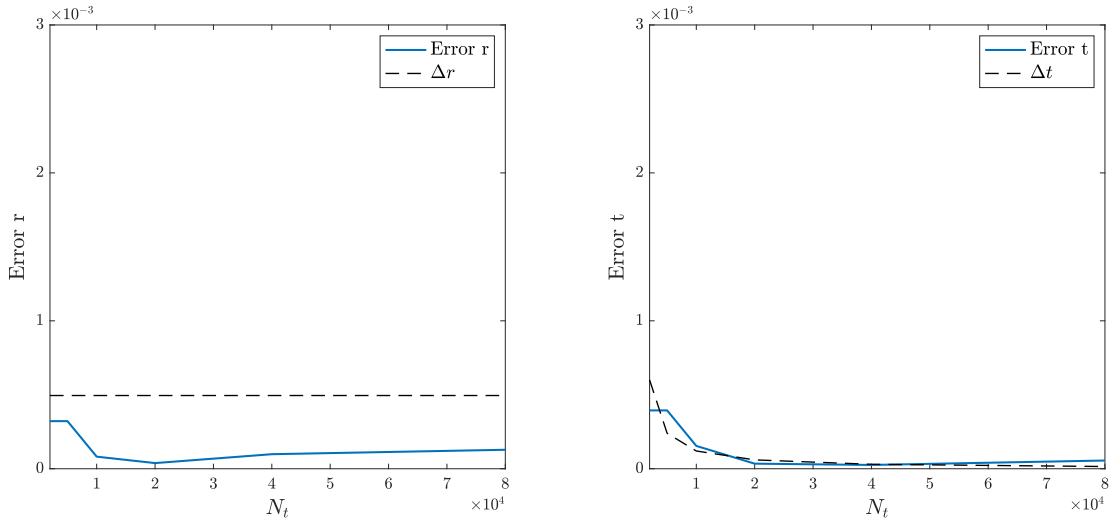

(c) $N_r = 2000$

Figure A.4: Error in r and t as a function of the number of grid steps in t, for varying number of spatial grid steps, N_r.

A.2 Critical zeta value for $p = 3/2$

To find the critical zeta value when $p = 3/2$, we perform a numerical search described in section 5.3.1. The resulting value is $\zeta_{\text{crit}} \approx 7.4945$. This is illustrated for PG coordinates in Figure A.5 and for comoving coordinates in Figure A.6. If $\zeta > \zeta_{\text{crit}}$, a null geodesic originating at the singularity, $(0, 0)$, is not caught by the apparent horizon and can thus escape to null infinity. If $\zeta < \zeta_{\text{crit}}$, the null geodesic intersects the apparent horizon which, by previous results [19], imply that an event horizon will form around the singularity. Note that, we here set $\mathring{t} = 0$, but the same ζ_{crit} is found for other values of $\mathring{t}$ as well.

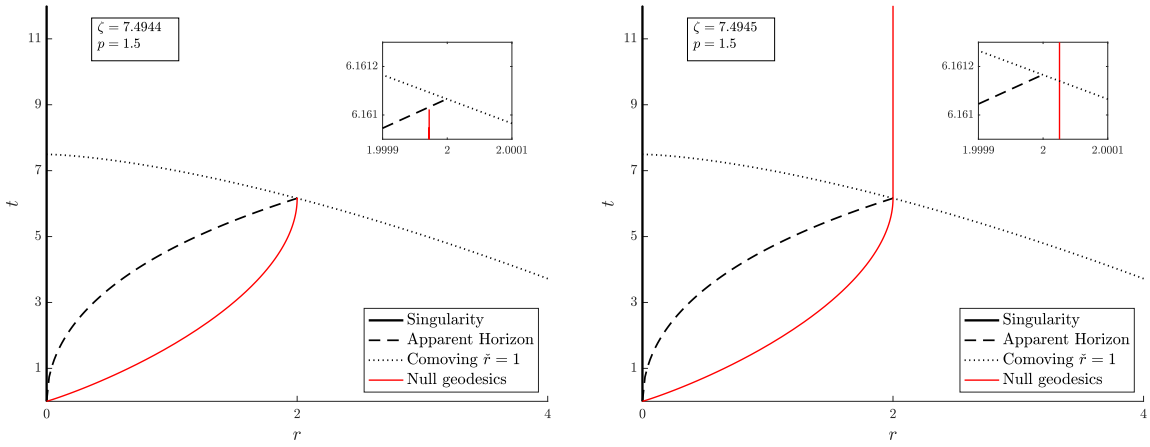

(a) $\zeta < \zeta_{\text{crit}}$ **(b)** $\zeta > \zeta_{\text{crit}}$

Figure A.5: Null geodesic originating at $(0, 0)$ for $\zeta \gtrless \zeta_{\text{crit}}$ in PG coordinates.

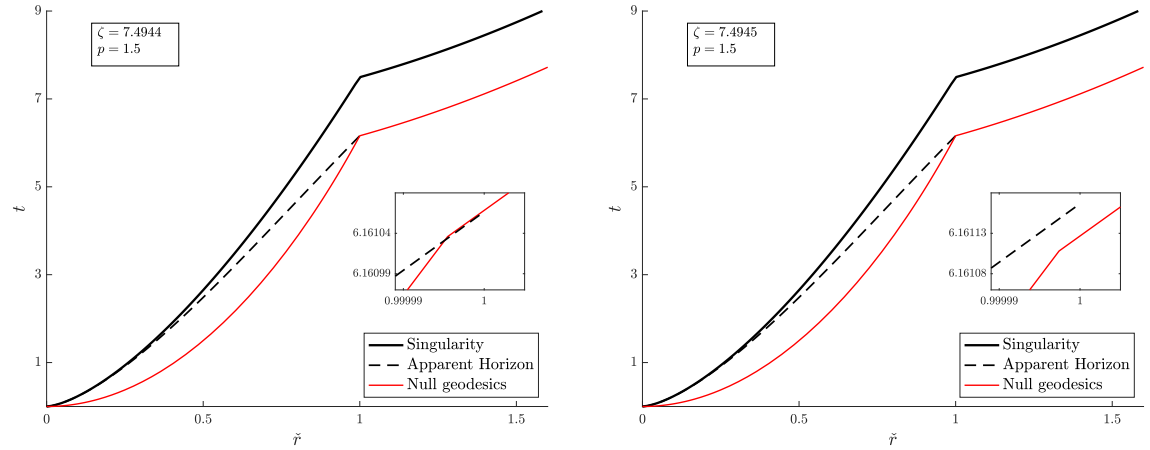

(a) $\zeta < \zeta_{\text{crit}}$ **(b)** $\zeta > \zeta_{\text{crit}}$

Figure A.6: Null geodesic originating at $(0, 0)$ for $\zeta \gtrless \zeta_{\text{crit}}$ in co-moving coordinates.

A.3 Kretschmann implementation

Here, the behaviour of the Kretschmann scalar, K, and specfically the suitability of equation (5.40) as a measure of when the singularity occurs, is analysed. The purpose is to motivate the method defined in section 5.3.2.3. From section 2.2.3, we know that $K \to \infty$ at a singularity. We use the case of $\mathring{t} = 1$ and $\zeta = 7.6$ to analyse how K behaves close to $\mathring{t}$ and $\mathring{t}_V$.

We first consider the dust case, where K is known analytically by (4.41) and (4.42) in (5.39). To illustrate how K_{limit} depends on $\mathring{r}$, $K(t, \mathring{r})$ is plotted as a function of t for different values of $\mathring{r}$ in Figure A.7. For all $\mathring{r}$, $K(t, \mathring{r})$ goes from negative to large positive values just before t crosses $\mathring{t}$. The smaller the $\mathring{r}$, the closer this shift is to $t = \mathring{t}$. Moreover, the values taken at $t = \mathring{t}$ (i.e. K_{limit}) appear to increase exponentially as $\mathring{r}$ decreases. This can be seen from Figure A.7b, where a logarithmic scale is used and the K_{limit} for each $\mathring{r}$ is depicted. This sudden shift thus looks promising as an indicator for singularity.

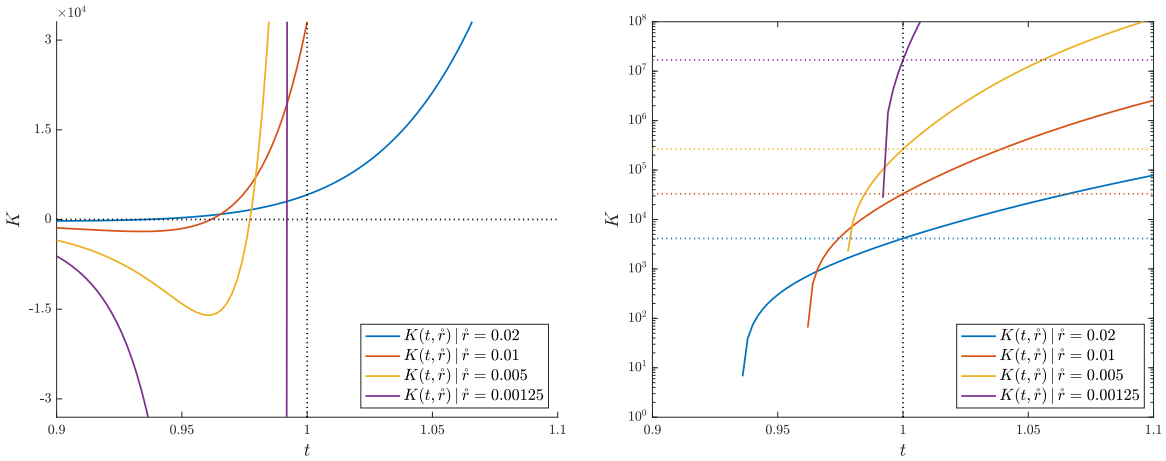

(a) Linear scale

(b) Logarithmic scale

Figure A.7: The Kretschmann scalar $K(t, \mathring{r})$ in dust plotted for different choices of $\mathring{r}$. To the left, linear scale is used on the y-axis and to the right a logarithmic scale is used. The vertical black dotted line represents the dust singularity time $\mathring{t}$ and the horizontal coloured dotted lines represent the values of K_{limit} in (5.40) corresponding to each $\mathring{r}$.

In Vlasov matter, the issue becomes more intricate. We use the simulation data from the results in section 6.2.2, i.e. the simulation parameters in (5.42) and Table 5.1. Let $r_{\check{m}}$ denote the specific grid point chosen as $\mathring{r}$, i.e. $\mathring{r} = r_{\check{m}}$. The idea of (5.40) and (5.41) is that as long as $\mathring{r}$ is chosen small enough, the result should be relatively independent of exactly which grid point is chosen. To avoid some numerical instability at the centre, which propagates to the first couple of grid points, the grid index $\check{m}$ needs to be chosen sufficiently large. As discussed in section 5.3.2.3, the choice of $\check{m}$ becomes a trade-off between runtime and accuracy as increasing $\check{m}$ means that N_r needs to be increased for $\mathring{r}$ to still be sufficiently small.

In Figure A.8, we illustrate this for Vlasov matter with different ε and the grid index $\check{m} \in \{1, 4, 8, 16\}$. The vertical dotted lines represent the singularity time $\mathring{t}_V$ from each choice of $\check{m}$ as determined by (5.40) and (5.41). Ideally, these lines would be close together, to verify the above. We see that this is generally the case and that for $\varepsilon \geq 0.01$, $\mathring{t}_V$ is far from $\mathring{t}$ for all $\check{m}$. With $\check{m} = 1$, $K(t, \mathring{r})$ appears to behave somewhat irregular, which is a sign of the numerical instability close to the centre. Moreover, for $\varepsilon \geq 0.01$, $K(t, r_1)$ appears to shift from small (or negative) values to large positive values quite long before reaching K_{limit}. It does therefore not give the same clear break in trend close to $\mathring{t}_V$ as in the dust case or for the larger $\check{m}$.

For the smaller ε values, the different choices of $\check{m}$ still give $\mathring{t}_V$ values that are close to each other, but also closer to $\mathring{t}$. The relative distance to $\mathring{t}$, is significantly different for different choices of $\check{m}$. This indicates that better precision is needed for an accurate analysis in these cases and is why they are not considered in this work.

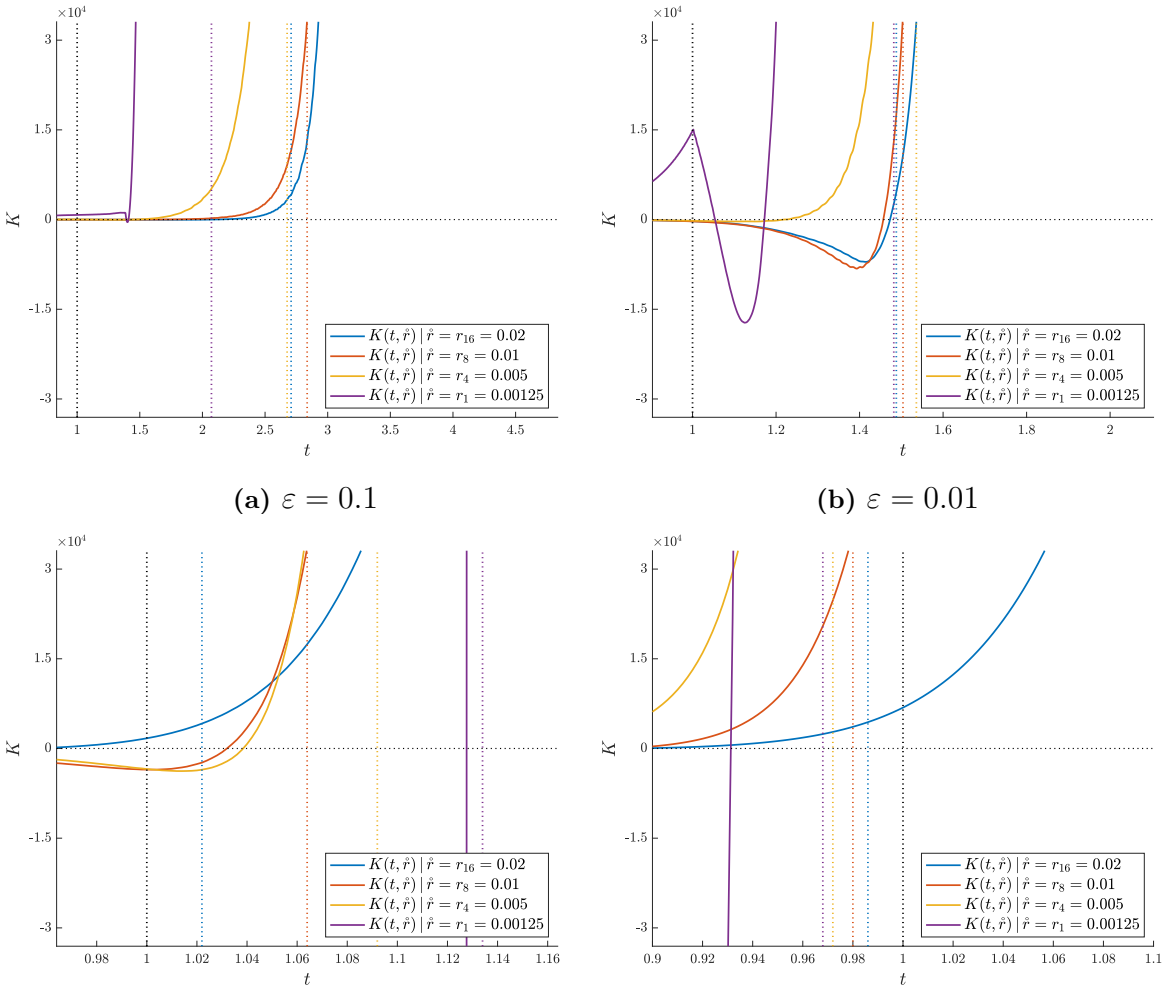

(a) $\varepsilon = 0.1$ **(b)** $\varepsilon = 0.01$

(c) $\varepsilon = 0.001$ **(d)** $\varepsilon = 0.0001$

Figure A.8: The Kretschmann scalar $K(t, \mathring{r})$ in Vlasov matter, plotted for different choices of $r_{\check{m}} = \mathring{r}$. Vertical dotted lines show the corresponding $\mathring{t}_V$ determined from (5.40-5.41). The vertical black dotted line represents the dust singularity time $\mathring{t}$.

B

Additional derivations

In this appendix, derivations that are too lengthy for the main text are presented. Specifically, this consists of the coordinate change in the derivation of T_{00} in the Einstein-Vlasov system, a formal calculation of the conservation of mass and the derivation of the Kretschmann scalar.

B.1 Coordinate transform in the macroscopic quantity integrals

Here, the coordinate transformation $(p_1, p_2, p_3) \mapsto (w, L, p_3)$ and how it is used in (4.10) is presented. We follow the proof in [21, Lemma 8.3].

Let $(w, L, p_3) \mapsto (p_1, p_2, p_3)$ be described by

$$\begin{aligned} w &= \frac{1}{a} p_1 \,, \\ L &= {p_2}^2 + \frac{1}{\sin^2(\theta)} {p_3}^2 \,, \\ p_3 &= p_3 \,. \end{aligned} \tag{B.1}$$

The determinant of the Jacobian of this transformation is then

$$2\frac{1}{a} p_2 = 2\frac{1}{a}\sqrt{L - \frac{1}{\sin^2(\theta)} {p_3}^2} \tag{B.2}$$

and thus the Jacobian of the inverse transformation $(p_1, p_2, p_3) \mapsto (w, L, p_3)$ is

$$\frac{a}{2\sqrt{L - \frac{1}{\sin^2(\theta)} {p_3}^2}} \,. \tag{B.3}$$

Wuth this transformation in (4.10), the T_{00} integral becomes

$$\begin{aligned}
T_{00} &= \frac{1}{r^2 a\sin(\theta)}\int_{\mathbb{R}^3} f(t,x,p)\left(p^0 - 2\beta p_1 + \beta^2 (p_1)^2\frac{1}{p^0}\right)dp_1dp_2dp_3 \\
&= \frac{1}{r^2 a\sin(\theta)}\int_{\mathbb{R}^3} f(t,r,w,L)\underbrace{\left(p^0 - 2a\beta w + a^2\beta^2 w^2\frac{1}{p^0}\right)}_{=:\kappa(w,L)}\frac{a}{2\sqrt{L-\frac{1}{\sin^2(\theta)}{p_3}^2}}dLdwdp_3 \\
&= \frac{1}{2r^2\sin(\theta)}\int_{-\infty}^{\infty} 2\int_0^{\infty} f(t,r,w,L)\kappa(w,L)\underbrace{\left(\int_{-\sqrt{L}\sin(\theta)}^{\sqrt{L}\sin(\theta)}\frac{1}{\sqrt{L-\frac{1}{\sin^2(\theta)}{p_3}^2}}dp_3\right)}_{=:I} dLdw\,,
\end{aligned} \tag{B.4}$$

where the limits of p_3 comes from when $L - \frac{1}{\sin^2(\theta)}{p_3}^2 > 0$. The extra factor 2 in the integral over L comes from the fact that $(p_1, p_2, p_3) \mapsto (w, L, p_3)$ is a one-to-one map for both $\mathbb{R}\times(-\infty,0)\times\mathbb{R} \to \mathbb{R}\times(0,\infty)\times\mathbb{R}$ and $\mathbb{R}\times(0,\infty)\times\mathbb{R} \to \mathbb{R}\times(0,\infty)\times\mathbb{R}$. Note that (B.4) is true for general kernels, $\kappa(w,L)$, which, in particular, means that it holds for the other elements of T_{ab}.

We thus turn to the integral over p_3, defined as I above. By standard integration,

$$\begin{aligned}
I &= \int_{-\sqrt{L}\sin(\theta)}^{\sqrt{L}\sin(\theta)}\frac{1}{\sqrt{L-\frac{1}{\sin^2(\theta)}{p_3}^2}}dp_3 \\
&= 2\int_0^{\sqrt{L}\sin(\theta)}\frac{1}{\sqrt{L-\frac{1}{\sin^2(\theta)}{p_3}^2}}dp_3 \\
&= \frac{2}{\sqrt{L}}\int_0^{\sqrt{L}\sin(\theta)}\frac{1}{\sqrt{1-\frac{{p_3}^2}{L\sin^2(\theta)}}}dp_3dp_3 \\
&= \frac{2}{\sqrt{L}}\left[\arcsin\left(\frac{p_3}{\sqrt{L}\sin(\theta)}\right)\sqrt{L}\sin(\theta)\right]_0^{\sqrt{L}\sin(\theta)} \\
&= 2\sin(\theta)\arcsin(1) \\
&= \pi\sin(\theta)\,.
\end{aligned} \tag{B.5}$$

With (B.5) in (B.4), we arrive at the final expression in (4.10),

$$T_{\mu\nu} = \frac{\pi}{r^2}\int_{-\infty}^{\infty}\int_0^{\infty} f(t,r,w,L)\kappa(w,L)dLdw\,, \tag{B.6}$$

where $\kappa(w,L)$ is determined for the specific element of T_{ab} considered. For T_{00}, it is as defined in (B.4).

B.2 Conservation of mass

In this appendix, we investigate the conservation of the ADM mass, $\mathcal{M}$, defined in (4.23). The ADM mass should be conserved in time, meaning that $\frac{\partial \mathcal{M}}{\partial t}$ should be 0. To evaluate $\frac{\partial \mathcal{M}}{\partial t}$, we use the Vlasov equation (4.11) and the definitions of ρ, j, p and p_T in (4.8). Remember that $p^0 = \sqrt{1 + w^2 + \frac{L}{r^2}}$. We start by first considering the dust case, before moving on to the full Vlasov case. Note that this is not a rigorous proof, but rather a formal calculation. We assume that all the functions are sufficiently smooth and that f has compact support in phase space.

B.2.1 Dust matter

In the dust case, we have $j = p = p_T = 0$ and $a = 1$. From (4.23), we thus get the ADM mass

$$\mathcal{M} = 4\pi \int_0^\infty \rho(t, r) r^2 dr \,. \tag{B.7}$$

By using the Vlasov equation (4.11) with $a = 1$ we get

$$\begin{aligned}
\frac{\partial \mathcal{M}}{\partial t} &= 4\pi \int_0^\infty \frac{\partial \rho}{\partial t} r^2 dr = 4\pi \int_0^\infty r^2 \frac{\pi}{r^2} \int_{-\infty}^\infty \int_0^\infty p^0 \frac{\partial f}{\partial t} dL dw dr \\
&= 4\pi^2 \int_0^\infty \int_{-\infty}^\infty \int_0^\infty p^0 \left(- \left(\frac{w}{a p^0} - \beta \right) \frac{\partial f}{\partial r} - \left[\left(\frac{\beta}{a} \frac{\partial a}{\partial r} + \frac{\partial \beta}{\partial r} - \frac{1}{a} \frac{\partial a}{\partial t} \right) w + \frac{L}{a p^0 r^3} \right] \frac{\partial f}{\partial w} \right) dL dw dr \\
&= 4\pi^2 \int_0^\infty \int_{-\infty}^\infty \int_0^\infty \left(-w + \beta p^0 \right) \frac{\partial f}{\partial r} - \left(\frac{\partial \beta}{\partial r} p^0 w + \frac{L}{r^3} \right) \frac{\partial f}{\partial w} dL dw dr \,.
\end{aligned}$$

Add and remove $\beta \frac{\partial p^0}{\partial r} f$ in the integrand, and note that $\frac{\partial p^0}{\partial r} = -\frac{L}{p^0 r^3}$

$$= 4\pi^2 \int_0^\infty \int_{-\infty}^\infty \int_0^\infty -w \frac{\partial f}{\partial r} + \beta \Big(\underbrace{p^0 \frac{\partial f}{\partial r} + \frac{\partial p^0}{\partial r} f}_{\frac{\partial}{\partial r}(p^0 f)} \Big) - \beta \underbrace{\frac{\partial p^0}{\partial r}}_{= -\frac{L}{p^0 r^3}} f - \left(\frac{\partial \beta}{\partial r} p^0 w + \frac{L}{r^3} \right) \frac{\partial f}{\partial w} dL dw dr \,.$$

Use the definitions of ρ, j, p and p in (4.8), to simplify as

$$\begin{aligned}
= 4\pi^2 \int_0^\infty \Bigg[&- \frac{\partial}{\partial r} \Bigg(\underbrace{\int_{-\infty}^\infty \int_0^\infty w f dL dw}_{= \frac{r^2}{\pi} j} \Bigg) + \beta \frac{\partial}{\partial r} \Bigg(\underbrace{\int_{-\infty}^\infty \int_0^\infty p^0 f dL dw}_{= \frac{r^2}{\pi} \rho} \Bigg) \\
&+ \frac{\beta}{r^3} \underbrace{\int_{-\infty}^\infty \int_0^\infty \frac{L}{p^0} f dL dw}_{= \frac{2r^4}{\pi} p_T} \Bigg) - \int_{-\infty}^\infty \int_0^\infty \left(\frac{\partial \beta}{\partial r} p^0 w + \frac{L}{r^3} \right) \frac{\partial f}{\partial w} dL dw \Bigg] dr \,.
\end{aligned}$$

Now use partial integration with respect to w on the last term and note that f has compact support in w

$$
\begin{aligned}
&= 4\pi^2 \int_0^\infty \Bigg[- \frac{\partial}{\partial r}\left(\frac{r^2}{\pi} j\right) + \beta \frac{\partial}{\partial r}\left(\frac{r^2}{\pi}\rho\right) + \frac{2\beta r}{\pi} p_T \\
&\quad - \int_0^\infty \underbrace{\left[\left(\frac{\partial\beta}{\partial r} p^0 w + \frac{L}{ar^3}\right) f\right]_{-\infty}^{\infty}}_{\substack{=0 \\ \text{since } w^2 f \to 0 \text{ as } w\to\pm\infty}} dL + \frac{\partial\beta}{\partial r} \underbrace{\int_{-\infty}^\infty \int_0^\infty \left(\frac{w^2}{p^0} + p^0\right) f dL dw}_{=\frac{r^2}{\pi}p + \frac{r^2}{\pi}\rho} \Bigg] dr \\
&= 4\pi \int_0^\infty \Bigg[- \frac{\partial}{\partial r}\Big(\underbrace{r^2 j}_{=0}\Big) + \underbrace{\beta \frac{\partial}{\partial r}\Big(r^2\rho\Big) + \frac{\partial\beta}{\partial r} r^2 \rho}_{=\frac{\partial}{\partial r}(\beta r^2 \rho)} + \frac{\partial\beta}{\partial r} \underbrace{r^2 p}_{=0} + 2\beta \underbrace{r p_T}_{=0} \Bigg] dr \\
&= 4\pi \int_0^\infty \frac{\partial}{\partial r}\Big(\beta r^2 \rho\Big) dr = 4\pi \Big[\beta(t,r) r^2 \rho(t,r)\Big]_0^\infty \\
&= 4\pi^2 \lim_{r\to\infty} \Bigg(\underbrace{\beta(t,r)}_{\substack{\to 0 \\ \text{by (4.2)}}} \int_{-\infty}^\infty \int_0^\infty p^0 \underbrace{f(t,r,w,L)}_{\to 0} dL dw \Bigg) - 4\pi \lim_{r\to 0} \Big(\beta(t,r) r^2 \rho(r,t)\Big) \ .
\end{aligned}
$$

In conclusion, for general dust data

$$
\frac{\partial \mathcal{M}}{\partial t} = -4\pi \lim_{r\to 0} \Big(\beta(t,r) r^2 \rho(r,t)\Big) \ . \tag{B.8}
$$

In the case of Eardly-Smarr data, both β and ρ are known analytically by (4.39) and (4.42). The above limit can thus be evaluated explicitly as

$$
\begin{aligned}
\frac{\partial \mathcal{M}}{\partial t} &= -4\pi \lim_{r\to 0} \left(\sqrt{\frac{2}{r}} \left(-\frac{\mathring{t}-t}{2\zeta} + \sqrt{\frac{(\mathring{t}-t)^2}{4\zeta^2} + \frac{1}{\zeta}\left(\frac{r}{c_0}\right)^{\frac{3}{2}}} \right) r^2 \frac{3\left(-\frac{\mathring{t}-t}{2\zeta} + \sqrt{\frac{(\mathring{t}-t)^2}{4\zeta^2} + \frac{1}{\zeta}\left(\frac{r}{c_0}\right)^{\frac{3}{2}}} \right)}{8\pi c_0^{\frac{3}{2}} \zeta r^{\frac{3}{2}} \sqrt{\frac{(\mathring{t}-t)^2}{4\zeta^2} + \frac{1}{\zeta}\left(\frac{r}{c_0}\right)^{\frac{3}{2}}}} \right) \\
&= \frac{-3\sqrt{2}}{2c_0^{\frac{3}{2}}\zeta} \lim_{r\to 0} \left(\frac{r^2}{r^{\frac{1}{2}} r^{\frac{3}{2}}} \frac{\left(-\frac{\mathring{t}-t}{2\zeta} + \sqrt{\frac{(\mathring{t}-t)^2}{4\zeta^2} + \frac{1}{\zeta}\left(\frac{r}{c_0}\right)^{\frac{3}{2}}} \right)^2}{\sqrt{\frac{(\mathring{t}-t)^2}{4\zeta^2} + \frac{1}{\zeta}\left(\frac{r}{c_0}\right)^{\frac{3}{2}}}} \right) \\
&= \frac{-3}{\sqrt{2}(\frac{9}{2})^{\frac{1}{3}\cdot\frac{3}{2}}\zeta} \lim_{r\to 0} \left(\frac{\left(-\frac{\mathring{t}-t}{2\zeta} + \sqrt{\frac{(\mathring{t}-t)^2}{4\zeta^2} + \frac{1}{\zeta}\left(\frac{r}{c_0}\right)^{\frac{3}{2}}} \right)^2}{\sqrt{\frac{(\mathring{t}-t)^2}{4\zeta^2} + \frac{1}{\zeta}\left(\frac{r}{c_0}\right)^{\frac{3}{2}}}} \right) \\
&= \frac{-3}{\sqrt{2}(\frac{9}{2})^{\frac{1}{2}}\zeta} \frac{\left(-\frac{\mathring{t}-t}{2\zeta} + \sqrt{\frac{(\mathring{t}-t)^2}{4\zeta^2}} \right)^2}{\sqrt{\frac{(\mathring{t}-t)^2}{4\zeta^2}}} \\
&= \frac{-1}{\zeta} \frac{\left(-\frac{\mathring{t}-t}{2\zeta} + \frac{|\mathring{t}-t|}{2\zeta} \right)^2}{\frac{|\mathring{t}-t|}{2\zeta}} = \begin{cases} 0 & , t < \mathring{t} \\ \frac{-2}{\zeta^2}(t-\mathring{t}) & , t > \mathring{t} \end{cases} ,
\end{aligned} \tag{B.9}
$$

which shows that the ADM mass is not preserved. The reason is that for $t > \mathring{t}$, we do not have regularity at the centre, which requires $\lim_{r\to 0} \beta(t,r) = 0$, see (4.2). To verify the above calculation and to illustrate the effect of $\mathcal{M}$ not being conserved, we define a correction term by

$$\tilde{m}(t) = \begin{cases} 0 & , t < \mathring{t} \\ \frac{(t-\mathring{t})^2}{\zeta^2} & , t > \mathring{t} \end{cases}, \tag{B.10}$$

so that

$$\frac{\partial}{\partial t}\Big(\mathcal{M} + \tilde{m}(t)\Big) = \begin{cases} 0 & , t < \mathring{t} \\ \frac{-2}{\zeta^2}(t-\mathring{t}) + \frac{\partial}{\partial t}\left(\frac{(t-\mathring{t})^2}{\zeta^2}\right) = 0 & , t > \mathring{t} \end{cases}. \tag{B.11}$$

In words, by adding $\tilde{m}(t)$ to the mass function, the ADM mass is conserved. In Figure B.1 we plot the mass, $M(t,r)$, calculated either as in (4.22) or as in (4.41) and add or remove $\tilde{m}(t)$. Note that (4.22) and (4.41) should be equivalent.

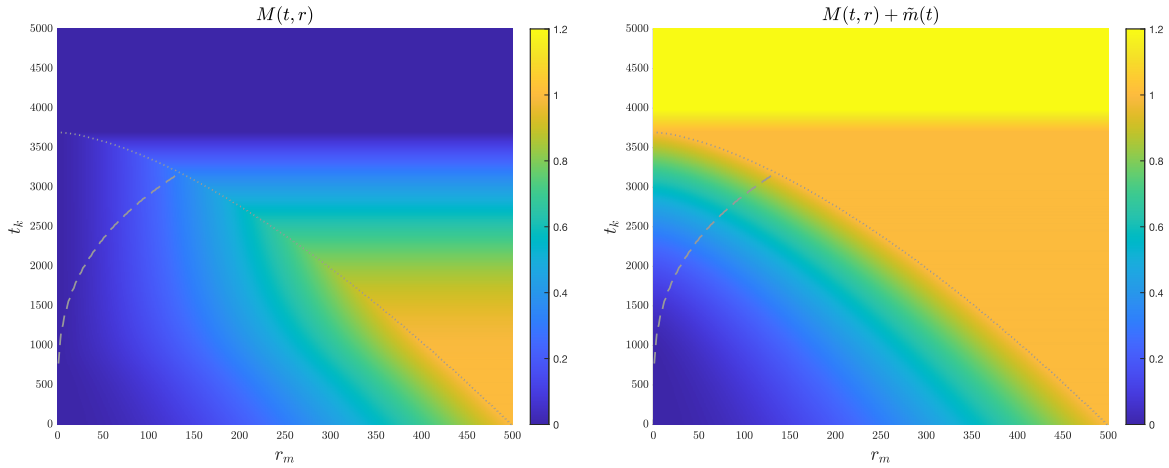

(a) $M(t,r) = (4.22)$ **(b)** $M(t,r) = (4.22) + \tilde{m}(t,r)$

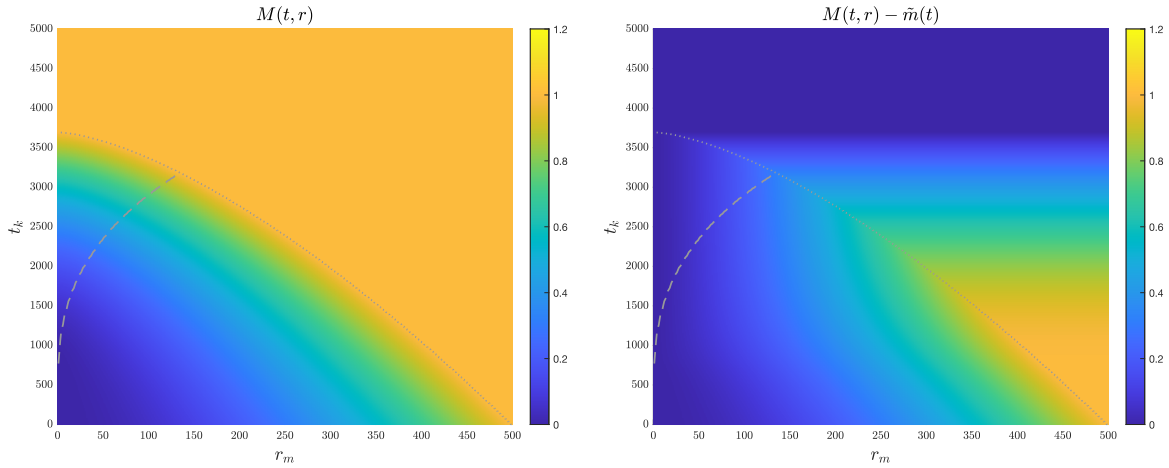

(c) $M(t,r) = (4.41)$ **(d)** $M(t,r) = (4.41)$ - $\tilde{m}(t,r)$

Figure B.1: Dust mass function calculated in different ways with and without the correction term.

We see that without the correction term, the mass calculated from (4.22) vanishes. By adding the correction to M from (4.22), the mass that equals the analytical dust mass in (4.41) (except for the top region, which occurs after all the particles have converged to the centre, i.e. $r_b(t) = 0$), see Figure B.1b and Figure B.1c. Similarly, by assing $-\tilde{m}$ to the mass in (4.41), the result equals that of $M(t, r)$ calculated from (4.22), see Figure B.1d and Figure B.1a.

Finally, in the Oppenheimer-Snyder dust case, $\beta(t, r) = \frac{2\sqrt{2c}}{3} r \left(1 - \sqrt{2c}t\right)^{-1}$ [9]. With $M(t, r) = \beta^2 \frac{r}{2}$ and $\rho(t, r) = \frac{1}{4\pi r^2} \frac{\partial M}{\partial r}$ we by (B.8) get,

$$\begin{aligned}
\frac{\partial \mathcal{M}}{\partial t} &= -4\pi \lim_{r\to 0} \Big(\beta(t, r) r^2 \rho(r, t)\Big) \\
&= -4\pi \lim_{r\to 0} \left(\beta(t, r) r^2 \frac{1}{4\pi r^2} \frac{\partial}{\partial r} \left(\frac{r}{2}\beta^2\right)\right) \\
&= -\frac{1}{2} \lim_{r\to 0} \left(\beta(t, r) \left(\frac{1}{2}\beta^2 + r\beta \frac{\partial \beta}{\partial r}\right)\right) \\
&= \frac{1}{4} \lim_{r\to 0} \left(\beta^3(t, r) + 2\beta^2(t, r) r \frac{2\sqrt{2c}}{3} \left(1 - \sqrt{2c}t\right)^{-1}\right) \\
&= \frac{3}{4} \lim_{r\to 0} \beta^3(t, r) = 0 \,.
\end{aligned} \tag{B.12}$$

The ADM mass is thus conserved with homogeneous data, since regularity at the centre is always fulfilled. This explains why no vanishing mass problems occur in the Oppenheimer-Snyder simulations presented in section 6.1.

B.2.2 Vlasov matter

In the Vlasov case, the derivation becomes more complicated since j, p, p_T and a are non-constant. The time derivative of the ADM mass in (4.23) becomes

$$\begin{aligned}
\frac{\partial \mathcal{M}}{\partial t} &= 4\pi \int_0^\infty \left(\frac{\partial \rho}{\partial t} - \frac{\partial}{\partial t}\big(a\beta j\big)\right) r^2 dr \\
&= 4\pi \int_0^\infty \left[\underbrace{\frac{\partial \rho}{\partial t} r^2}_{=:I_1} - \left(\frac{\partial a}{\partial t}\beta + a\frac{\partial \beta}{\partial t}\right) j r^2 - a\beta \underbrace{\frac{\partial j}{\partial t} r^2}_{=:I_2}\right] dr \,,
\end{aligned} \tag{B.13}$$

where we expand I_1 and I_2 separately with the same techniques as in the dust case. Note that I_1, is the same as in the dust case plus some extra terms arising from a no longer being constant. Specifically,

$$\begin{aligned}
I_1 &= r^2 \frac{\pi}{r^2} \int_{-\infty}^\infty \int_0^\infty p^0 \frac{\partial f}{\partial t} dL dw \\
&= \pi \int_{-\infty}^\infty \int_0^\infty p^0 \left(-\left(\frac{w}{ap^0} - \beta\right) \frac{\partial f}{\partial r} - \left[\left(\frac{\beta}{a}\frac{\partial a}{\partial r} + \frac{\partial \beta}{\partial r} - \frac{1}{a}\frac{\partial a}{\partial t}\right) w + \frac{L}{ap^0 r^3}\right] \frac{\partial f}{\partial w}\right) dL dw \\
&= \pi \int_{-\infty}^\infty \int_0^\infty \left(-\frac{w}{a} + \beta p^0\right) \frac{\partial f}{\partial r} - \left[\left(\frac{\beta}{a}\frac{\partial a}{\partial r} + \frac{\partial \beta}{\partial r} - \frac{1}{a}\frac{\partial a}{\partial t}\right) p^0 w + \frac{L}{ar^3}\right] \frac{\partial f}{\partial w} dL dw \,.
\end{aligned}$$

Add and remove $\beta\frac{\partial p^0}{\partial r}f$ in the integrand, and note that $\frac{\partial p^0}{\partial r} = -\frac{L}{p^0 r^3}$

$$= \pi \int_{-\infty}^{\infty}\int_{0}^{\infty} \Bigg[-\frac{w}{a}\frac{\partial f}{\partial r} + \beta\Big(\underbrace{p^0\frac{\partial f}{\partial r} + \frac{\partial p^0}{\partial r}f}_{\frac{\partial}{\partial r}(p^0 f)}\Big) - \beta \underbrace{\frac{\partial p^0}{\partial r}}_{=-\frac{L}{p^0 r^3}} f \\ - \left[\left(\frac{\beta}{a}\frac{\partial a}{\partial r} + \frac{\partial \beta}{\partial r} - \frac{1}{a}\frac{\partial a}{\partial t}\right)p^0 w + \frac{L}{a r^3}\right]\frac{\partial f}{\partial w}\Bigg] dL dw\,.$$

Simplify with (4.8) as

$$= \pi\Bigg[-\frac{1}{a}\frac{\partial}{\partial r}\Big(\underbrace{\int_{-\infty}^{\infty}\int_{0}^{\infty} w f dL dw}_{=\frac{r^2}{\pi}j}\Big) + \beta\frac{\partial}{\partial r}\Big(\underbrace{\int_{-\infty}^{\infty}\int_{0}^{\infty} p^0 f dL dw}_{=\frac{r^2}{\pi}\rho}\Big) + \frac{\beta}{r^3}\underbrace{\int_{-\infty}^{\infty}\int_{0}^{\infty}\frac{L}{p^0} f dL dw}_{=\frac{2r^4}{\pi}p_T}\Big) \\ - \int_{-\infty}^{\infty}\int_{0}^{\infty}\left[\left(\frac{\beta}{a}\frac{\partial a}{\partial r} + \frac{\partial \beta}{\partial r} - \frac{1}{a}\frac{\partial a}{\partial t}\right)p^0 w + \frac{L}{a r^3}\right]\frac{\partial f}{\partial w} dL dw\Bigg]\,. \tag{B.14}$$

Use partial integration with respect to w on the last term and compact support of f in w

$$\begin{aligned}
&= \pi\Bigg[-\frac{1}{a}\frac{\partial}{\partial r}\left(\frac{r^2}{\pi}j\right) + \beta\frac{\partial}{\partial r}\left(\frac{r^2}{\pi}\rho\right) + \frac{2r}{\pi}\beta p_T \\
&\qquad - \int_0^{\infty}\underbrace{\left[\left(\left(\frac{\beta}{a}\frac{\partial a}{\partial r} + \frac{\partial \beta}{\partial r} - \frac{1}{a}\frac{\partial a}{\partial t}\right)p^0 w + \frac{L}{a r^3}\right) f\right]_{-\infty}^{\infty}}_{\substack{=0 \\ \text{since } w^2 f \to 0 \text{ as } w\to\pm\infty}} dL \\
&\qquad + \left(\frac{\beta}{a}\frac{\partial a}{\partial r} + \frac{\partial \beta}{\partial r} - \frac{1}{a}\frac{\partial a}{\partial t}\right)\underbrace{\int_{-\infty}^{\infty}\int_{0}^{\infty}\left(\frac{w^2}{p^0} + p^0\right) f dL dw}_{\frac{r^2}{\pi}p + \frac{r^2}{\pi}\rho}\Bigg] \\
&= -\frac{1}{a}\frac{\partial}{\partial r}\left(r^2 j\right) + 2r\beta p_T + \beta\frac{\partial}{\partial r}\left(r^2\rho\right) + r^2\left(\frac{\beta}{a}\frac{\partial a}{\partial r} + \frac{\partial \beta}{\partial r} - \frac{1}{a}\frac{\partial a}{\partial t}\right)(p+\rho) \\
&= -\frac{1}{a}\frac{\partial}{\partial r}\left(r^2 j\right) + \underbrace{\beta\frac{\partial}{\partial r}\left(r^2\rho\right) + \frac{\partial \beta}{\partial r}r^2\rho}_{\frac{\partial}{\partial r}(\beta r^2\rho)} + \frac{\partial \beta}{\partial r}r^2 p + r^2\left(\frac{\beta}{a}\frac{\partial a}{\partial r} - \frac{1}{a}\frac{\partial a}{\partial t}\right)(p+\rho) + 2r\beta p_T \\
&= -\frac{1}{a}\frac{\partial}{\partial r}\left(r^2 j\right) + \frac{\partial}{\partial r}\big(\beta r^2\rho\big) + \frac{\partial \beta}{\partial r}r^2 p + r^2\left(\frac{\beta}{a}\frac{\partial a}{\partial r} - \frac{1}{a}\frac{\partial a}{\partial t}\right)(p+\rho) + 2r\beta p_T\,.
\end{aligned} \tag{B.15}$$

Note that the dust case is recovered when $j = p = p_T = 0$ and $a = 1$.

Now the same thing can be done for I_2 as,

$$
\begin{aligned}
I_2 &= r^2 \frac{\pi}{r^2} \int_{-\infty}^{\infty} \int_0^{\infty} w \frac{\partial f}{\partial t} dL dw \\
&= \pi \int_{-\infty}^{\infty} \int_0^{\infty} w \left(- \left(\frac{w}{a p^0} - \beta \right) \frac{\partial f}{\partial r} - \left[\left(\frac{\beta}{a} \frac{\partial a}{\partial r} + \frac{\partial \beta}{\partial r} - \frac{1}{a} \frac{\partial a}{\partial t} \right) w + \frac{L}{a p^0 r^3} \right] \frac{\partial f}{\partial w} \right) dL dw \\
&= \pi \int_{-\infty}^{\infty} \int_0^{\infty} \left(- \frac{w^2}{a p^0} + \beta w \right) \frac{\partial f}{\partial r} - \left[\left(\frac{\beta}{a} \frac{\partial a}{\partial r} + \frac{\partial \beta}{\partial r} - \frac{1}{a} \frac{\partial a}{\partial t} \right) w^2 + \frac{wL}{a p^0 r^3} \right] \frac{\partial f}{\partial w} dL dw \,.
\end{aligned}
$$

Add and remove $-\frac{w^2}{a} \frac{\partial}{\partial r} \left(\frac{1}{p^0} \right) f$ in the integrand, and note that $\frac{\partial}{\partial r} \left(\frac{1}{p^0} \right) = \frac{L}{(p^0)^3 r^3}$

$$
\begin{aligned}
&= \pi \int_{-\infty}^{\infty} \int_0^{\infty} \Bigg[- \frac{w^2}{a} \Big(\underbrace{\frac{1}{p^0} \frac{\partial f}{\partial r} + \frac{\partial}{\partial r} \left(\frac{1}{p^0} \right) f}_{\frac{\partial}{\partial r} \left(\frac{1}{p^0} f \right)} \Big) + \frac{w^2}{a} \underbrace{\frac{\partial}{\partial r} \left(\frac{1}{p^0} \right)}_{= \frac{L}{(p^0)^3 r^3}} f + \beta w \frac{\partial f}{\partial r} \\
&\qquad\qquad - \left[\left(\frac{\beta}{a} \frac{\partial a}{\partial r} + \frac{\partial \beta}{\partial r} - \frac{1}{a} \frac{\partial a}{\partial t} \right) w^2 + \frac{wL}{a p^0 r^3} \right] \frac{\partial f}{\partial w} \Bigg] dL dw \\
&= \pi \Bigg[- \frac{1}{a} \frac{\partial}{\partial r} \Bigg(\underbrace{\int_{-\infty}^{\infty} \int_0^{\infty} \frac{w^2}{p^0} f dL dw}_{= \frac{r^2}{\pi} p} \Bigg) + \frac{1}{a r^3} \underbrace{\int_{-\infty}^{\infty} \int_0^{\infty} \frac{w^2 L}{(p^0)^3} f dL dw}_{=: I_3} \\
&+ \beta \frac{\partial}{\partial r} \Bigg(\underbrace{\int_{-\infty}^{\infty} \int_0^{\infty} w f dL dw}_{= \frac{r^2}{\pi} j} \Bigg) - \int_{-\infty}^{\infty} \int_0^{\infty} \left[\left(\frac{\beta}{a} \frac{\partial a}{\partial r} + \frac{\partial \beta}{\partial r} - \frac{1}{a} \frac{\partial a}{\partial t} \right) w^2 + \frac{wL}{a p^0 r^3} \right] \frac{\partial f}{\partial w} dL dw \Bigg] ,
\end{aligned}
$$

where we define the integral I_3 for notational convenience. Using partial integration with respect to w on the last term, together with compact support of f in w,

$$
\begin{aligned}
&= \pi \Bigg[- \frac{1}{a} \frac{\partial}{\partial r} \left(\frac{r^2}{\pi} p \right) + \frac{1}{a r^3} I_3 + \beta \frac{\partial}{\partial r} \left(\frac{r^2}{\pi} j \right) \\
&\qquad - \int_0^{\infty} \underbrace{\left[\left(\left(\frac{\beta}{a} \frac{\partial a}{\partial r} + \frac{\partial \beta}{\partial r} - \frac{1}{a} \frac{\partial a}{\partial t} \right) w^2 + \frac{wL}{a p^0 r^3} \right) f \right]_{-\infty}^{\infty}}_{\substack{=0 \\ \text{since } w^2 f \to 0 \text{ as } w \to \pm\infty}} dL \\
&\qquad + \int_{-\infty}^{\infty} \int_0^{\infty} \left[\left(\frac{\beta}{a} \frac{\partial a}{\partial r} + \frac{\partial \beta}{\partial r} - \frac{1}{a} \frac{\partial a}{\partial t} \right) 2w + \frac{L}{a r^3} \left(\frac{1}{p^0} - \frac{w^2}{(p^0)^3} \right) \right] f dL dw \Bigg]
\end{aligned}
$$

$$= \pi \Bigg[-\frac{1}{a}\frac{\partial}{\partial r}\left(\frac{r^2}{\pi}p\right) + \beta\frac{\partial}{\partial r}\left(\frac{r^2}{\pi}j\right) + \frac{1}{ar^3}I_3 + 2\left(\frac{\beta}{a}\frac{\partial a}{\partial r} + \frac{\partial\beta}{\partial r} - \frac{1}{a}\frac{\partial a}{\partial t}\right)\underbrace{\int_{-\infty}^{\infty}\int_0^{\infty} w f dL dw}_{=\frac{r^2}{\pi}j}$$
$$+ \frac{1}{ar^3}\underbrace{\int_{-\infty}^{\infty}\int_0^{\infty}\frac{L}{p^0}f dL dw}_{=\frac{2r^4}{\pi}p_T} - \frac{1}{ar^3}\underbrace{\int_{-\infty}^{\infty}\int_0^{\infty}\frac{w^2 L}{(p^0)^3}f dL dw}_{=I_3}\Bigg]$$
$$= -\frac{1}{a}\frac{\partial}{\partial r}\left(r^2 p\right) + \beta\frac{\partial}{\partial r}\left(r^2 j\right) + 2r^2 j\left(\frac{\beta}{a}\frac{\partial a}{\partial r} + \frac{\partial\beta}{\partial r} - \frac{1}{a}\frac{\partial a}{\partial t}\right) + \frac{2r}{a}p_T\,. \tag{B.16}$$

Thus, the sought after $-a\beta I_2$ in (B.13) is

$$-a\beta I_2 = -a\beta\left[-\frac{1}{a}\frac{\partial}{\partial r}\left(r^2 p\right) + \beta\frac{\partial}{\partial r}\left(r^2 j\right) + 2r^2 j\left(\frac{\beta}{a}\frac{\partial a}{\partial r} + \frac{\partial\beta}{\partial r} - \frac{1}{a}\frac{\partial a}{\partial t}\right) + \frac{2r}{a}p_T\right]$$
$$= \beta\frac{\partial}{\partial r}\left(r^2 p\right) - a\beta^2\frac{\partial}{\partial r}\left(r^2 j\right) - 2r^2 j\left(\beta^2\frac{\partial a}{\partial r} + a\beta\frac{\partial\beta}{\partial r} - \beta\frac{\partial a}{\partial t}\right) - 2r\beta p_T\,. \tag{B.17}$$

We now gather the terms in the integrand of (B.13). To keep track, we use violet colour for terms from (B.15) and blue colour for terms from (B.17). Then,

$$I_1 - \left(\frac{\partial a}{\partial t}\beta + a\frac{\partial\beta}{\partial t}\right)jr^2 - a\beta I_2$$
$$= \frac{\partial}{\partial r}\left(\beta r^2\rho\right) + \underbrace{\beta\frac{\partial}{\partial r}\left(r^2 p\right) + \frac{\partial\beta}{\partial r}r^2 p}_{\frac{\partial}{\partial r}(\beta r^2 p)} - \left(a\beta^2 + \frac{1}{a}\right)\frac{\partial}{\partial r}\left(r^2 j\right) - \left(\beta^2\frac{\partial a}{\partial r} + 2a\beta\frac{\partial\beta}{\partial r}\right)r^2 j$$
$$+ r^2 j\left(-\beta^2\frac{\partial a}{\partial r} + 2\beta\frac{\partial a}{\partial t} - \frac{\partial a}{\partial t}\beta - a\frac{\partial\beta}{\partial t}\right) + r^2\left(\frac{\beta}{a}\frac{\partial a}{\partial r} - \frac{1}{a}\frac{\partial a}{\partial t}\right)(p+\rho) + (2r\beta - 2r\beta)\,p_T\,.$$

Add and remove $\frac{\partial}{\partial r}\left(\frac{1}{a}\right)r^2 j = \frac{-1}{a^2}\frac{\partial a}{\partial r}r^2 j$

$$= \frac{\partial}{\partial r}\left(\beta r^2\rho\right) + \frac{\partial}{\partial r}\left(\beta r^2 p\right)\underbrace{- \left(a\beta^2 + \frac{1}{a}\right)\frac{\partial}{\partial r}\left(r^2 j\right) - \left(\beta^2\frac{\partial a}{\partial r} + 2a\beta\frac{\partial\beta}{\partial r} - \frac{1}{a^2}\frac{\partial a}{\partial r}\right)r^2 j}_{-\frac{\partial}{\partial r}\left[\left(a\beta^2+\frac{1}{a}\right)r^2 j\right]}$$
$$+ r^2 j\left(\left(-\frac{1}{a^2} - \beta^2\right)\frac{\partial a}{\partial r} + \beta\frac{\partial a}{\partial t} - a\frac{\partial\beta}{\partial t}\right) + r^2\left(\frac{\beta}{a}\frac{\partial a}{\partial r} - \frac{1}{a}\frac{\partial a}{\partial t}\right)(p+\rho)\,,$$

and by linearity gather all the $\frac{\partial}{\partial r}$ terms

$$= \frac{\partial}{\partial r}\left[r^2\left(\beta(\rho+p) - \left(a\beta^2 + \frac{1}{a}\right)j\right)\right]$$
$$\underbrace{+ r^2 j\left(-\left(\frac{1}{a^2} + \beta^2\right)\frac{\partial a}{\partial r} + \beta\frac{\partial a}{\partial t} - a\frac{\partial\beta}{\partial t}\right) + r^2\left(\frac{\beta}{a}\frac{\partial a}{\partial r} - \frac{1}{a}\frac{\partial a}{\partial t}\right)(p+\rho)}_{=:I_4}$$
$$= \frac{\partial}{\partial r}\left[r^2\left(\beta(\rho+p) - \left(a\beta^2 + \frac{1}{a}\right)j\right)\right] + I_4\,, \tag{B.18}$$

where we gather all the extra terms in I_4 for convenience. We proceed to show that $I_4 = 0$ by combining the Einstein equations (4.15-4.18) as follows

$$
\begin{aligned}
I_4 &= r^2 j \left(-\left(\frac{1}{a^2} + \beta^2\right) \frac{\partial a}{\partial r} + \beta \frac{\partial a}{\partial t} - a \frac{\partial \beta}{\partial t} \right) + r^2 \underbrace{\left(\frac{\beta}{a} \frac{\partial a}{\partial r} - \frac{1}{a} \frac{\partial a}{\partial t} \right)}_{\substack{=4\pi r a j \\ \text{by (4.18)}}} (p + \rho) \\
&= r^2 j \left(-\left(\frac{1}{a^2} + \beta^2\right) \frac{\partial a}{\partial r} + \beta \frac{\partial a}{\partial t} - a \frac{\partial \beta}{\partial t} \right) + 4\pi r^3 a j (p + \rho) \\
&= r^2 j \left(-\left(\frac{1}{a^2} + \beta^2\right) \frac{\partial a}{\partial r} + \beta \frac{\partial a}{\partial t} - a \frac{\partial \beta}{\partial t} + 4\pi r a (p + \rho) \right) .
\end{aligned}
$$

By (4.17), $\frac{\partial \beta}{\partial t} = \beta \frac{\partial \beta}{\partial r} + \frac{1}{2r}(1 - A) + 4\pi r p$, so

$$
\begin{aligned}
&= r^2 j \left(-\left(\frac{1}{a^2} + \beta^2\right) \frac{\partial a}{\partial r} + \beta \frac{\partial a}{\partial t} - a \left(\beta \frac{\partial \beta}{\partial r} + \frac{1}{2r}(1 - A) + 4\pi r p \right) + 4\pi r a (p + \rho) \right) \\
&= r^2 j \left(-\left(\frac{1}{a^2} + \beta^2\right) \frac{\partial a}{\partial r} + \beta \frac{\partial a}{\partial t} - a\beta \frac{\partial \beta}{\partial r} - \frac{a}{2r}(1 - A) + 4\pi r a \rho \right) .
\end{aligned}
$$

By (4.18), $\frac{\partial a}{\partial t} = \beta \frac{\partial a}{\partial r} - 4\pi r a^2 j$, so

$$
\begin{aligned}
&= r^2 j \left(-\left(\frac{1}{a^2} + \beta^2\right) \frac{\partial a}{\partial r} + \beta \left(\beta \frac{\partial a}{\partial r} - 4\pi r a^2 j \right) - a\beta \frac{\partial \beta}{\partial r} - \frac{a}{2r}(1 - A) + 4\pi r a \rho \right) \\
&= r^2 j \left(-\frac{1}{a^2} \frac{\partial a}{\partial r} - a\beta \frac{\partial \beta}{\partial r} - \frac{a}{2r}(1 - A) + 4\pi r a (\rho - a\beta j) \right) .
\end{aligned}
$$

Remember that $A = \frac{1}{a^2} - \beta^2$, so $(1 - A) = 1 - \frac{1}{a^2} + \beta^2$

$$
\begin{aligned}
&= \frac{1}{2} a r j \left(-r \underbrace{\left(\frac{2}{a^3} \frac{\partial a}{\partial r} + 2\beta \frac{\partial \beta}{\partial r} \right)}_{= \frac{\partial}{\partial r}\left(1 - A\right)} - (1 - A) + 8\pi r^2 (\rho - a\beta j) \right) \\
&= \frac{1}{2} a r j \left(-\underbrace{\left[r \frac{\partial}{\partial r}\left(1 - A\right) + (1 - A) \right]}_{= \frac{\partial}{\partial r}\left(r(1 - A)\right)} + 8\pi r^2 (\rho - a\beta j) \right) \\
&= \frac{1}{2} a r j \left(\underbrace{-\frac{\partial}{\partial r}\big(r(1 - A)\big) + 8\pi r^2 (\rho - a\beta j)}_{\substack{=0 \\ \text{by (4.16)}}} \right) = 0
\end{aligned}
\tag{B.19}
$$

With $I_4 = 0$ in (B.18), we can finally write (B.13) as

$$\begin{aligned}
\frac{\partial \mathcal{M}}{\partial t} &= 4\pi \int_0^\infty \frac{\partial}{\partial r}\left[r^2\left(\beta(\rho+p) - \left(a\beta^2 + \frac{1}{a}\right) j\right)\right] \\
&= 4\pi \left[r^2\left(\beta(\rho+p) - \left(a\beta^2 + \frac{1}{a}\right) j\right)\right]_0^\infty \\
&= 4\pi \lim_{r\to\infty}\left[r^2\left(\beta(\rho+p) - \left(a\beta^2 + \frac{1}{a}\right) j\right)\right] - 4\pi \lim_{r\to 0}\left[r^2\left(\beta(\rho+p) - \left(a\beta^2 + \frac{1}{a}\right) j\right)\right] \\
&= 4\pi^2 \lim_{r\to\infty}\Bigg[\underbrace{\beta(t,r)}_{\substack{\to 0 \\ \text{by (4.2)}}} \int_{-\infty}^\infty \int_0^\infty (p^0 + \frac{w^2}{p^0})\, \underbrace{f(t,r,w,L)}_{\to 0}\, dw dL \\
&\qquad\qquad - \underbrace{\left(a\beta^2 + \frac{1}{a}\right)}_{\substack{\to 1 \\ \text{by (4.2)}}} \int_{-\infty}^\infty \int_0^\infty w\, \underbrace{f(t,r,w,L)}_{\to 0}\, dw dL\Bigg] \\
&\qquad\qquad - 4\pi \lim_{r\to 0}\left[r^2\left(\beta(\rho+p) - \left(a\beta^2 + \frac{1}{a}\right) \underbrace{j}_{\to 0}\right)\right] \\
&= -4\pi \lim_{r\to 0}\left[r^2 \beta(t,r)(\rho+p)_{(t,r)}\right], \qquad \text{(B.20)}
\end{aligned}$$

which, as in the dust case, would give a conserved ADM mass if $\lim_{r\to 0} \beta(t,r) = 0$ in accordance with (4.2). As seen in the dust case, this is however not true for $t > \mathring{t}$ in the Eardly-Smarr case. Note that the dust case (B.8) is recovered from (B.20) with $p = 0$.

B.3 Derivation of the Kretschmann scalar

In this appendix, some details of the calculation of the Kretschmann scalar is provided. The main calculation and initial simplification should be credited to T. Bäckdahl, who performed them with Mathematica. For the metric in (4.1), the Kretschmann scalar is calculated from (2.33) as

$$\begin{aligned}K = 4\Bigg(&\frac{(1-a^{-2}+\beta^2)^2}{r^4} - \frac{4}{a^4 r^2}\left(\frac{\partial a}{\partial t} + a^3\beta\frac{\partial \beta}{\partial t}\right)\left(\frac{\partial a}{\partial t} - \beta\frac{\partial a}{\partial r}\right)\\ &+ \frac{2}{r^2}\left(\frac{1}{a^3}\frac{\partial a}{\partial r} + \beta\frac{\partial \beta}{\partial r}\right)^2 + \frac{2}{a^2 r^2}\left(-a\frac{\partial \beta}{\partial t} + \beta^2\frac{\partial a}{\partial r} + \beta\left(-\frac{\partial a}{\partial t} + a\frac{\partial \beta}{\partial r}\right)\right)^2\\ &+ \frac{1}{a^2}\Bigg(\frac{\partial^2 a}{\partial t^2} - \frac{\partial a}{\partial r}\frac{\partial \beta}{\partial t} - 2\frac{\partial a}{\partial t}\frac{\partial \beta}{\partial r} + 3\beta\frac{\partial a}{\partial r}\frac{\partial \beta}{\partial r} + a\left(\frac{\partial \beta}{\partial r}\right)^2 - 2\beta\frac{\partial^2 a}{\partial t \partial r}\\ &\qquad - a\frac{\partial^2 \beta}{\partial t \partial r} + \beta^2\frac{\partial^2 a}{\partial r^2} + a\beta\frac{\partial^2 \beta}{\partial r^2}\Bigg)^2\Bigg). \end{aligned} \tag{B.21}$$

To simplifiy the expression, we complement the subsystem of the Einstein field equations presented in (4.15-4.18), with a field equation involving the tangential pressure, p_T. It reads,

$$\begin{aligned}\frac{r}{a^3}\Bigg(&a^2\beta\frac{\partial a}{\partial t} + a^3\frac{\partial \beta}{\partial t} - a^2 r\frac{\partial^2 a}{\partial t^2} - (1+a^2\beta^2)\frac{\partial a}{\partial r} + a^2 r\frac{\partial a}{\partial r}\frac{\partial \beta}{\partial t}\\ &-2a^3\beta\frac{\partial \beta}{\partial r} + 2a^2\frac{\partial a}{\partial t}\frac{\partial \beta}{\partial r} - 3a^2\beta r\frac{\partial a}{\partial r}\frac{\partial \beta}{\partial r} - a^3 r\left(\frac{\partial \beta}{\partial r}\right)^2\\ &+2a^2\beta r\frac{\partial^2 a}{\partial t \partial r} + a^3 r\frac{\partial^2 \beta}{\partial t \partial r} - a^2\beta^2 r\frac{\partial^2 a}{\partial r^2} - a^3\beta r\frac{\partial^2 \beta}{\partial r^2}\Bigg) = 8\pi r^2 p_T\,. \end{aligned} \tag{B.22}$$

With (4.15-4.18) and (B.22), the expression in (B.21) can be simplified to

$$\begin{aligned}K = \frac{4}{r^4}\Bigg[&3(1-A)^2 + 16\pi r^2\Big((p - p_T - \rho)(1-A)\\ &- r^2(4j^2 - 2(p^2+\rho^2) - (2p_T - p - \rho)^2)\Big)\Bigg], \end{aligned} \tag{B.23}$$

where we note that $A = \frac{1}{a^2} - \beta^2$ as defined in section 4.1.1. By (4.22), it is, however, also true that $A = 1 - \frac{2M}{r}$. With this in (B.23), we finally get

$$K = \frac{48M^2}{r^6} + 128\pi(p - p_T - \rho)\frac{M}{r^3} - 64\pi(4j^2 - 2(p^2+\rho^2) - (2p_T - p - \rho)^2)\,, \tag{B.24}$$

which is the expression used in this thesis. Note that the first term is the same as in the Schwarzschild solution.

C

Eardly-Smarr solution

In this appendix, the main equations from the paper by Eardly and Smarr are presented as in [4]. This is a complement to the main analysis, presented in section 4.2.2, where this is translated to the framework used in this thesis. Eardly and Smarr use spherically symmetric comoving coordinates to describe a collapsing dust system. Only the main equations of interest are presented here and readers are referred to [4] for details. Note that we here use the same notation as in [4], meaning that the r here is what is denoted $\check{r}$ elsewhere in this thesis.

Consider a metric on the form

$$ds^2 = -dt^2 + X^2(r,t)dr^2 + Y^2(r,t)(d\theta^2 + \sin^2(\theta)d\phi^2). \tag{C.1}$$

The Einstein field equations can then be written as

$$\begin{aligned} X(r,t) &= \frac{\partial Y}{\partial r}\frac{1}{W(r)}\,, \\ \frac{\partial Y^2(r,t)}{\partial t} &= W^2(r) - 1 + \frac{2}{Y(r,t)}\int_0^r W(\tilde{r})\frac{dM(\tilde{r})}{dr}d\tilde{r}\,, \\ \frac{dM(r)}{dr} &= 4\pi\rho(r,t)X(r,t)Y^2(r,t)\,, \end{aligned} \tag{C.2}$$

where M is the proper mass within r, W is the relative binding energy and Y is the area radius. Assume the marginally bound case ($W(r) = 1$), then (C.2) can be written as

$$\begin{aligned} Y(r,t) &= \left(\frac{9M(r)}{2}(t_0(r) - t)^2\right)^{\frac{1}{3}}\,, \\ X(r,t) &= \left(\frac{dM(r)}{dt}(t_0(r) - t) + 2M(r)\frac{dt_0(r)}{dt}\right)\left(6M^2(r)(t_0(r) - t)\right)^{-\frac{1}{3}}\,, \end{aligned} \tag{C.3}$$

where $t_0(r)$ is an integration function which will determine the proper time at which the singularity is hit. Note that for any $r \geq 0$, the area radius $Y(r,t) = 0$ as $t = t_0(r)$.

The trapped surface condition is the same as in (4.24), which in the notation used by Eardly-Smarr is written as $Y(r,t) \leq 2M(r)$. The apparent horizon can be derived from $Y(r,t) = 2M(r)$ in (C.3) as

$$t_H(r) = t_0(r) - \frac{4}{3}M(r)\,. \tag{C.4}$$

For the numerical results, Eardly and Smarr propose using data of the form

$$M(r) = \begin{cases} r^3 & , 0 \leq r \leq 1 \\ 1 & , r > 1 \end{cases}, \quad t_0(r) = \begin{cases} \zeta r^p & , 0 \leq r \leq 1 \\ r^2 - 1 + \zeta & , r > 1 \end{cases}, \tag{C.5}$$

where $\zeta \geq 0$ and $p \in \mathbb{N}_+$ are parameters. Unless $\zeta = 0$ (for which case the data is homogeneous as in the Oppenheimer-Snyder solution) this prescribes inhomogeneous data in the collapsing dust core $0 \leq r \leq 1$. In [4, Table 1], they show that if $p \in \{1, 2, 3\}$ there are threshold values, ζ_{crit}, such that if $\zeta > \zeta_{\text{crit}}$, globally naked singularities are formed. In principle, this means that the trapped surface expands too slowly compared to a radial null geodesic that originates from the origin of the singularity $(r, t) = (0, 0)$.

A radial future-pointing null geodesic of (C.1) satisfies

$$\frac{dt}{dr} = X(r, t)\,. \tag{C.6}$$

By inserting (C.5) in (C.3), we have an expression for $X(t, r)$ and can solve (C.6) with `ode45` in MATLAB to get the null geodesics. We test one of the threshold values given in [4, Table 1]. Namely, for $p = 1$, the threshold value is $\zeta_{\text{crit}} \approx 6.3$. In Figure C.1, null geodesics are plotted for $p = 1$ with $\zeta = 6.1 < \zeta_{\text{crit}}$ and $\zeta = 6.6 > \zeta_{\text{crit}}$ respectively. In both cases, a radial null geodesic is released from the centre at the time of the singularity, i.e. at $(0, 0)$. Note that for the numerics, we start at $(\mathring{r}, 0)$ where $\mathring{r} = 0.0001$. If $\zeta < \zeta_{\text{crit}}$, this light ray is caught by the apparent horizon and will eventually converge into the singularity. However, for $\zeta > \zeta_{\text{crit}}$, the apparent horizon does not expand quickly enough and the light ray can escape to null infinity. For $\zeta > \zeta_{\text{crit}}$, the dust system thus gives naked singularies.

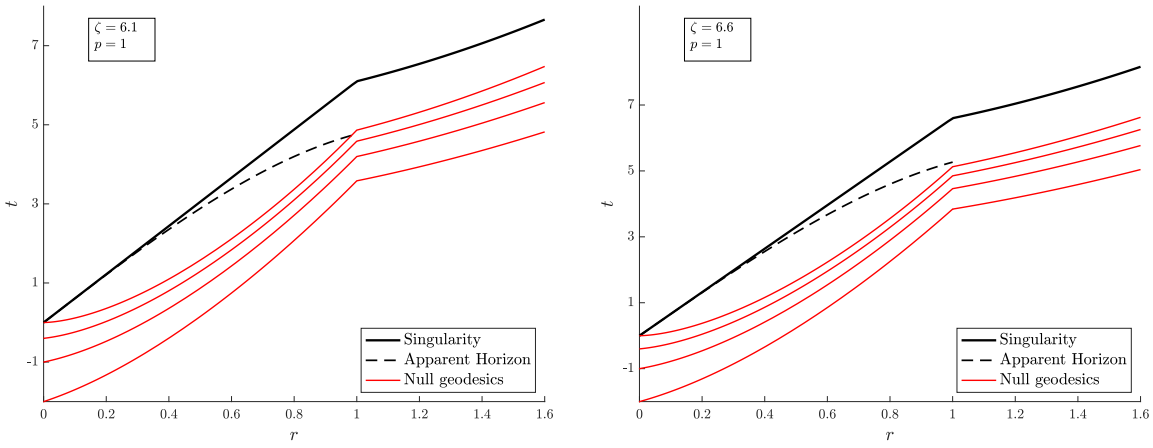

(a) $\zeta < \zeta_{\text{crit}}$ **(b)** $\zeta > \zeta_{\text{crit}}$

Figure C.1: Radial future pointing null geodesics for $p = 1$ and $\zeta \gtrless \zeta_{\text{crit}}$.